

Copyright
by
He-Chun Chou
2012

**The Dissertation Committee for He-Chun Chou Certifies that this is the approved
version of the following dissertation:**

**Enhancement of Raman Signals: Coherent Raman Scattering and
Surface Enhanced Raman Spectroscopy**

Committee:

David A. Vanden Bout, Supervisor

Sang-Hyun Lim, Co-Supervisor

Katherine A. Willets

Peter J. Rossky

Xiaoqin E. Li

**Enhancement of Raman Signals: Coherent Raman Scattering and
Surface Enhanced Raman Spectroscopy**

by

He-Chun Chou, B.S.; M.S.

Dissertation

Presented to the Faculty of the Graduate School of
The University of Texas at Austin
in Partial Fulfillment
of the Requirements
for the Degree of

Doctor of Philosophy

The University of Texas at Austin

May 2012

Dedication

將這本論文獻給我的媽媽，妹妹，還有在另一個世界的爸爸以及阿嬤們

Acknowledgements

I guess this is my first time to write so many words in my own book, and it also may be the last time for me to write my own book. To finish this dissertation, I owe many people's help. Of course, the first one I have to thank is my advisor, Dr. Lim. I have to thank him to give me the chance to enter UT Austin, so I can see the different world. Also, his working attitude and the enthusiasm for science also affect me a lot. Although we didn't have satisfied results in the end, I still learn a lot of science and life from him. Thank for all my committee members for their suggestions of this dissertation. Thank Prof. Vanden Bout for your generous help to take me in my final semester. Thank Prof Rosky, I will never forget your encouragement after my qualify exam. Thank Prof Li, I learned a lot of ultrafast laser from your class. Thank Prof Willets, you really pointed out what lacks in this dissertation. Because of your comments, we found another possible reason to explain our results. Thank all members in Lim group, two Davids, Yoon, Jiha, and Xiaoxi. Also thank all Vanden Bout group people for your help. Thank department staffs, Penny, Sylvia, and Mr. Hooper, especially Penny's help for my final semester. Thank CNM staffs for their technical supports. Thank Dwight to bring me into world of electron microscope. Thank Albert to be my good neighborhood. Thank Bob Fu's help, and we get our PhD in the same semester. Thank Leen, you are really my good friend here. Thank my writing teacher, Judy. Without your writing class, I never finish this dissertation. Finally, if I miss anyone who help me for my PhD life, that's all because of my bad memory. Thank you all.

更重要的是我所有台灣的朋友們，不管你們是在台灣還是米國或是日本，我都一樣的感謝，感謝我的好朋友許哲奇，我們倒楣的命運實在很相似阿，難怪我們的友誼可以維持如此之久。感謝嘴砲大師歷史系王一平，總是鼎力相助小弟，從高中結成

的孽緣果然不是假的。感謝大學好朋友劉俊鴻以及學弟莊啟宏一直的關心。感謝郭俊宏同學跟小弟討論光譜知識以及教會小弟范特西的樂趣。感謝祺姐的建議與關心，你對研究的熱情是我們無法企及的。謝謝余大胖陳小翼夫妻檔在小弟博士班初期以及尾聲所給的幫助及關心。謝謝張哲維同學總是打電話還有寫信要來跟小弟分享看正妹的樂趣。謝謝我的乾媽朱玉玲小姐總是把我當兒子關心。最後謝謝曼倩，我的好朋友。謝謝一路上幫助過我的人，如果我沒寫到你的話只是因為我糟糕的記憶力，而並不是表示你不重要。謝謝大家。

Enhancement of Raman Signals: Coherent Raman Scattering and Surface Enhanced Raman Spectroscopy

He-Chun Chou, Ph.D

The University of Texas at Austin, 2012

Supervisor: David A. Vanden Bout

Co-Supervisor: Sang-Hyun Lim

Raman spectroscopy is a promising technique because it contains abundant vibrational chemical information. However, Raman spectroscopy is restricted by its small scattering cross section, and many techniques have been developed to amplify Raman scattering intensity. In this dissertation, I study two of these techniques, coherent Raman scattering and surface enhanced Raman scattering and discuss their properties.

In the first part of my dissertation, I investigate two coherent Raman processes, coherent anti-Stokes Raman scattering (CARS) and stimulated Raman scattering (SRS). In CARS project, I mainly focus on the molecular resonance effect on detection sensitivity, and I find the detection sensitivity can be pushed into 10 μM with the assistance of molecular resonance. Also, I am able to retrieve background-free Raman spectra from nonresonant signals. For SRS, we develop a new SRS system by applying spectral focusing mechanism technique. We examine the feasibility and sensitivity of our SRS system. The SRS spectra of standards obtained from our system is consistent with literature, and the sensitivity of our system can achieve 10 times above shot-noise limit.

In second part of this dissertation, I study surface enhanced Raman scattering (SERS) and related plasmonic effects. I synthesize different shapes of nanoparticles,

including nanorod, nanodimer structure with gap and pyramids by template method, and study how electric field enhancement effects correlate to SERS by two photon luminescence (TPL). Also, I build an optical system to study optical image, spectra and particle morphology together. I find that SERS intensity distribution is inhomogeneous and closely related to nanoparticle shape and polarization direction. However, TPL and SERS are not completely correlated, and I believe different relaxation pathways of TPL and SERS and coupling of LSPR and local fields at different frequencies cause unclear correlation between them.

Table of Contents

List of Tables	xi
List of Figures	xii
Chapter 1: Introduction	1
Chapter 2: Coherent Raman Scattering.....	6
2.1 Introduction.....	6
2.1.1 Spontaneous Raman versus Coherent Raman process.....	6
2.1.2 Introduction to CARS	8
2.1.3 Introduction to SRS	14
2.1.4 Phase control in Coherent Raman process.....	20
2.1.4.1 Silberberg's work of phase modulation	20
2.1.4.2 Fourier transform spectral interferometry CARS (FTSI-CARS).....	22
2.1.4.3 Spectral Focusing mechanism.....	24
2.2 Experimental Section.....	28
2.2.1 Resonant CARS	28
2.2.2 SRS	29
2.2.2.1 Principles of high frequency modulation, lock-in amplifier and divider circuit	32
2.3 Results and Discussion	35
2.3.1 Resonance CARS.....	35
2.3.2 SRS	39
2.4 Conclusion	45
Chapter 3 Surface Enhanced Raman Scattering	47
3.1 Introduction.....	47
3.1.1 Introduction to localized surface plasmon resonance (LSPR)....	47
3.1.2 Introduction to surface enhanced Raman scattering (SERS).....	54
3.1.3 Nonlinear optics and SERS.....	60
3.1.4 Our work of gold nanorods and pyramids	62

3.2 Experimental Section	64
3.2.1 Synthesize Metal Nanorod by Template Method	64
3.2.2 Coating Silica on Nanorod	66
3.2.3 Simulation of nanorods by discrete dipole approximation	67
3.2.4 Pyramid synthesis procedures	67
3.2.4.1 Fabrication of regular and shaped pyramids	71
3.2.4.2 Fabrication of connected and isolated pyramids	72
3.2.5 Optical Setup	75
3.2.5.1 Optical setup for nanorod experiment	75
3.2.5.2 Optical Setup for pyramid experiment	76
3.3 Results and discussion	78
3.3.1 Nanorod and nanodimers	78
3.3.2 Nanopyramids	86
3.3.2.1 Connected and non-connected pyramids	86
3.3.2.2 Regular and shaped pyramids	101
Chapter 4 Conclusion	116
Appendix (manual of nanorod synthesis)	118
References	138
Vita	153

List of Tables

Table 2.1:	Estimation of numbers of photoelectrons, shot noise limit, experimental noise and ratio of both noises under different conditions	41
Table 3.1:	The polystyrene (PS) size and the corresponding etching time	72

List of Figures

- Figure 2.1: Various mechanisms of spontaneous Raman and coherent Raman discussed in this thesis. (a) Spontaneous Raman, (b) Coherent anti-Stokes Raman scattering (CARS), and (c) Stimulated Raman scattering (SRS) (b) and (c) are coherent Raman processes. The corresponding phase-matching conditions are depicted below the diagrams.....7
- Figure 2.2: The mechanisms of (a) resonant contribution of CARS, (b) and (c) nonresonant contribution of CARS. Dash lines represent virtual states9
- Figure 2.3: (a) The comparison between Raman detuning frequency and amplitude for different modulation of the third-order susceptibility for resonant contribution (solid red line) and nonresonant contribution (dot green line) and mixed term (dash blue line). (b) The summation of all three contribution which corresponds measured CARS signal.....11
- Figure 2.4: (a) The intensity (top) and phase (bottom) of laser pulse versus wavelength used in resonance CARS experiment. (b) Measured CARS signals from cyclohexane. S_π (top) is CARS signal by applying π phase on probe. S_{ref} (middle) is reference signal. Bottom trace is normalized CARS signal S_π/S_{ref} . (c) The Raman-like spectrum of cyclohexane after FTSI procedures.....24

Figure 2.5: Spectral focusing mechanism in time-domain. (a and b) Temporal profiles of pump, Stokes and excitation field. For (a), time delay is zero. For (b), time delay is Δt . (c) is the field with shorter pulse duration. (d) Fourier transform for all excitation field from (a)-(c). The figure is a copy from our group's previous publication.....27

Figure 2.6: Spectral focusing mechanism in frequency-domain. (a) The comparison between transform-limited and stretched pulse when time delay is zero. (b) The stretched pulse can modulate different frequency by adjusting time delay Δt28

Figure 2.7: Experimental setup of resonance CARS: GR, grating; SLM, spatial light modulator; OBJ, microscope objective; S, sample; F, short wave pass filter; SP, spectrometer.....29

Figure 2.8: Optical setup of SRS. The arrow means the laser direction. M: mirror, L: lens, G: SF57 glass rod, 810ALP: 810 nm long wavelength pass filter, 790ASP: 790 nm short wavelength pass filter, PC: pockel cell, BSP: polarizing beam splitter, PD: photodiode, OBJ: objective, and S: sample.31

Figure 2.9: Laser spectrum for SRS experiment (upper panel) and corresponding phase of different wavelengths (bottom panel). Note that pump and Stokes are separate at 810 nm and the corresponding phase is quadratic.32

- Figure 2.10: The scheme of frequency modulation for SRS signal detection. (a) Pump pulse before modulation, (b) Frequency modulation by fast changing on-off state, note that the modulation frequency is 100 kHz in our experiment. (c) Pump pulse after modulation, (d) Stokes without any modulation, note that pump and Stokes initially come from the same laser source in our experiment. After interaction among modulated pump, non-modulated Stokes and the sample, (e) and (f) show SRL and SRG respectively.33
- Figure 2.11: (a) FTSI-CARS spectra of 1mM dyes in methanol and pure methanol (MeOH) (From top trace to bottom: R800, DCI', DODCI and MeOH). The shadow indicates the corresponding solvent peak. (b) The normalized absorption spectra of DODCI, DCI', and R800, dissolved in methanol, their molecular structures, and the experimental laser pulse spectrum after pulse shaping. Note that the CARS signal ranges produced by pulse shaping laser also labels on the figure.37
- Figure 2.12: (a) The FTSI-CARS spectra of R800 and DCI' under low concentration (R800, 31 μ M; DCI', 63 μ M in methanol) and compare to pure methanol. The shaded area is corresponding solvent peak. (b) Plot of intensity at 1342 cm^{-1} calibrated by methanol 1030 cm^{-1} peak intensity versus R800 concentration and its best least-squares fitting.39
- Figure 2.13: The SRS spectra of different compounds. (a) Pure toluene solution (b) From top trace to bottom are: 1M urea aqueous solution, 1M sodium nitrate aqueous solution, pure ethanol, and pure methanol solution. Acquisition time for (a) is 13.5 s and (b) is 45 s.41

Figure 2.14: The SRS spectra of (a) sodium nitrate (b) phenylalanine with different concentrations. The time constant of lock-in amplifier was 30 ms (total acquisition time was 135 s) for both (a) and (b). (c) is the plot of concentration of phenylalanine versus SRS intensity and linear fitting at 1010 cm^{-1} peak.....43

Figure 2.15: Different experimental conditions for (a) 50 mM sodium nitrate solution. From top trace to bottom: 30 ms time constant, 1 average; 100 ms, 1 average; 100 ms and 10 average (b) 22 mM phenylalanine, from top trace to bottom trace: 300 ms, 100 ms and 30 ms time constant, all are with 1 average.....44

Figure 2.16: SRS of toluene spectra for different objectives. Three spectra are taken at same condition. The y axis scales are same for all three SRS spectra.45

Figure 3.1: (a) The sphere with radius d and dielectric constant $\epsilon_1(\omega)$ is placed in the medium with dielectric constant $\epsilon_2(\omega)$. After interacting with electric field E_0 along with z direction, one can see the surface charges are induced by E_0 (b) Dimer structure with small gap under E_0 excitation54

Figure 3.2: Various reported structures with strong localized electric field enhancement (top) and corresponding simulation results in literatures. The red spots represent highest electric field position (a) junction of aggregate, (b) gap between sphere, rod, and bowtie and gap between sample and substrate (c) sharp tip (d) crescent (e) V-groove (g) void..59

Figure 3.3: The synthesis procedures of anodized aluminum oxide (AAO) template65

Figure 3.4: The synthesis procedures of nanorods and nanodimers by template method.....	66
Figure 3.5: TEM images of (a) silica coated nanorods and (b) etched nanodimers	67
Figure 3.6: The scheme of fabrication of regular pyramid and shaped pyramid	69
Figure 3.7 The scheme of connected pyramid and isolated pyramid synthesis .	70
Figure 3.8: The SEM images of RIE treatment effect on self-assembled polystyrene beads (a) 3 μm polystyrene beads without RIE treatment, All polystyrene are closed packing. (b) 3 μm polystyrene beads with 6 min RIE treatment (see text for detailed recipes) Scale bar for (a): 10 μm , (b) 2 μm	73
Figure 3.9: The plot of RIE etching time versus the remaining polystyrene (PS) diameter for two sizes of polystyrene beads: (a) 3 μm , (b) 6 μm	74
Figure 3.10: Optical setup for nanorod project where white light scattering and femtosecond laser are combined together. The arrows mean the laser direction. M: mirror, L: lens, GR: grating, SLM: spatial light modulator, HWP: half wave plate, BS: beam splitter, WL: white light, SP: spectrometer OBJ: objective, and S: sample.....	76
Figure 3.11: Optical setup for pyramid project where two lasers are combined together. The arrows mean the laser direction. M: mirror, L: lens, F: filter, P: polarizer GR: grating, SLM: spatial light modulator, DRLP: dichroic long pass filter HWP: half wave plate, BS: beam splitter, WL: white light, SP: spectrometer, PD: photodiode, OBJ: objective, and S: sample.	78

Figure 3.12: DDA simulation results for nanodimers (a) scattering spectra (b) near field spectra (c) the contour of square modulation of field whose excitation wavelength is 790 nm.....	80
Figure 3.13: The correlation experiment of scattering image, TPL image, scattering spectra and corresponding SEM image.....	82
Figure 3.14: The photostability test of coated (a-c) and uncoated (d-f) nanoparticles, both panels are scan for three times under 300 μ W , the color scale for top panel is from 0 to 1.1, and the bottom panel is from 0 to 0.8.	83
Figure 3.15: (a) TPL scanning image (Excitation wavelength is 790nm) (b) The dependence of TPL signal and power (c) TPL excitation spectra	84
Figure 3.16: (a) TPL scanning image (Excitation wavelength is 790nm) (b) FWM scanning image (Excitation wavelength is 760nm and 845nm) (c) The spectra of TPL (red line) and FWM (black line) under similar condition (d) Normalized TPL and FWM spectra	85
Figure 3.17: SEM images for different fabrication stages (a) silicon wafer after KOH etching. One can clearly see inverse pyramid pits. (b) KOH etched pyramid pits deposited thin gold layer. 50 nm gold layers are used here. (c) Stripped gold pyramid.	87
Figure 3.18: Benzenethiol SERS spectrum. Three peak positions around 1000 cm^{-1} are 996, 1022 and 1071 cm^{-1} respectively. * represents the peak integrated to acquire SERS image	88

Figure 3.19: Three representative samples of large area pyramids (a)-(c), their SERS images (left panel) and corresponding SEM images (right panel). Note that the center of both SERS and SEM images are not exactly same. The numbers on SERS image axis represent actual scanning distance (μm). The scale of SERS images are same for three samples90

Figure 3.20: SEM images of two different types of pyramids: (a) connected pyramids (b) isolated pyramids.....91

Figure 3.21: (a)-(c): Three examples of small aggregate pyramids, SERS images (left panel) and corresponding SEM images (right panel). The scales of SERS images are from 0 to 500 and same for all three samples. The acquisition time is 0.1 sec for each step. The numbers on SERS image axis represent actual scanning length (μm).....96

Figure 3.22: The example of small aggregate non-connected pyramids with high SERS signals. Left panel is SERS image and right panel is SEM image.97

Figure 3.23: (a) and (b): The power dependence plots of two examples. The slopes are 1.81 and 1.96 respectively.97

Figure 3.24: (a)-(c): Three examples of small aggregate pyramids fabricated by oxygen plasma processes, Pyramids are well separated from each other. Left panel is SERS images and right panel is SEM images. The scale of SERS images are from 0 to 200 and same for all three samples. The acquisition time is 0.5 sec for each step.....98

Figure 3.25: Four examples of small aggregate pyramids Their SERS, TPL and SEM images. (a)-(c) sample 1, (d)-(f) sample2, (g)-(i) sample 3 and (j)-(l) sample 4. The red arrows are polarization direction of both lasers.100

Figure 3.26: EDX spectrum of shaped pyramid after peeling from wafer substrate.106

Figure 3.27: (a) Scattering image of single pyramid collected by a photodiode. (b) SERS image in same region of (a). (c) The overlap of (a) and (b), Dash circle line represents the circle in (a). The SERS spots are at bottom left, upper left, and right of circumference.....106

Figure 3.28: The different angle SEM images of regular single pyramid and shaped single pyramid. (a) top view (b) tilt 25 degree (c) tilt 70 degree.107

Figure 3.29: SERS images (left panel) and TPL images (right panel) of shaped pyramid of sample 1. Red arrows are polarization directions: (a) polarization is x direction (b) polarization is y direction. The numbers 1-4 on the images represent the four corners of shaped pyramid, same as SEM images in Figure 3.30.108

Figure 3.30: SEM images of shaped pyramid of sample 1. The top view is in the middle of the images. The other four are high tilt angle images of four corners labeling with different numbers from 1 to 4.109

Figure 3.31: SERS images (left panel) and TPL images (right panel) of shaped pyramid of sample 2. Red arrows are polarization directions: (a) polarization is x direction (b) polarization is y direction. The numbers 1-4 on the images represent the four corners of shaped pyramid, same as SEM images in Figure 3.32.110

Figure 3.32: SEM images of shaped pyramid of sample 2. The top view is in the middle of the images. The other four are high tilt angle images of four corners labeling with different numbers from 1 to 4.111

Figure 3.33: SERS images (left panel) and TPL images (right panel) of shaped pyramid of sample 3. Red arrows are polarization directions: (a) polarization is x direction (b) polarization is y direction. The numbers 1-4 on the images represent the four corners of shaped pyramid, same as SEM images in Figure 3.34.112

Figure 3.34: SEM images of shaped pyramid of sample 3. The top view is in the middle of the images. The other four are high tilt angle images of four corners labeling with different numbers from 1 to 4.113

Figure 3.35: SERS images (left panel) and TPL images (right panel) of shaped pyramid of sample 4. Red arrows are polarization directions: (a) polarization is x direction (b) polarization is y direction (c) polarization is +45 degree (d) polarization is -45 degree. The numbers 1-4 on the images represent the four corners of shaped pyramid, same as SEM images in Figure 3.36.....114

Figure 3.36: SEM images of shaped pyramid of sample 4. The top view is in the middle of the images. The other four are high tilt angle images of four corners labeling with different numbers from 1 to 4.115

Chapter 1: Introduction

Nowadays many researchers investigate molecular properties in complex systems especially in biological systems¹. They usually combine optical microscopy and spectroscopy to investigate these complex biological systems. High spatial resolution and specific chemical selectivity are key elements for both microscopy and spectroscopy techniques.

Traditional transmission microscopy is the most common microscopy². The optical contrast of it comes from the refractive index distribution of the sample. The advantage of transmission microscopy is that samples do not need to be labeled with dyes, and morphology information can be obtained instantly. However, it lacks chemical selectivity because sample images are generated by refractive index contrast rather than chemical properties such as electronic transition, vibration, and rotation of molecules.

Fluorescence is the most common choice of microscopy in biological researches³. The contrast of fluorescence comes from the fluorescence quantum yield (QY) of various species, and therefore, labeling high QY emitters is necessary for the low QY molecules. Fluorescence microscopy is widely used in these days because the confocal technique can improve the resolution^{1, 3}, and various fluorescent probes have developed to bind to specific chemical structures³. Although there are great advantages of fluorescence microscopy, there are still a lot of limitations for fluorescence microscopy. For example, the amount of dye binding to a target molecule is always questionable. Furthermore, the photobleaching problem and the perturbations to systems by fluorescent dyes also hinder the application of fluorescence microscopy.

Vibrational microscopy based on infrared (IR) and Raman spectroscopy is another choice to have chemical imaging of the sample without any perturbation. Both of them

can obtain the information of functional groups, and their spectra in the fingerprint region are particularly useful. IR has similar orders of magnitudes of absorption cross section to fluorescence⁴. Hence, IR has signals as strong as fluorescence. Although IR is a powerful tool, the limited spatial resolution due to long absorption wavelength makes the biological application very difficult. Water absorption in IR region cannot be ignored, either.

Raman spectroscopy is a complementary technique to IR and is commonly used in many biological systems⁵. Because of the shorter excitation wavelength, Raman has better spatial resolution than IR. Also, water only has a very tiny Raman signal. Thus, Raman is a possible choice to study the properties of biological systems. However, Raman scattering has very small cross section ($\sim 10^{-30} \text{cm}^2$, 10^{14} times smaller than fluorescence)⁶, which makes the signal extremely weak. As a result, it takes long time to acquire enough Raman signals to obtain sample images. For example, Hamaguchi group investigated living yeast cell by Raman spectroscopy⁷. They usually spent 100 seconds for a single time-resolved Raman spectrum, and 20 minutes for a Raman mapping experiment. Therefore, it is important to develop a fast and convenient way to obtain Raman spectra of biological samples.

Generally speaking, there are several types of techniques which researchers have been trying to develop in order to increase the intensity of Raman signals. In this dissertation, I study two of these techniques, coherent Raman scattering⁸ and surface enhanced Raman scattering^{6,9}. Coherent Raman scattering uses coherent light excitation of two different frequencies, ω_1 and ω_2 , to drive a vibrational Raman field whose frequency is $\omega_R = \omega_1 - \omega_2$. The nature of the coherent light excitation enhances Raman signal enormously. The coherent Raman processes include Coherent anti-Stokes Raman spectroscopy (CARS) and Stimulated Raman spectroscopy (SRS).

For CARS, our group have applied the Fourier transform spectral interferometry (FTSI)¹⁰ to CARS and successfully retrieved Raman-like vibrational spectra from the notorious nonresonant signal. Here, we apply this technique to investigate resonance-enhanced CARS. It is well-known that the resonance effect can amplify the Raman signals⁵. We choose different dyes to study the resonance effect in CARS, and our results show that we can retrieve the background-free vibrational spectra and can improve the detection limit for several orders with the assistance of resonance effect. For SRS, we develop an easier and cheaper SRS technique based on spectral focusing mechanism¹¹. Several groups have already demonstrated spectral focusing mechanism in CARS¹¹. Here, we apply the spectral focusing mechanism to SRS. We examine the feasibility and detection limits of our SRS technique by different standard Raman samples. The lock-in detection and divider circuit push the sensitivity 10 times over the shot-noise limit.

Surface enhanced Raman scattering (SERS) is another way to amplify Raman signals with the assistance of noble metal nanoparticles (such as gold and silver)^{6, 9}. Briefly, because of the inherent properties of noble metal nanoparticles, the surface electrons can be oscillated coherently, the so-called surface plasmon¹². As a result, local electromagnetic field of noble metal nanoparticles can be enhanced several orders to amplify the Raman signals of samples on nanoparticles.

In the second part of this dissertation, we synthesize two kinds of samples, nanogaps and pyramids, by template methods to examine the relationship between local electromagnetic field and SERS. Two-photon luminescence (TPL) has been proven a great tool to probe local field enhancement¹³, and therefore, we use TPL to study local field enhancement. The general consensus of SERS theory is that SERS signals are highly related to local field enhancement, and local field enhancement is also closely

related to the properties of samples such as size, shape, and the dielectric constant of samples.

We first conduct SERS experiments and find SERS signals are very sensitive to the sample structures and polarization of incident laser. Because of the extreme sensitivity, structure differences of few nanometers may lead to observable signals change. It is still difficult for us to synthesis the desired structures with nanometer precision. Next, we examine the correlation between SERS and TPL and the morphology by scanning electron microscopy (SEM). Like other researchers, we find that high SERS and TPL signals are along with the gap structure^{6, 14}. However, both SERS and TPL are not completely spatially correlated. According to literature, we believe that SERS and TPL have similar excitation pathways but different relaxation pathways. These different relaxation pathways could be one possible explanation for the vague correlation between SERS and TPL. Another possibility is the coupling frequencies of both processes and localized plasmon structures are different. For SERS, coupling frequencies are incident laser frequency and Raman scattering frequency which is smaller than laser frequency. For TPL, coupling frequencies are incident light and frequency of TPL illumination which is larger than incident frequency. If we consider the difference between coupling frequencies and local plasmon structures, there are still some possibilities TPL and SERS are not totally correlated with each other.

In conclusion, we successfully build coherent Raman scattering systems including CARS and SRS and demonstrate amplified Raman signals in both systems. Our coherent Raman setup can retrieve background-free Raman spectra and is simpler than other groups' work¹⁵. We also obtain satisfying the sensitivity of Raman signals. For SERS project, we successfully synthesize different noble metal nanoparticle samples and investigate their SERS activity. We also build an optical system to obtain optical images,

spectra, and morphology simultaneously. We observe sensitive SERS and TPL signals change with structure but unclear correlation between them. The detailed theory, experimental setup, results and discussion are provided in the following chapters.

Chapter 2: Coherent Raman Scattering

2.1 INTRODUCTION

2.1.1 Spontaneous Raman versus Coherent Raman process

In 1928, Raman discovered a new type of spectroscopy. He found that after interacting with molecules, the monochromatic light with frequency ω_p is scattered with frequency not only the original frequency ω_p (Rayleigh scattering) but also the one with other frequencies $\omega_p \pm \omega_R$ ⁵. He and other researchers soon realized that the frequency difference between incident photon and scattered photon corresponds to a molecule intrinsic property—vibrational motion. As stated in chapter 1, Raman scattering can provide rich chemical information, so many extended techniques of Raman scattering have been developed since then⁵. However, Raman scattering is extremely weak, and the efficiency^{5b} is only 10^{-6} - 10^{-8} . It restricts the application of Raman scattering.

Coherent Raman techniques provide a possible solution for application of Raman scattering. In coherent Raman techniques, two different frequencies of pump fields ω_p and Stokes field ω_s , form a beat with frequency $\omega_p - \omega_s$ ¹⁶. When beat frequency $\omega_p - \omega_s$ matches with vibration frequency of a molecule, the beat drives the molecule to oscillate coherently¹⁶. One can treat this problem as a classical harmonic oscillator and solve the equation to see the coherent effect. Later, we will use harmonic oscillator model to illustrate Stimulated Raman scattering.

So far, we only discuss the situation that a molecule is driven by the beat. However, each sample contains enormous numbers of molecules, and all of them oscillate when interacting with pump and Stokes fields¹⁶. If each oscillator has different phase from each other, the destructive interference caused by each oscillator makes the net output field negligible¹⁶. When all oscillators oscillate in the same phase, the

constructive interference occurs and gives strong signal enhancement. In order to obtain the induced oscillators oscillating in the same phase, the phases of coherent driving fields require fulfilling the certain condition, the so-called phase matching condition¹⁶. In conclusion, Raman scattering can be enhanced several orders of magnitude if coherent excitation and phase-matching condition are fulfilled^{8, 16}.

Two coherent Raman processes, coherent anti-Stokes Raman scattering (CARS) and stimulated Raman scattering (SRS), are discussed in this chapter. Figure 2.1 compares the (a) spontaneous Raman, (b) coherent anti-Stokes Raman, and (c) stimulated Raman¹⁶⁻¹⁷. The corresponding phase-matching conditions also depict below the energy diagram. Note that for stimulated Raman scattering, the phase-matching condition is automatically fulfilled¹⁶. The detailed explanation of each coherent process and each terminology will be illustrated in following sections.

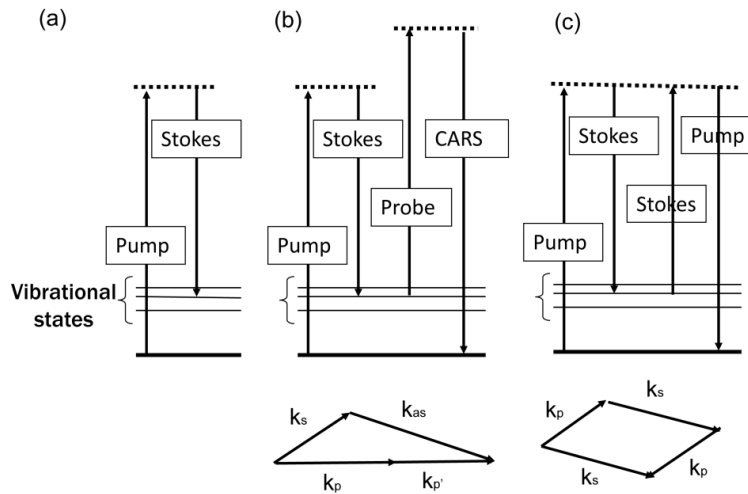


Figure 2.1: Various mechanisms of spontaneous Raman and coherent Raman discussed in this thesis¹⁶⁻¹⁷. (a) Spontaneous Raman, (b) Coherent anti-Stokes Raman scattering (CARS), and (c) Stimulated Raman scattering (SRS) (b) and (c) are coherent Raman processes. The corresponding phase-matching conditions are depicted below the diagrams.

2.1.2 Introduction to CARS¹⁷

Coherent anti-Stokes Raman scattering (CARS) is a third order nonlinear vibrational spectroscopy technique, which excites coherent vibration with beating frequency between pump pulse ω_p and Stokes pulse ω_s , followed by the third pulse (probe ω_{pr}) to generate anti-Stokes signals at the frequency ω_{as} ($\omega_{as} = \omega_p - \omega_s + \omega_{pr}$)¹⁷. Typically, pump and probe pulses are chosen from the same laser, $\omega_p = \omega_{pr}$ and $E_p = E_{pr}$, where E is electric field for the convenient reason. Like other nonlinear optics processes such as sum frequency generation (SFG)¹⁶, phase matching condition needs to be fulfilled, which can be expressed mathematically: $\Delta k = k_{as} - 2k_p + k_s = 0$, where k is the wave vector of each pulse¹⁷. In early stage of CARS, careful alignment of the incident excitation beam geometry was the key to accomplish the phase matching condition. In 1999, Zumbusch and Xie found that using high numerical aperture (NA) objectives can relax the phase matching condition¹⁸. After incident beams pass through the high numerical aperture objectives, the large cone of wave vectors due to tightly focused beams leads to fulfill the phase matching condition¹⁸.

For CARS process, excitation pulses have to overlap temporally and spatially to produce the blue-shifted CARS signals I_{CARS} , which is proportional to the square modulus of the induced third-order nonlinear polarization¹⁷, $p^{(3)}$, $I_{CARS} \propto |p^{(3)}|^2$. Also, the induced nonlinear polarization is proportional to the nonlinear susceptibility $\chi^{(3)}$ and electric field E. Therefore, $I_{CARS} \propto |p^{(3)}|^2 = |\chi^{(3)} E_p^2 E_s^*|^2$. Typically, there are two kinds of contributions of CARS signals – resonance and nonresonance signals¹⁷. The resonance signals come from the vibrational frequency Raman modes (Figure 2.2(a))¹⁷. The anti-Stokes field not only drives vibrational frequency Raman mode but also drives the electron clouds to oscillate at the frequency ω_{as} coherently¹⁷. This pure electronic oscillation is the source of nonresonance signals¹⁷. Hence, we can separate the nonlinear

susceptibility $\chi^{(3)}$ into resonant ($\chi_R^{(3)}$) and nonresonant ($\chi_{NR}^{(3)}$) part, and $\chi^{(3)} = \chi_R^{(3)} + \chi_{NR}^{(3)}$. According to advanced theory, resonant susceptibility is $\chi_R^{(3)} = \frac{A_R}{\Omega - (\omega_p - \omega_s) - i\Gamma_R}$, where A_R is constant related to the Raman scattering cross section, Γ_R is the half-width at half-maximum of the Raman peak, and Ω is the center frequency of the vibrational frequency of Raman peak¹⁷. Some researchers¹⁷ define Raman detuning frequency $\Delta = \Omega - (\omega_p - \omega_s)$, and thus, $\chi_R^{(3)} \propto \frac{1}{\Delta - i\Gamma_R}$.

For nonresonant signals, two possible contributions are depicted in Figure 2.2(b) and (c)¹⁷. Figure 2.2(b) describes the beat frequency ($\omega_p - \omega_s$) drives at virtual state, instead of resonant vibrational state¹⁷. Another possible contribution is two-photon enhanced nonresonant contribution (Figure 2.2(c)), where the energy of $2\omega_p$ is closed to the energy between the real electronic excited state and ground state¹⁷. Typically, nonresonant contribution is treated as a real number and approximately same for all frequencies.

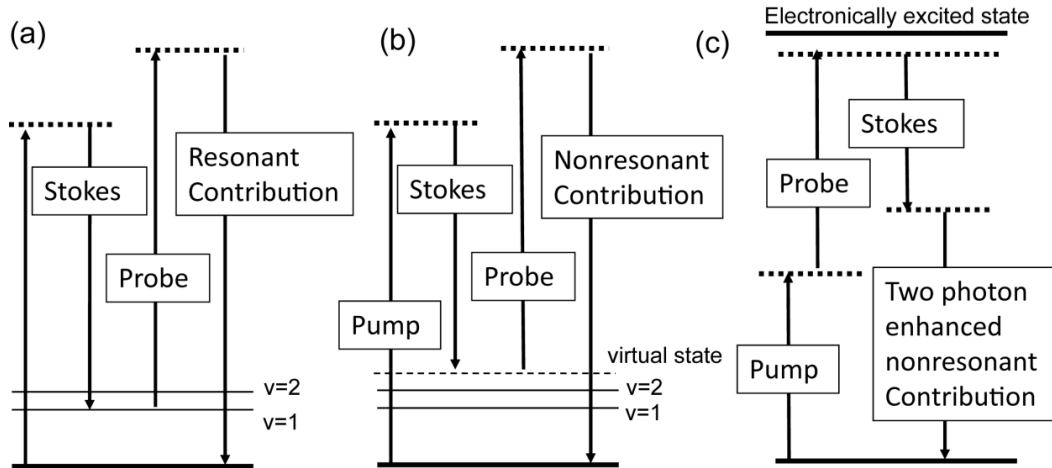


Figure 2.2: The mechanisms of (a) resonant contribution of CARS, (b) and (c) nonresonant contribution of CARS¹⁷. Dash lines represent virtual states

As discussing previously, the intensity of CARS signal can be written as¹⁷:

$$I_{CARS} \propto \left| \chi_R^{(3)} + \chi_{NR}^{(3)} \right|^2 I_p^2 I_S = \left(\left| \chi_R^{(3)} \right|^2 + \left| \chi_{NR}^{(3)} \right|^2 + 2\chi_{NR}^{(3)} \text{Re}\left\{ \chi_R^{(3)} \right\} \right) \times I_p^2 I_S \quad (2.1)$$

Therefore, CARS signals can be separated into three part, the resonant contribution (first term), the nonresonant background (second term), and the mixture of resonant and nonresonant contribution (the cross term). Because $\chi_R^{(3)} \propto \frac{1}{\Delta - i\Gamma_R}$, we can expect $\left| \chi_R^{(3)} \right|^2$ has Lorentzian line shape¹⁷. In addition, the cross term has dispersive lineshape due to mixing nonresonant susceptibility with the real part of the resonant susceptibility¹⁷. Non-resonance background interferes with resonance signals and makes lineshape different from spontaneous Raman scattering¹⁷. A simple comparison among three contributions is plotted in Figure 2.3(a)¹⁷. After adding three terms, CARS spectrum is plotted in Figure 2.3(b)¹⁷. Compared to the vibrational Raman peak (resonant contribution), the peak of CARS spectrum is red-shifted and has a negative dip at blue frequency¹⁷. This blue frequency dip produces negative contrast¹⁷ and deteriorates the image quality in microscopy application. In biological systems, the numbers of samples are usually low, and the cross sections of vibrational Raman peaks are also small. In addition, the nonresonant background signals from the surrounding water are extremely high. Therefore, after abundant nonresonant background signals interfere with resonant vibrational signals, the line shapes of CARS spectrum are broadened and distorted even more seriously than the one depicted in Figure 2.3(a). This serious spectral distortion restricts CARS application in biological systems. Hence, suppression of nonresonant signals is critical to have further application of biological system imaging¹⁷.

Researchers have been developed many techniques to reduce the nonresonant contribution in CARS such as epi-detection (E-CARS)¹⁷, polarization methods (p-CARS)¹⁷, time-resolved CARS (t-CARS)¹⁷, and phase modulation methods¹⁹. Below, we

will briefly introduce these methods. Because the phase modulation method not only can reduce the nonresonant signal but also can obtain great spectral resolution with broadband laser, we applied this technique to both CARS and SRS. Hence, phase modulation methods are the key technique in the first part of this dissertation, and more detailed discussion is provided in section 2.1.4.

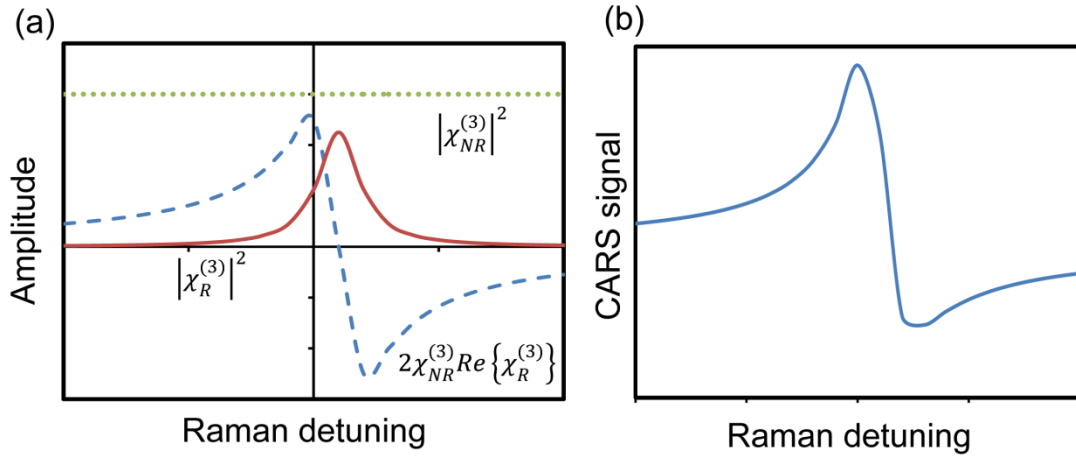


Figure 2.3: (a) The comparison between Raman detuning frequency and amplitude for different modulation of the third-order susceptibility for resonant contribution (solid red line) and nonresonant contribution (dot green line) and mixed term (dash blue line). (b) The summation of all three contribution which corresponds measured CARS signal¹⁷

Theory, simulation and experimental details of E-CARS are demonstrated in literatures²⁰. In brief, after driving by beat frequency, particles can be considered as an oscillating dipole, which can be treated by classical electrodynamics. If the particle size is small, the radiation pattern of the oscillating dipole distributes equally in both forward and backward direction. However, if particle size is large, the distribution of radiation pattern is mainly localized in forward direction. In other words, for thick sample (~large particle), constructive interference occurs in forward direction, and destructive

interference occurs in backward direction. Typically, in biological samples, the surrounding water is the main source of nonresonant signals. One can think surrounding water is much larger than the samples. Therefore, nonresonant signals resulting from surrounding water can be minimized in the backward direction, and resonance vibrational signals remain same in both directions.

Based on the difference of polarization direction between nonresonant signals and resonant signals, p-CARS is also used to suppress the nonresonant signals²¹. As discussed in literature²¹, we consider polarization of incident light perpendicular to incident plane. Because molecules have their own symmetry and vibration modes, the polarization of Raman scattering is not necessary to have the same direction as incident light. Researchers define depolarization ratio $\rho = I_{\perp}/I_{\parallel}$, where I_{\perp} is the intensity of Raman scattering whose polarization is perpendicular to incident plane, and I_{\parallel} is the one parallel to the incident plane. The depolarization ratio is closely related to the symmetry of molecules, so various values (from 0 to 0.75) are expected⁵. However, if one assumes the nonresonant signals are isotropic and transparent (lossless), the depolarization ratio is equal to 1/3 according to the theory²¹. It is almost true for surrounding water in biological samples. Therefore one can place an analyzer (polarizer) in front of the detector to minimize the nonresonant signals by knowing the depolarization ratio of both samples and nonresonant signals.

Similar to the p-CARS, time-resolved CARS (t-CARS) separate both nonresonant signals and resonant signals from mixed signals by their specific properties²². P-CARS use the difference of polarization orientation between nonresonant signal and resonant signals. On the other hand, t-CARS use the different temporal behaviors to suppress nonresonant signals. Typically, the origin of nonresonant signals is from the electronic response. The electronic response is instantaneous to the excitation field (i.e. response

time ~ 0). However, the dephasing time of resonant vibrational contribution is usually several hundred femtoseconds²². Hence, by controlling suitable delay between pump and probes fields, the nonresonant signals can be suppressed.

Although p-CARS and t-CARS have been demonstrated to remove nonresonant signals efficiently, both methods also significantly decrease the resonant signals¹⁷. Therefore, it is necessary to have a better way to maintain the resonant signals and suppress the nonresonant signals for CARS application in biological research. One possible way is the phase modulation technique, mainly developed by Silberberg group¹⁹. Our group also has developed a series of techniques based on Silberberg's work. For completeness of this thesis, we will introduce Silberberg's work in section 2.1.4.1.

Another important issue of CARS microscopy is the choice of excitation laser source¹⁷. First of all, near-infrared (NIR) light can penetrate biological samples deeperly than UV and visible light. Also, NIR causes less multiphoton absorption photodamage, which is the main problem in the most multiphoton bio-imaging techniques. A pulse laser is used in most nonlinear optics including CARS, and the pulse duration is directly related to spectral resolution¹⁷. Typically, a broadband laser has poor spectral resolution. In addition, the broadband laser leads to serious nonresonant contributions as described earlier. Therefore, researchers have used narrowband laser to suppress nonresonant signals and increase spectral resolution¹⁷. However, the broadband laser has the advantage of wide spectral ranges. Compared to traditional point-by point acquisition of CARS spectra by tuning the narrowband laser, the broadband laser can provide flexible spectral ranges to obtain more spectroscopic information simultaneously¹⁷. Some researchers attempted to combine advantage of both narrowband and broadband laser (For example²³). They used narrowband laser as pump to obtain high spectral resolution

and broad-band laser as Stokes to have adjustable spectral range²³. The technique is so-called “multiplex CARS²³.”

CARS requires both pump and Stokes laser to interact on samples simultaneously. Synchronization is the key to achieve this requirement if two individual lasers are used independently¹⁷. One problem of synchronization is pulse jitter, and it causes CARS intensity fluctuation¹⁷. Few research groups including us use single broadband pulse served as both pump and Stokes to avoid synchronization^{10, 17, 19}.

2.1.3 Introduction to SRS^{16, 24}

Stimulated Raman scattering (SRS) is another coherent Raman scattering technique. Similar to CARS, SRS is also a four-wave mixing process and needs two coherent lasers (pump and Stokes) to excite the sample^{16, 24}. As we discussed in previous section, the frequency of pump ω_p , the frequency of Stokes ω_s , and the frequency difference of pump and Stokes $\Delta = \omega_p - \omega_s$ should match with the specific frequency which corresponds to the molecular vibration frequency. However, there are many differences between CARS and SRS. First of all, CARS and SRS detect different signals. In CARS, a new anti-Stokes frequency ω_{as} is generated by mixing two pump photons and one Stokes photon to make $\omega_{as} = 2\omega_p - \omega_s$. The new frequency is higher than both pump and Stokes. In SRS, instead of generated the new frequency, a pump photon is converted into a Stokes photon after interacting with the sample^{16, 24-25}. Therefore, we detect intensity change of pump or Stokes in SRS. We expect to detect intensity loss for pump laser but intensity gain for Stokes^{16, 24, 25b}.

Another difference is that CARS is required to fulfill the phase matching condition $\Delta k = 2k_p - k_s - k_{as} = 0$, but it is automatically fulfilled in SRS^{16, 24, 25b}. In addition, CARS is seriously suffered from the notorious nonresonant background, which

results from the fast electronic response. The CARS spectra are different from spontaneous Raman spectra; however, SRS is totally free from the nonresonant background, and the SRS spectra are the same as spontaneous Raman scattering in theory^{16, 24-25}.

We can use a simple classical harmonic oscillator model to illustrate the SRS phenomenon, and we will closely follow arguments in Boyd's book¹⁶ to discuss this question. Consider a one dimensional harmonic oscillator with reduced mass m , vibration frequency ω_v , and damping constant γ . If we apply any force $F(t)$ to this harmonic oscillator system, the equation of motion can be written as¹⁶

$$\frac{d^2q}{dt^2} + 2\gamma \frac{dq}{dt} + \omega_v^2 q = \frac{F(t)}{m} \quad (2.2)$$

where $q(t)$ is the coordinate of intermolecular distance

To discuss nonlinear effect, we also need to consider polarizability of molecules $\alpha(t)$, and $\alpha(t)$ depends on the intermolecular distance $q(t)$. Therefore, we can expand it by first order Taylor expansion.¹⁶

$$\alpha(t) = \alpha_0 + \left(\frac{d\alpha}{dq}\right)q(t) \quad (2.3)$$

Furthermore, in the presence of electric field $E(x,t)$, the induced dipole moment p and work restoring in the system W can be written as¹⁶

$$p(x, t) = \varepsilon_0 \alpha E(x, t) \quad (2.4)$$

$$W = \frac{1}{2} \varepsilon_0 \alpha \langle E^2(x, t) \rangle \quad (2.5)$$

where ε_0 is vacuum permittivity. Also, the bracket means taking average with respect to time. Therefore, the force applied to the system can be expressed as¹⁶

$$F(x, t) = \frac{dW}{dq} = \frac{\varepsilon_0}{2} \left(\frac{d\alpha}{dq}\right) \langle E^2(x, t) \rangle \quad (2.6)$$

For SRS, we know that we need both pump and Stokes fields to coherently excite the sample. Hence, we can assume the electric field applying to this system is¹⁶

$$E(x, t) = [A_p e^{i(k_p x - \omega_p t)} + A_s e^{i(k_s x - \omega_s t)}] + c. c \quad (2.7)$$

where p and s present pump and Stokes respectively. After plugging electric field into equation of force (Equation 2.6) and rearrange the equation, we can obtain the applied force equation at beat frequency $\Omega = \omega_p - \omega_s$

$$F(x, t) = \varepsilon_0 \left(\frac{d\alpha}{dq} \right) [A_p A_s^* e^{i(Kx - \Omega t)} + c. c] \quad (2.8)$$

where $K = k_p - k_s$. Next, we can find a solution of $q(t)$ to the harmonic oscillator equation under the driving force shown as previous equation¹⁶. We can use trial solution $q = q(\Omega) e^{i(Kx - \Omega t)} + c. c$ to solve the equation. After few steps calculation, we can find $q(\Omega)$ is equal to¹⁶

$$q(\Omega) = \frac{(\varepsilon_0/m)(d\alpha/dq)A_L A_s^*}{\omega_v^2 - \Omega^2 - 2i\Omega\gamma} \quad (2.9)$$

where ω_v is vibration frequency. We know that the polarization P of whole medium is $P = Np(x, t) = \varepsilon_0 N \alpha E$, which N is number of molecules. In order to simplify the question, we only consider nonlinear polarization P^{NL} at frequency ω_s here¹⁶.

$$P_S^{NL}(x, t) = \frac{(N\varepsilon_0^2/m)(d\alpha/dq)^2 |A_p|^2 A_s}{\omega_v^2 - \Omega^2 + 2i\Omega\gamma} e^{ik_s x} e^{-i\omega_s t} + c. c \quad (2.10)$$

We can define Raman susceptibility according to this equation¹⁶

$$P_S^{NL}(x, t) = 6\varepsilon_0 \chi_R(\omega_s) |A_p|^2 A_s e^{ik_s x} e^{-i\omega_s t} + c. c \quad (2.11)$$

Therefore, we can express Raman susceptibility as¹⁶

$$\chi_R(\omega_s) = \frac{(N\varepsilon_0/6m)(d\alpha/dq)^2}{\omega_v^2 - \Omega^2 + 2i\Omega\gamma} \quad (2.12)$$

When we consider the vibrational resonance, which means $\omega_v^2 = \Omega^2$, we obtain

$$\chi_R(\omega_s) = \frac{(N\varepsilon_0/6m)(d\alpha/dq)^2}{2i\Omega\gamma} = -i \frac{(N\varepsilon_0/6m)(d\alpha/dq)^2}{2\Omega\gamma} \quad (2.13)$$

Note that the Raman susceptibility is pure negative imaginary number under vibrational resonance condition, and this is the reason why Stokes field experiences gain. If we only

consider the simplest condition which pump field is undepleted and apply slow varying envelope approximation, we can obtain

$$\frac{dA_S}{dx} = -\alpha_S A_S = 3i \frac{\omega_S}{n_S C} \chi_R(\omega_S) |A_p|^2 A_S \quad (2.14)$$

where n_S is the refractive index at Stokes frequency. At resonance, it becomes¹⁶

$$\frac{dA_S}{dx} = 3i \frac{\omega_S}{n_S C} \chi_R(\omega_S) |A_p|^2 A_S = \frac{3\omega_S (N\varepsilon_0/6m)(d\alpha/dq)^2}{2\Omega\gamma} |A_p|^2 A_S \quad (2.15)$$

One can easily see that the coefficient of A_S is a positive number at right hand side of the equation, and there is no phase matching condition involved in this equation. The solution of equation 2.15 is exponential function and grows with increase of the medium thickness x . Therefore, we can explain automatic phase matching condition and gain of Stokes field by this simple harmonic oscillator model. Also, it is obvious that SRS signals are proportional to the imaginary part of Raman susceptibility at resonance, and the lineshape of SRS is the same as spontaneous Raman. There are still many more complicated situations such as depleted pump and mixing Stokes and anti-Stokes, which we do not discuss here. Boyd's book¹⁶ and Power's book²⁴ both provide detailed discussion of these situations. Also, Shen's book uses density matrix theory to explain SRS²⁶.

CARS signals demonstrate quadratic concentration dependence in high concentration limit and linear concentration dependence in low concentration limit¹⁷. It can be explained by equation 2.1.

$$I_{CARS} \propto \left| \chi_R^{(3)} + \chi_{NR}^{(3)} \right|^2 I_p^2 I_S = \left(\left| \chi_R^{(3)} \right|^2 + \left| \chi_{NR}^{(3)} \right|^2 + 2\chi_{NR}^{(3)} \text{Re}\{\chi_R^{(3)}\} \right) \times I_p^2 I_S \quad (2.1)$$

At high concentration of analyte, the first term dominates, so quadratic dependence is expected (homodyne detection). At low concentration, interference between analyte and background (the third term) dominates the signals, so linear concentration dependence is expected (heterodyne detection)^{10, 17}. In the contrast to CARS, SRS detects the intensity

change of pump (loss) or Stokes (gain), and linear concentration dependence is expected^{25b}. In other words, we can consider total detected signals for pump loss is $I_p \propto |E_p + E_{sig}|^2$, where E_p is pump field and E_{sig} is signal field. It is straightforward to expand the equation to obtain²⁷

$$I_p \propto |E_p|^2 + 2E_p E_{sig} + |E_{sig}|^2 \quad (2.16)$$

The first term can be treated as an offset, and the third term is so small that we can neglect it. Hence, it is clear now that the detection mechanism of SRS is the same as detection mechanism of heterodyne CARS. Furthermore, by applying similar arguments of previous harmonic oscillator model under weak signal limit $E_{sig} \ll E_p$, the change of signals after passing through distance L can be given by²⁷

$$\Delta I_p = I_p(L) - I_p(0) \approx -\frac{3\omega_p\mu_0}{n_p n_s \epsilon_0} \text{Im}[\chi_R^{(3)}] I_p(0) I_s(0) L \propto -\text{Im}[\chi_R^{(3)}] I_p(0) I_s(0) \quad (2.17)$$

From this equation, we can easily see the linear dependence of concentration and laser intensity of pump and Stokes. Also, SRS depends on $\text{Im}[\chi_R^{(3)}]$, which gives same spectra lineshape as spontaneous Raman.²⁷⁻²⁸

Because SRS is linearly proportional to concentration, free of nonresonant background, and has the same spectral lineshape as spontaneous Raman, SRS may have more potential in biological imaging application than CARS^{25b, 29}. Another application for SRS is probing ultrafast chemical dynamics. Mathies' group has been developed femtosecond SRS techniques to investigate the excited state vibrational structure dynamical information such as cis-trans isomerization of retinal^{15, 25a, 28, 30}.

Although SRS shows promising potential for biological imaging application, SRS suffers from huge laser noise. In early SRS work of imaging, high laser pulse power is used to obtain observable signals. For example, Ploetz et al had used amplified femtosecond laser system with 1 kHz repetition rate, 270 nJ pulse energy, and the

photodiode array detector to image polystyrene beads³¹. Although they had satisfied results from this amplified laser system, such high peak power easily damages biological samples and is not a good choice for biological imaging. Since then, several groups have used quiet mode-locked picosecond or femtosecond laser with 76 MHz repetition rate, ~few nJ pulse energy and lock-in detection to obtain biological imaging independently^{27, 29a, 32}. Their detection sensitivities were increased several orders of magnitude with much lower peak power.

The key of their techniques in SRS application was to modulate pump or Stokes laser at high frequency (MHZ) by electrooptical modulator (EOM) or acousto-optic modulator (AOM) and then retrieve the signals from laser noise by lock-in amplifier^{27, 29a, 32}. Lock-in amplifier is a tool to extract signals at high modulation frequency, which can eliminate most background in other frequency. In the experimental section, we will discuss this idea briefly. In our work, we not only use high frequency modulation and lock-in detection but also use spectral focusing mechanism and home-made divider circuit to detect SRS signals. The spectral focusing mechanism will be briefly discussed in next section of phase control of laser. Another important feature here is the divider circuit. We already know that the laser fluctuation is main noise source in SRS experiments. Therefore, instead of direct signal measurement, we can measure the ratio of signal and reference, I_{sig}/I_{ref} , as our new signal source. Laser fluctuation should be same for both signals and references, so the ratio of them should be free of laser fluctuation and can increase the sensitivity. In our results, we found that we can improve signal noise ratio more than 10 times although there were still some noise generated from circuit itself. By applying these methods, we developed a simple and convenient technique to obtain fingerprint region SRS spectra for various samples within reasonable acquisition time by a single shot laser, and our detection limit reaches ~mM level.

Different numerical aperture (NA) objectives were also used to verify the relationship between SRS signals and NA, and we found the SRS signals were independent on NA.

2.1.4 Phase control in Coherent Raman process

2.1.4.1 Silberberg's work of phase modulation¹⁹

Quantum control studies how to drive a system from an initial state to a desired state by constructive interference between different paths, and how to avoid the system to evolve into an undesired state by destructive interference between different paths. After the invention of laser, quantum control is one important application for laser technology³³. For CARS, one can think the nonresonant signals are from undesired state, and resonant signals are from desired state. Therefore, quantum control can play an important role to remove nonresonant signals in CARS. Silberberg's group is the first one to employ quantum control in CARS to remove nonresonant signals and even obtain spectacular spectral resolution by using the broadband laser^{19b-d}.

For simplicity in mathematics, we briefly introduce the quantum control idea by two photon absorption, which was also done by Silberberg group³⁴, and then generalize to multiphoton processes including CARS. First, in the two photon absorption process, we need to consider the second order time perturbation theory³⁴.

The amplitude of the excited state can be expressed as^{19e, 34-35}

$$a_f(t) = -\frac{1}{\hbar^2} \sum_n \mu_{fn} \mu_{ng} \int_{-\infty}^t \int_{-\infty}^{t_1} E(t_1) E(t_2) \times \exp(i\omega_{fn} t_1) \exp(i\omega_{ng} t_2) dt_2 dt_1 \quad (2.18)$$

where $E(t)$ is electric field of excitation pulse in time domain, μ_{ij} is transition dipole from state i to state j , ω is the corresponding frequency, and the summation is performed over all possible intermediate states. After several steps of approximation and calculation, the amplitude is proportional to the Fourier transform of electric field square modulation, $a_f(t) \propto \int_{-\infty}^{\infty} E^2(t) \exp(i\omega_0 t) dt$. Therefore, transition probability $p = |a(t)|^2 \propto$

$|\int_{-\infty}^{\infty} E^2(t) \exp(i\omega_0 t) dt|^2$. By using convolution theorem of Fourier transform, and changing variables, we can write^{19e, 35}:

$$\begin{aligned}
p &\propto \left| \int_{-\infty}^{\infty} E^2(t) \exp(i\omega_0 t) dt \right|^2 \\
&= \left| \int_{-\infty}^{\infty} \tilde{E}(\omega) \tilde{E}(\omega_0 - \omega) d\omega \right|^2 \\
&= \left| \int_{-\infty}^{\infty} \tilde{E}(\omega_0/2 + \Omega) \tilde{E}(\omega_0/2 - \Omega) d\Omega \right|^2 \\
&= \left| \int_{-\infty}^{\infty} A(\omega_0/2 + \Omega) A(\omega_0/2 - \Omega) \exp[i\{\Phi(\omega_0/2 + \Omega) + \Phi(\omega_0/2 - \Omega)\}] d\Omega \right|^2 \quad (2.19)
\end{aligned}$$

where $\tilde{E}(\omega) = A(\omega) \exp[i\Phi(\omega)]$ is the Fourier transform of $E(t)$, $A(\omega)$ is amplitude and Φ is the phase in frequency domain. From equation 2.19, we can see that the transition probability of the two photon absorption is the summation of all possible pair of photons with frequency ω_i , ω_j , and $\omega_i + \omega_j = \omega_0$, and all possible photon frequencies lie within the frequencies of excitation laser pulse^{19e, 35}. After applying Fourier transform, we can easily see that phase of pulse plays an important role in controlling the transition probability. Silberberg's group successfully demonstrated that certain two-photon transitions in Cs gas system can switch from allowed transition to forbidden transition by modulating the phase of the excitation pulse³⁴. They call this forbidden pulse as “dark pulse³⁴.”

For CARS, we can follow the similar derivation to show that nonlinear polarization for nonresonant contribution is equal to^{19c}:

$$P_{NR}^{(3)}(\omega) \propto \int_0^{\infty} d\Omega E_{Pr}(\omega - \Omega) \int_0^{\infty} d\omega_1 E_S^*(\omega_1 - \Omega) E_p(\omega_1) \quad (2.20)$$

where P, Pr, S stand for pump, probe and Stokes respectively. For resonant Raman transition polarization,^{19c}

$$P_{NR}^{(3)}(\omega) \propto \int_0^{\infty} \frac{E_{Pr}(\omega - \Omega)}{(\omega_R - \Omega) + i\Gamma} d\omega_1 E_S^*(\omega_1 - \Omega) E_p(\omega_1) \quad (2.21)$$

where Γ is bandwidth. By controlling the phase, which means to consider phase term $\exp[i\Phi(\omega)]$, nonresonant contribution can be suppressed. In addition, the phase modulation methods solve the problem which broadband pulse excitation lacks the

selectivity to excite two neighboring energy levels. Silberberg and coworkers applied the phase modulation methods to probe pulse or both pump and Stokes pulses, and they found that both ways can effectively remove nonresonant signals and obtain great spectral resolution. For example, they shaped probe pulse by adding phase term $\Phi = \tan^{-1}[(\omega - \omega_R)/\Gamma]$. As a result, their spectral resolution was 5 cm^{-1} while they used 120 cm^{-1} bandwidth pulse^{19b-d, 36}.

In our group, we also chose to modulate the phase of probe pulse. Instead of arctan function, we employed π phase in both our group's past work¹⁰ and resonance CARS in this dissertation. In SRS part, we chose quadratic phase (spectral focusing mechanism)¹¹ to shape both pump and Stokes fields. The detailed idea will be presented in the next two sections.

2.1.4.2 Fourier transform spectral interferometry CARS (FTSI-CARS)¹⁰

The theory and methods of Fourier transform spectral interferometry CARS (FTSI-CARS) are well-described in our previous paper¹⁰. In brief, we select pump, Stokes and probe by applying amplitude and phase mask to a broad-band laser pulse. The probe pulse has π -step spectral shape, which does not create vibration excitation but probes the vibration effectively. Generally, vibration signals interfere with nonresonant signal and create controlled spectral interference pattern, from which we obtain the full complex function of vibration spectrum by Fourier transform spectral interferometry.

Figure 2.4(a)-(c) illustrates the basic idea of FTSI¹⁰. Figure 2.4(a) shows the laser pulse after amplitude and phase shaping to generate CARS signals¹⁰. The generated CARS signal $S_\pi(\omega)$ can be expressed as following equation¹⁰ (Figure 2.4(b) top trace).

$$S_\pi(\omega) = |P_{NR}(\omega) + P_R(\omega)|^2 = P_{NR}(\omega)^2 + P_R(\omega)^2 + P_{NR}(\omega)(P_R(\omega) + P_R(\omega)^*) \quad (2.22)$$

P_R is the third order resonant polarization, and P_{NR} is nonresonant polarization. Typically, nonresonant polarization is much larger than resonant one. We can neglect square term of resonant polarization. Therefore, the total signal becomes¹⁰

$$S_\pi(\omega) \approx P_{NR}(\omega)^2 + 2P_{NR}(\omega)\text{Re}[P_R(\omega)] \quad (2.23)$$

Note that the cross-term causes the interference between the nonresonant and resonant signals. We can convert this cross-term to $P_R(\omega)$ by FTSI method. First, normalize the signals ($S_\pi(\omega)$) with the reference signals (S_{ref} , the reference laser is transform-limited Figure 2.4(b) middle trace). Since S_{ref} does not have any sharp spectral features and contains mostly the non-resonant signal. The normalized signal $S_\pi(\omega)/S_{ref}(\omega)$ becomes (Figure 2.4(b) bottom trace)¹⁰

$$S_\pi(\omega)/S_{ref}(\omega) \approx \frac{|P_{NR}(\omega)|^2}{|P_{NR}^0(\omega)|^2} + 2\frac{P_{NR}(\omega)}{|P_{NR}^0(\omega)|^2}\text{Re}[P_R(\omega)] \quad (2.24)$$

where $P_{NR}^0(\omega)$ is the non-resonant signal by the reference excitation laser pulse. The first term ($|P_{NR}(\omega)/P_{NR}^0(\omega)|^2$) becomes a flat offset, while the non-resonant signals in the cross term ($P_{NR}(\omega)/|P_{NR}^0(\omega)|^2$) also has a smooth shape in frequency. As a result, the normalized signals have the spectral shape of ($\text{Re}[P_R(\omega)]$). We can apply the Fourier transform to this real part of resonant signal and then only consider $P_R(t)$ in positive time region¹⁰. Finally, the inverse Fourier transformation of $P_R(t)$ yields the entire complex function of the resonant CARS spectrum in frequency domain $P_R(\omega)$. After $P_R(\omega)$ is retrieved, one can construct Raman-like spectrum by adding imaginary part of $P_R(\omega)$ and amplitude of $P_R(\omega)$ (Figure 2.4(c)). Note that Figure 2.4(b) and (c) is from experimental measured CARS signals of cyclohexane. In our experimental condition, we assume all non-resonant signals are from solvent and their magnitudes are very close to each other.

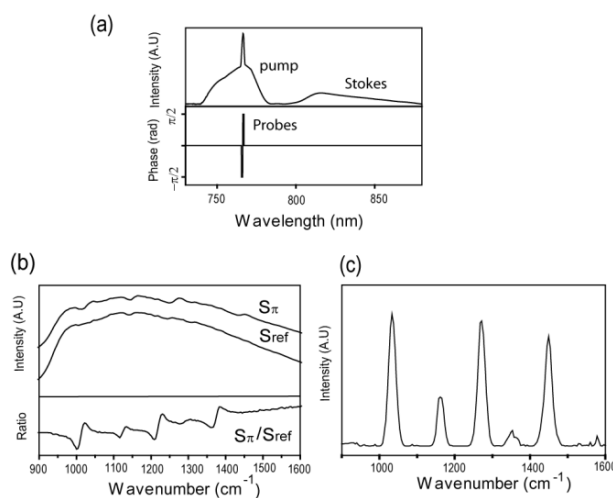


Figure 2.4: (a) The intensity (top) and phase (bottom) of laser pulse versus wavelength used in resonance CARS experiment. (b) Measured CARS signals from cyclohexane. S_π (top) is CARS signal by applying π phase on probe. S_{ref} (middle) is reference signal. Bottom trace is normalized CARS signal S_π/S_{ref} . (c) The Raman-like spectrum of cyclohexane after FTSI procedures¹⁰.

2.1.4.3 Spectral Focusing mechanism¹¹

It is well-known for CARS researchers that the choice of excitation light source is critical to spectral resolution. Although broadband excitation source has advantage on exciting multiple vibrations simultaneously, it also limits the spectral resolution. For typical Raman peaks in fingerprint region, the bandwidth is approximately from 5 to 20 cm^{-1} , and they are much smaller than the bandwidth of usual transform limited femtosecond Gaussian pulse³⁷, which is about 150 cm^{-1} . That's why many researchers used two synchronized picosecond laser as excitation sources for CARS in early stage¹⁷. One way to overcome the spectral resolution problem of broadband laser is to modulate the phase of excitation laser. As we mention in previous section, Silberberg and us used π phase to modulate the laser to obtain CARS spectra in fingerprint region. In spectral focusing mechanism¹¹, the identical quadratic phase (chirp) is added to both pump and

Stokes, so the bandwidth of both pump and Stokes can be stretched to picosecond level, which has better spectral resolution¹¹.

In the following section, two kinds of pictures —time domain and frequency domain—are presented to briefly illustrate the spectral focusing mechanism. For the explanation of time domain picture, which is adapted from our previous publication³⁷, we consider pump field E_p and Stokes field E_s . After both of them combine together, the nonlinear excitation field $A(t)$ can be expressed as $A(t) = E_p(t)E_s(t, \Delta t)^*$, where quadratic phase has been added to pump field $E_p(t)$ and Stokes field $E_s(t, \Delta t)$. Also, assume time difference between pump field and Stokes field is Δt and pump pulse arrives earlier than Stokes field³⁷. If we consider the stationary phase approximation for linear chirped pulse, we can separate electric field to envelope and carrier wave part. In other words, $E_p(t)$ and $E_s(t, \Delta t)$ can be written as³⁷:

$$E_p(t) = E_p(t, \alpha)^0 \exp \left[i \left(\omega_p + \frac{t}{2\alpha} \right) * t \right] \quad (2.25)$$

$$E_s(t, \Delta t) = E_s(t + \Delta t, \alpha)^0 \exp \left[i \left(\omega_s + \frac{t + \Delta t}{2\alpha} \right) * (t + \Delta t) \right] \quad (2.26)$$

where ω_p and ω_s are carrier frequency of pump and Stokes pulse, respectively. α is group velocity dispersion (GVD), which is the coefficient of phase modulation in frequency domain. $E_p(t, \alpha)^0$ and $E_s(t + \Delta t, \alpha)^0$ are envelopes of the electric field³⁷. Basically, the bandwidth of pump and Stokes pulse envelopes depend on GVD α . The more GVD is added, the longer the pulse is stretched. After few steps of algebra, the excitation field $A(t)$ can be expressed as³⁷

$$A(t) = E_p(t, \alpha)^0 E_s(t + \Delta t)^0 * \exp(i\Omega t) * \exp \left[-i \left(\omega_s + \frac{\Delta t}{2\alpha} \right) \Delta t \right] \quad (2.27)$$

where $\Omega \equiv \omega_p - \omega_s - \Delta t/\alpha$. One can see that the frequency of excitation field Ω is also related to time delay Δt and GVD α . Based on these assumption, simple simulations can be performed and the results are shown in Figure 2.5(a) to (d). Both identical stretched

pulses are used for pump and Stokes field, and the results of excitation field $A(t)$ are also shown in Figure 2.5(a) and (b)³⁷. The difference for Figure 2.5 (a) and (b) is only time-delay Δt . According to simulation, one can see that instead of changing the pump and Stokes pulse frequencies, the frequency of excitation field $A(t)$ can be easily adjusted by changing time-delay Δt . We can also investigate the pulse duration effect on $A(t)$ by using shorter pulse. Figure 2.5(c) shows the simulation of using shorter $E_p(t)$ and $E_s(t)$ and resulting $A(t)$ ³⁷. In order to compare the spectral resolution in frequency domain, Fourier transform is performed on $A(t)$ of all three conditions, and the result is shown in Figure 2.5(d)³⁷. One can easily see that Fourier transform of $A(t)$ from shorter pulse in time domain has broader bandwidth in frequency domain. Also, by changing the amount of time-delay Δt , the frequency can be easily tuned³⁷. In real experiments, we control the amount of GVD α by inserting different length of glass and change time delay by moving stage (see experimental section). Thus, we can sweep the desired frequency ranges by adjusting the movement of the stage.

Another way to explain spectral focusing mechanism is from frequency-domain point of view^{11e}. We first consider pump and Stokes pulse with short time profiles, and both of them are transform limited pulses. For the transform-limited pulse, all the frequencies arrive at the same time. Also, because of the short time profile of pump and Stokes pulses, both of them cover broad frequencies. Therefore, after pump and Stokes pulses interact together, the bandwidth ($\Delta\Omega$) of vibrational excitation field also has broad bandwidth at short time duration, which illustrate in the left panel of Figure 2.6(a)^{11e}. Then we assume time delay Δt is zero. If both pump and Stokes pulses have been stretched, it means different frequencies arrives at different time, and total time duration is longer than the transform-limited pulse. In the right panel of Figure 2.6(a)^{11e}, identical linear chirp (quadratic phase, GVD) is added to both pump and Stokes. The central

frequency (Ω) of vibrational excitation field is same due to identical chirp of both pump and Stokes. Also, the bandwidth is narrower than the field excited by the transform limited pulses. When time delay Δt is not zero, it means different pump and Stokes frequencies interact at different time (Figure 2.6(b)). Therefore, various frequencies (e.g. Ω_1, Ω_2) can be easily modulated by different time delay. Furthermore, the bandwidth of vibrational excitation field is narrower than transform limited pulses.

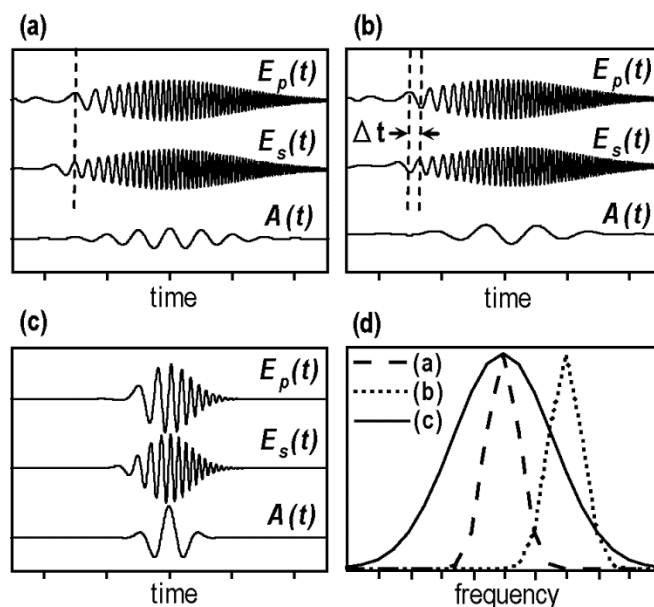


Figure 2.5: Spectral focusing mechanism in time-domain. (a and b) Temporal profiles of pump, Stokes and excitation field. For (a), time delay is zero. For (b), time delay is Δt . (c) is the field with shorter pulse duration. (d) Fourier transform for all excitation field from (a)-(c). The figure is a copy from our group's previous publication³⁷

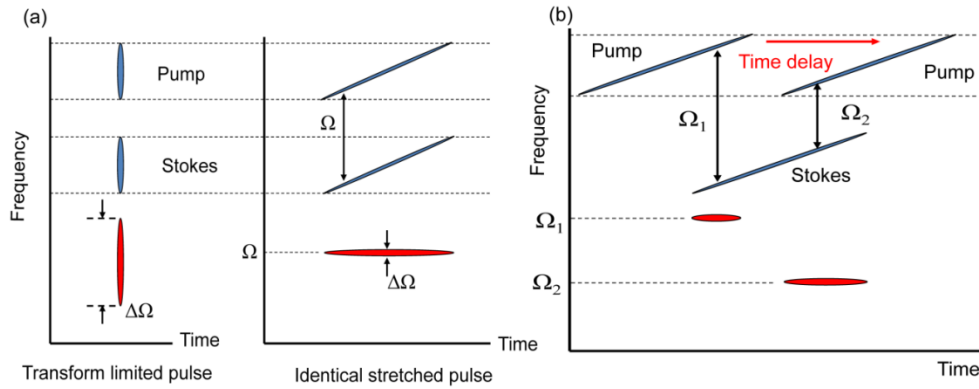


Figure 2.6: Spectral focusing mechanism in frequency-domain. (a) The comparison between transform-limited and stretched pulse when time delay is zero. (b) The stretched pulse can modulate different frequency by adjusting time delay Δt ^{11e}.

2.2 EXPERIMENTAL SECTION

2.2.1 Resonant CARS

Figure 2.7 shows the experimental setup. CARS signals were generated with a cavity-dumping Ti-Sapphire oscillator (Cascade, KM Lasers), whose repetition rate was 2MHz. We used a 640 pixel dual bank liquid crystal spatial light modulator (SLM-640-D-VN, CRI) to manipulate the amplitude and phase of the laser pulse. The spectral resolution of pulse shaper was 0.4 nm, which corresponded to 5.3 cm^{-1} at 800 nm. The wavelength of the laser shorter than 740 nm was blocked by a razor blade placed just before the SLM. The shaped pulse was focused into the sample and the signals were collected with high NA water immersion objectives (1.2 and 1.0 NA, respectively, Olympus). Note that the pump power was 2.0 mW, the Stokes power was 1.0 mW, and the probe power was 0.3 mW. The collected signals were filtered by short wave pass filter (740 AESP, Omega Optical), coupled into an imaging spectrometer (Holospec f/1.8,

Kaiser Optical Systems) and measured with a frame transfer charged-coupled device (CCD) (DV887, Andor).

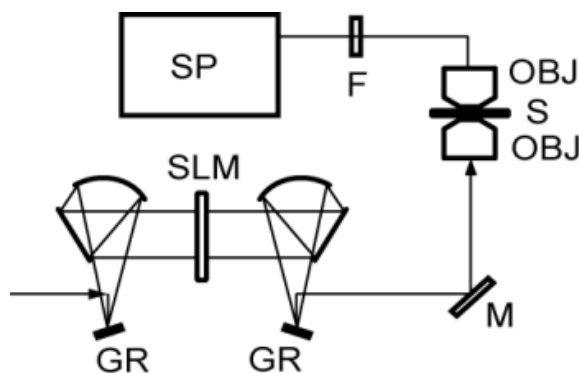


Figure 2.7: Experimental setup of resonance CARS: GR, grating; SLM, spatial light modulator; OBJ, microscope objective; S, sample; F, short wave pass filter; SP, spectrometer¹⁰.

The dyes (1,1'-Diethyl-2,2'-carbocyanine Iodine, DCI'; 3,3'-Diethyloxadicarbocyanine Iodine, DODCI; and Rhodamine 800, R800) were purchased from Exciton and used as received without further purification. The spectral grade methanol (MeOH) (Fisher Scientific) was used as solvent. The absorption spectra were recorded by UV-Vis spectrometer (HP 8453), and the concentrations of different dyes were calibrated by known absorption coefficients. FTSI-CARS measurements were performed with one drop of dye solutions sandwiched between two microscope coverslips. The thin 20 μm plastic film was used as spacer between two glasses to prevent the signals absorbed by the sample.

2.2.2 SRS

The optical setup of SRS was adapted from our group's previous work of spectral focusing CARS³⁷ and shown in Figure 2.8. In brief, we used broad-band pulses from a single cavity dumping Ti:sapphire oscillator laser (Cascade, KM Lasers) as our excitation

source. The repetition rate of each pulse was 2 MHz, and the laser spectrum was drawn in Figure 2.9 upper panel. The output energy was 40-45 nJ in 2 MHz. Basically, the laser beam first passed through a 10 cm SF57 glass rod (Casix) to stretch the whole pulse. Next, the laser beam was separated into two parts by passing through 810 long wavelength pass filter (Omega Optical). The short wavelength part served as pump, and the long wavelength part served as Stokes. The pump part was directed into a Pockels cell (ConOptics, model 350-50C) to switch the polarization direction of incoming pump pulses. The polarization beam splitter and mirror assisted to choose a desired polarization. We performed 100 kHz polarization modulation to produce fast modulated on-off states, so we can detect weak signal changes by lock-in amplifier. The principle of SRS signals detection will be discussed in next section. For Stokes part, we stretched Stokes pulse more by inserting pieces of SF57 glass rods (Casix) to the Stokes light path. The amount of GVDs of both pump and Stokes were matched according to spectral focusing mechanism. The pulse was stretched to 1.5 ps. The corresponding phase and wavelength relationship was shown in the bottom panel of Figure 2.9. To obtain the SRS spectra in the fingerprint region, a proper time delay was required. The required time delay can be adjusted by moving computer-controlled translation stage (M.405-CG, PI) on Stokes light path. The pump and Stokes were recombined with the assistance of 790 short wavelength filter (Omega Optical). The recombined pulse was directed into different NA objectives (NA=0.1 4x, NA=0.25 10x, NA=0.4 20x, Olympus) to focus on the sample. The signals were collected by a photodiode (Thorlabs, DET 100A), and the reference was collected from the Stokes by the same type of photodiode as well. The signals and reference were guided into a homemade divider circuit, and the homemade divider circuit converts photocurrents into voltage first and then amplified it. The processed overall signals were sent into lock-in amplifier to extract the SRS signals. The

divider can increase roughly 10 times sensitivity. We chose different time constant (10 ms, 30 ms, 100 ms and 300 ms) of lock-in amplifier to find appropriate experimental conditions and detection sensitivities for each sample. We chose the duration time for each point was three times to the time constant of lock-in amplifier.

All chemicals were purchased from Fisher Scientific including toluene, methanol, ethanol, sodium nitrate, urea and phenylalanine. The chemicals were all used as received without any further purification.

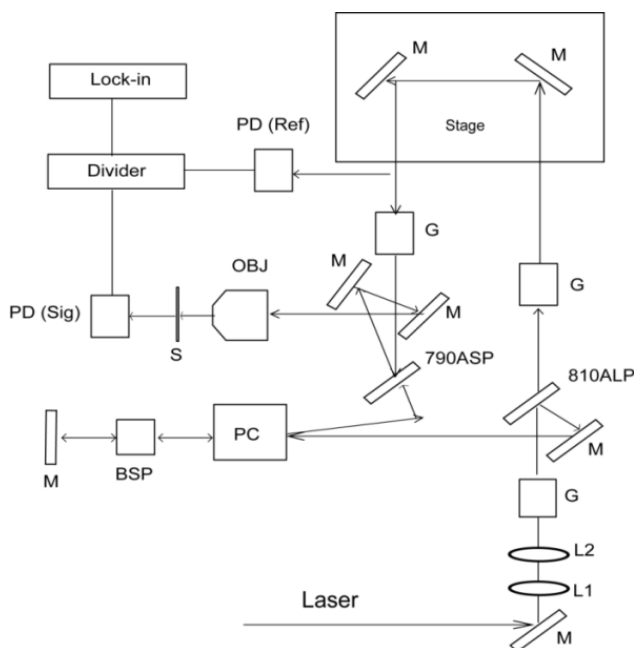


Figure 2.8: Optical setup of SRS. The arrow means the laser direction. M: mirror, L: lens, G: SF57 glass rod, 810ALP: 810 nm long wavelength pass filter, 790ASP: 790 nm short wavelength pass filter, PC: pockel cell, BSP: polarizing beam splitter, PD: photodiode, OBJ: objective, and S: sample.

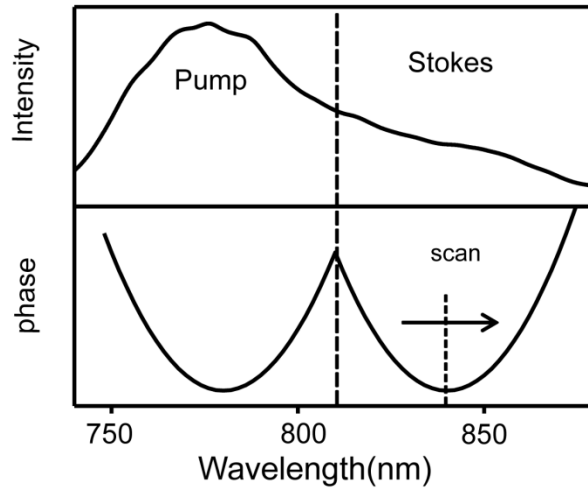


Figure 2.9: Laser spectrum for SRS experiment (upper panel) and corresponding phase of different wavelengths (bottom panel). Note that pump and Stokes are separate at 810 nm and the corresponding phase is quadratic.

2.2.2.1 Principles of high frequency modulation, lock-in amplifier and divider circuit

Similar to other groups, we used high frequency modulation technique and lock-in amplifier for SRS signal detection^{27, 29a, 32}. The basic principle of frequency modulation in SRS detection is shown in Figure 2.10^{25b, 29a}. The pump pulse (a) is modulated between on and off states in high frequency (b). After modulated pump pulse (c) interacts with original Stokes pulse (d) and the sample, either stimulated Raman loss (SRL) (e) or stimulated Raman gain (SRG) (f) can be detected^{25b, 29a}. To minimize laser noise, high frequency modulation is needed. Typically, laser has higher noise in low frequency region (DC to kilohertz) than high frequency region. Empirically, laser noise is related to $1/f$, the so-called $1/f$ noise^{25b}. The fast modulation of laser (\sim MHz) removes low frequency laser noise and the system can approach shot-noise limit^{25b}. The sensitivity can be increased several orders due to approaching shot noise limit^{25b, 29}.

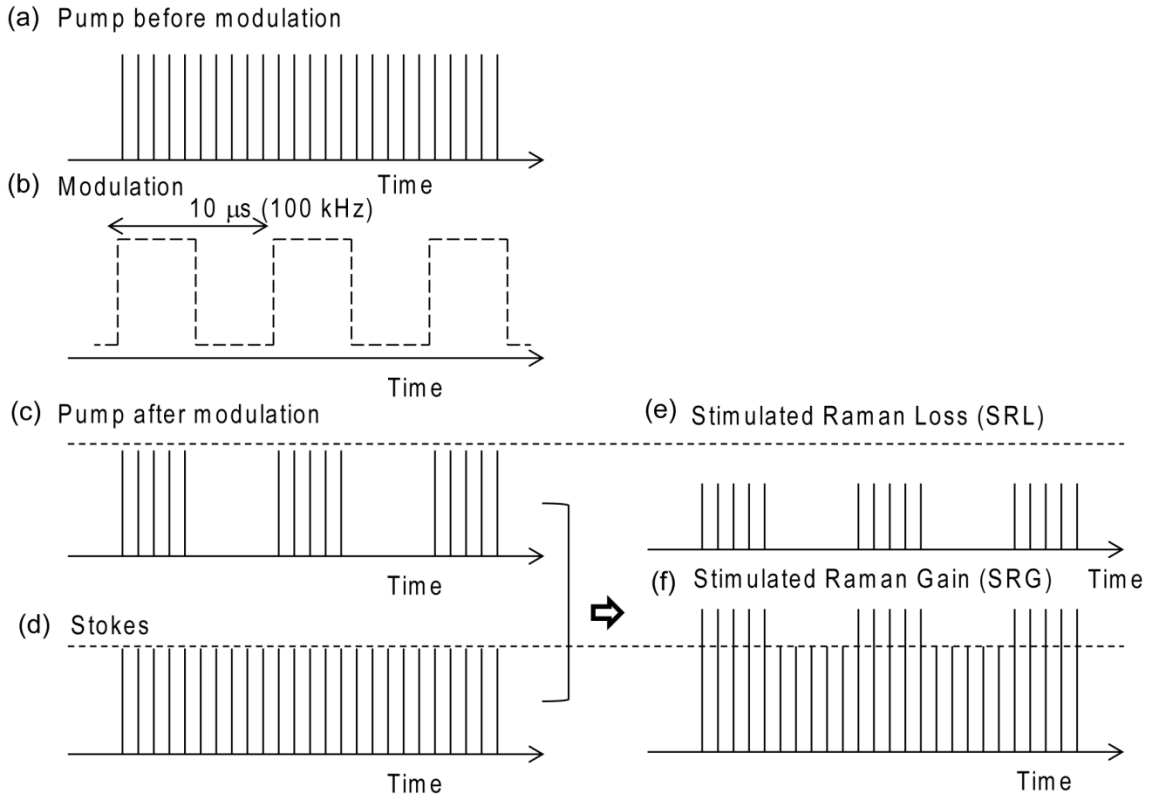


Figure 2.10: The scheme of frequency modulation for SRS signal detection. (a) Pump pulse before modulation, (b) Frequency modulation by fast changing on-off state, note that the modulation frequency is 100 kHz in our experiment. (c) Pump pulse after modulation, (d) Stokes without any modulation, note that pump and Stokes initially come from the same laser source in our experiment. After interaction among modulated pump, non-modulated Stokes and the sample, (e) and (f) show SRL and SRG respectively. The figure is adapted from reference 25b and 29a^{25b, 29a}

Another important element to detect SRS signals is lock-in amplifier. Here, we briefly discuss the principle of lock-in amplifier. The detailed explanation can be found in many literatures and technical notes³⁸. Consider very small signals (for example, SRS signals) in huge noise (for example, laser noise), and we need to detect it. Although a good low-noise amplifier with a band pass filter helps a little, the signal-to-noise ratio is still not satisfied enough. Therefore, we need a better solution to detect the weak signal.

Lock-in amplifiers and high frequency modulation are solution. To briefly discuss the principle of lock-in amplifiers, we assume our signals are sinusoidal, and we can express our signals as³⁸ $V_{sig} = V_0 \sin(\omega t + \theta)$, where ω is signal frequency, θ is signal phase and V_0 is signal amplitude, which is also the value we want. Sometimes the signal is sent into amplifier with filters to have preliminary process of the signal. On the other hand, lock-in amplifier has internal reference signal $V_r = V_1 \sin(\omega_r + \theta_r)$, where subscript r represents reference³⁸. Next, both signals and reference are sent to a phase-sensitive detector (PSD), which is the heart of lock-in amplifier. The PSD multiplies both signals and reference, and the output becomes the product of both signals and reference. The output can be expressed as³⁸

$$\begin{aligned} V_{out} &= V_0 \sin(\omega t + \theta) \times V_1 \sin(\omega_r + \theta_r) \\ &= \frac{1}{2} V_0 V_1 \cos[(\omega - \omega_r)t + (\theta - \vartheta_r)] - \frac{1}{2} V_0 V_1 \cos[(\omega + \omega_r)t + (\theta + \vartheta_r)] \quad (2.28) \end{aligned}$$

After PSD, the output signals become two terms, difference frequency and sum frequency³⁸. If two frequencies are identical, the first term becomes DC signals, and second term is second harmonic of original frequency. The processed signals are then sent to frequency filter to remove high frequency component. The filtered signals will be $\frac{1}{2} V_0 V_1 \cos(\theta - \vartheta_r)$. Now one can really tell the importance of phase difference term $(\theta - \vartheta_r)$. If phase difference changes with time, filtered signals also change with time. Therefore, the phase difference needs to maintain constant to obtain DC signals³⁸. In other words, phase difference needs to be locked. That's why we call it "lock-in amplifier." Locked phase is the key of lock-in amplifier. The final DC signals are proportional to V_0 , the quantity we want to measure. In Scofield's paper, he also provided a frequency domain analysis³⁸. One can easily see how lock-in amplifier retrieved small signals from noise by the process described above.

The home-made voltage divider is also important feature for us to increase the sensitivity³⁹. The divider circuit removes the laser fluctuation by taking the ratio of signal and reference, which should be independent of laser noise. In brief, we first convert the photocurrent generated from signal and reference photodiodes to voltages with transimpedance amplifier based on operational amplifier (LF155). Then we feed these two voltage signals into AD734 (analog device, inc) voltage divider. The output of this divider is $\Delta V_{sig}/V_{ref}$ in V unit. We can adjust our circuit; therefore, if 1mV is shown in lock-in amplifier, it directly tells us that $\Delta I_{Stokes}/I_{Stokes}$ is 10^{-3} .

2.3 RESULTS AND DISCUSSION

2.3.1 Resonance CARS

Figure 2.11(a) shows the FTSI-CARS spectra of pure methanol and all three dyes dissolved in methanol at the same concentration (1 mM). The first thing we noticed was the intensity of MeOH peaks of all dyes was similar to each other. But the peak intensity of dyes was different from each other. For R800, the strongest peak (1480 cm^{-1}) has similar intensity with its methanol peak. In the other words, the signal level of R800 (1 mM) was almost the same as pure MeOH (25 M). We can estimate that the enhancement is about 10^4 times with the assistance of resonance effect. Under the tightly focus condition, our focal volume was about 10^{-16} liter, which meant the number of R800 molecules we detected was about 6×10^4 , and the number of methanol molecules was about 1.5×10^5 . Based on the same argument, we can see the resonance enhancement with all three dye molecules, and the enhancement factors of all three dyes were quite different. The enhancement factor depended on the spectral overlap among laser, CARS and absorption peaks of dyes. Quantitatively, we can describe this enhancement effect by

time-dependent perturbation theory. According to time-dependent perturbation theory, the signal intensity of CARS signal can be expressed as equation below⁴⁰.

$$I_{CARS} \propto \left| N \sum_{k,m,l,n} \frac{\mu_{km}\mu_{ml}\mu_{ln}\mu_{nk}}{(\omega_{mk} - \omega_p - i\gamma_{mk})(\omega_{lk} - \omega_p + \omega_s - i\gamma_{lk})(\omega_{nk} - \omega_{as} - i\gamma_{nk})} \right|^2 \quad (2.29)$$

where N is number of molecules, μ_{xy} is the transition dipole moment between intermediate states x and y, ω_{xy} is the energy (frequency) difference between x and y state, γ_{xy} is the homogeneous linewidth of the associated (electronic or vibrational) transition between x and y. If the laser frequency and generated signals can match the transition frequency of each step, the denominator terms in equation above become very small, and the overall CARS signal can be enhanced greatly. However, we only considered signals enhanced by single resonance (i.e. $\omega_{nk} \sim \omega_{as}$) here instead of triple resonances (i.e. $\omega_{mk} \sim \omega_p$, $\omega_{lk} \sim \omega_p - \omega_s$, $\omega_{nk} \sim \omega_{as}$). Figure 2.11(b) shows the normalized absorption spectra of DODCI, DCI' and R800 dissolved in methanol, laser spectrum after pulse shaping and the generated CARS signal position. The absorption maximum of DODCI, DCI' and R800 were 579nm, 654nm and 679nm respectively. Among all three dyes, R800 had the most spectral overlap between absorption and CARS signals, which was consistent with the results we just discussed. We expected the CARS signals can be increase several orders of magnitudes by triple resonances, which is already demonstrated by Xie group⁴⁰. Another important point which should be pointed out here was that we did not see the significant change of non-resonant signals in different dyes of various concentrations. We thought the possible reason is because the nonresonant signals for dyes which concentration are less than 1 mM are mainly from MeOH, and nonresonant signals are not electronic resonant with laser pulse.

We further investigated our detection limit for all of dyes and the relation between signals and concentration. Figure 2.12(a) shows that the FTSI-CARS spectra of both dyes

under relatively low concentration (R800 is about 30 μM , and DCI' is about 60 μM). Compared to methanol spectrum, we can still clearly see signals from both R800 and DCI' under such low concentration. According to our experimental results, the detection limits of both dyes were 16 μM for R800 and 31 μM for DCI'. For DODCI, the detection limit was about 125 μM , several times higher than R800 and DCI'. In Figure 2.12(b), we plotted the intensity of R800 1342 cm^{-1} peak versus concentration. Note that we calibrated the signals with its 1040 cm^{-1} peak of MeOH as an internal reference. Instead of quadratic dependence, the plot showed good linear dependence between concentration and intensity. Remember that in FTSI process, we assumed P_{NR} was mainly from solvent and much larger than P_{R} , so FTSI-CARS signals were proportional to the cross term $P_{\text{NR}} \times \text{Re}[P_{\text{R}}]$ which was linear dependence of concentration.

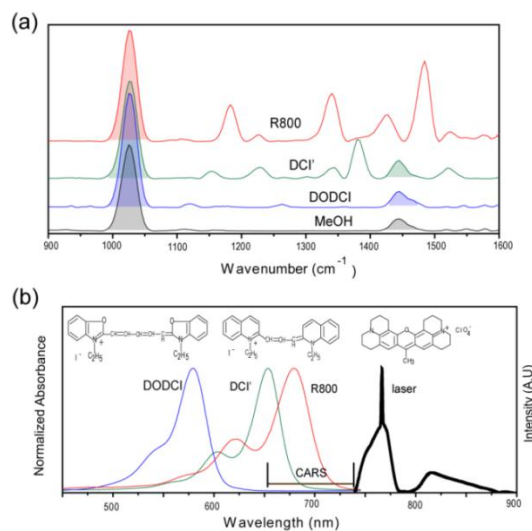


Figure 2.11: (a) FTSI-CARS spectra of 1mM dyes in methanol and pure methanol (MeOH) (From top trace to bottom: R800, DCI', DODCI and MeOH). The shadow indicates the corresponding solvent peak. (b) The normalized absorption spectra of DODCI, DCI', and R800, dissolved in methanol, their molecular structures, and the experimental laser pulse spectrum after pulse shaping. Note that the CARS signal ranges produced by pulse shaping laser also labels on the figure.

So far we only considered the case which dyes dissolved in methanol. We also attempted to dissolve our dyes in water to see the signal enhancement. The solubility of all three dyes is low in water, so we can only compare the medium concentration (125 μM) in MeOH and water. Surprisingly, for DCI in water, although the concentration and laser conditions were same, the signals almost disappeared. Similarly, the signals of R800 decreased few times in water. Remember that all variables were same in equation above except the homogeneous line width γ_{nm} . We know that $\gamma_{nm} = (\gamma_m + \gamma_n) / 2 + \gamma_{nm}$, γ_n is the inverse lifetime ($1/T_1$) of state n and γ_{nm} is pure dephasing rate for the coherence rate m and n¹⁶. For DCI, the reported fluorescence lifetime in MeOH was about 10 ps⁴¹, but for R800, the reported fluorescence lifetime was about ~ns both in methanol and water⁴². We can assume that all of CARS processes were finished within 1-2 ps because of using fs pulse laser. Therefore, the fluorescence lifetime didn't make any difference. Therefore, we had to consider the solvent effect to explain the intensity difference between methanol and water. The different solvent might change the pure dephasing rate or induce the inhomogeneous line broadening effect. Also, R800 were reported to aggregate in the solvent under the high concentration⁴². Aggregation was another issue we need to consider for dyes in different solvents. Until now, we still did not have enough information to make a judgment.

In summary, the amplitude and phase of laser pulse were optimized to generate CARS signals which were resonant with chosen dyes. The amount of resonant effect can be verified by choosing dyes with different molecular electronic transitions. The high numerical aperture objectives were also used to obtain a tightly focus condition. To overcome the problem of nonresonant background, we used FTSI technique to extract the resonant signal from nonresonant background to obtain Raman-like spectra. Because FTSI technique used the linear dependent cross term to determine the signals, the linear

concentration dependence is expected instead of quadratic dependence. The combination of pulse shaping, electronic resonant effect, FTSI, and high-resolution microscopy can push our detection limit to $\sim 10 \mu\text{M}$ which corresponds to about 1200 molecules under tightly focus condition.

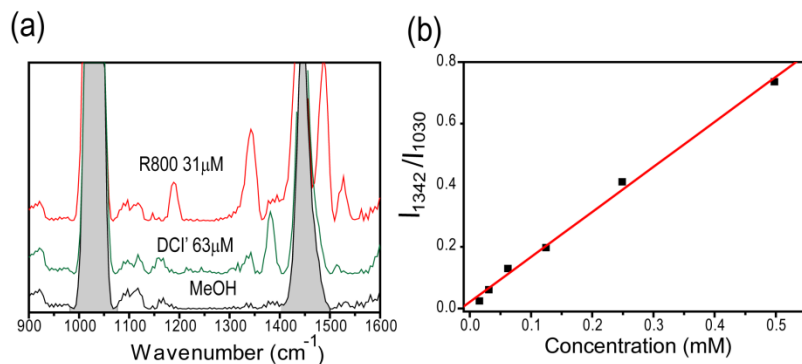


Figure 2.12: (a) The FTSI-CARS spectra of R800 and DCI' under low concentration (R800, 31 μM ; DCI', 63 μM in methanol) and compare to pure methanol. The shaded area is corresponding solvent peak. (b) Plot of intensity at 1342 cm^{-1} calibrated by methanol 1030 cm^{-1} peak intensity versus R800 concentration and its best least-squares fitting.

2.3.2 SRS

After we built our spectral focusing SRS setup, we have to examine the feasibility with solvents of well-characterized Raman features. With the assistance of broadband laser and spectral focusing mechanism, we were able to obtain SRS spectra of different samples within 800-1600 cm^{-1} (fingerprint region) by a single shot laser. We first chose pure toluene as the test sample. The toluene Raman spectrum is shown in Figure 2.13a. The time constant of lock-in amplifier we used in Figure 2.13a was 3 ms, which corresponded to 13.5 seconds acquisition time. The spectrum clearly showed Raman-like features, free of background, and no spectral distortion. One can clearly see the splitting

around 1000 cm^{-1} and 1200 cm^{-1} . The peak position and the splitting were matched with Raman in the literature⁴³. It confirmed the feasibility and demonstrated great spectral resolution of our femtosecond spectral focusing SRS setup. The resemblance between our SRS toluene spectrum and Raman spectrum also confirmed the SRS theory we discussed in the section 2.1.3. Figure 2.13b shows SRS of other samples including 1M urea aqueous solution⁴⁴, 1M sodium nitrate⁴⁵, pure ethanol⁴³ and pure methanol⁴³ (from top trace to bottom trace) under 45 seconds acquisition time. All spectra were consistent with Raman spectra in the literatures.

Next, we can estimate the ratio of experimental noise and shot noise limit in our system. In other words, we wanted to compare the detection limit of our system to the theoretical limit. In our system, we used photodiode to detect the signals, so the numbers of generated photoelectrons determined the shot noise limit. We can roughly estimate the number of photoelectrons generated in reference photodiode as following: First, we measured the photocurrent of Stokes laser by chopping the Stokes beam without pump beam by lock-in amplifier. It was 20 mV with 50 ohm load, so the photocurrent from Stokes was apparently 0.4mA. We multiplied current I with time constant τ under different conditions and divided by 1.6×10^{-19} to obtain the numbers of photoelectrons. Finally, we took square root of photoelectrons as shot noise limit. The estimated noise results were summarized in Table 2.1. The shot noise limit in our system was approximately 10^{-7} at various time constants. We also estimated experimental fluctuation as 10^{-6} . Therefore, approximate one order of magnitude difference needed to be improved to achieve shot noise limit. We believed the noise from divider circuits and laser noise contributed one order of magnitude deviation from shot noise limit. This can be caused by many factors such as the inner structure of our photodiode, collection objective, filter loss, and circuit noise.

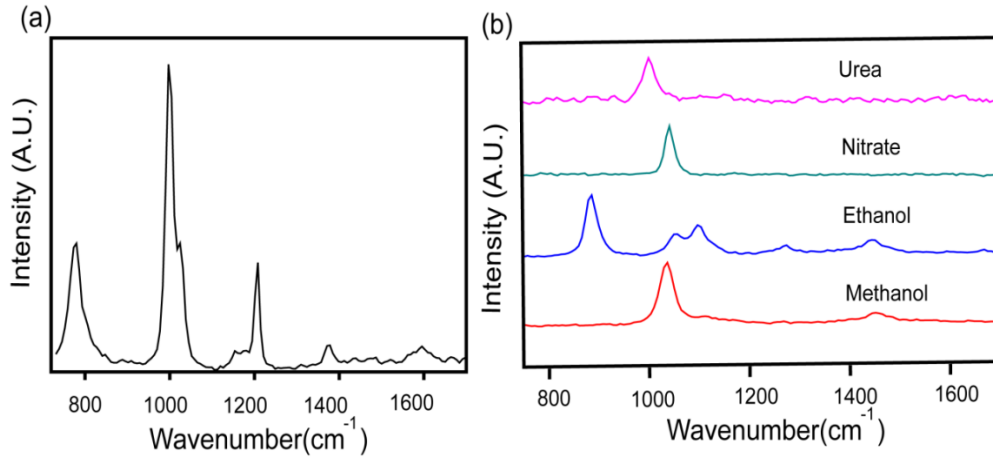


Figure 2.13: The SRS spectra of different compounds. (a) Pure toluene solution (b) From top trace to bottom are: 1M urea aqueous solution, 1M sodium nitrate aqueous solution, pure ethanol, and pure methanol solution. Acquisition time for (a) is 13.5 s and (b) is 45 s.

	3 ms TC¹	10 ms TC	30 ms TC	100 ms TC
current (A)	4×10^{-4}	4×10^{-4}	4×10^{-4}	4×10^{-4}
numbers of photoelectrons	7.5×10^{12}	2.5×10^{13}	7.5×10^{13}	2.5×10^{14}
shot noise limit (SNL)²	7.3×10^{-7}	4.0×10^{-7}	2.3×10^{-7}	1.3×10^{-7}
exp noise	2.0×10^{-5}	1.0×10^{-5}	5.0×10^{-6}	2.0×10^{-6}
exp noise / SNL	2.7×10^1	2.5×10^1	2.2×10^1	1.6×10^1

¹ TC: time constant ² SNL was estimated by two times of square root of number of photoelectrons

Table 2.1: Estimation of numbers of photoelectrons, shot noise limit, experimental noise and ratio of both noises under different conditions

Next, we sought the detection limit of our system after we verified the feasibility of our system. We chose sodium nitrate solution and phenylalanine (PA) solution to study the detection limit. The former is the common inorganic salt with one strong Raman

peak⁴⁵ at 1044 cm^{-1} , and the latter is an important amino acid in biology with three well-characterized Raman peak⁴⁶, 1004 cm^{-1} , 1032 cm^{-1} and 1208 cm^{-1} . In both Figure 2.14(a) and (b), we performed all the SRS experiments under 30 ms time constant of lock-in amplifier (total acquisition time is 135 seconds). In Figure 2.14(a), we began with 500 mM sodium nitrate and then diluted it until 50 mM. One can easily see that the detection limit was about 50 mM for sodium nitrate. In Figure 2.14(b) and (c), we also examined sensitivity and concentration dependence for PA. Because of low solubility of PA, we began our experiments with 180 mM aqueous solution. Similar to toluene, we also saw the spectra splitting around 1000 cm^{-1} in the 180 mM sample, and the peak positions were 1010 cm^{-1} and 1037 cm^{-1} , about 5 cm^{-1} difference from the literature⁴⁶. Again, the splitting confirmed the spectral resolution of our SRS system was approximately 20 cm^{-1} . After several dilutions, we were still able to see 1010 cm^{-1} peak with 45 mM sample. For 22 mM sample, the sample almost reached the limit of our system, and the intensity of peak signal was very close to the intensity of noise. Therefore, we can conclude that our detection limit was about 10 mM level under 135 seconds acquisition. We also plotted the relation between concentration and SRS intensity of PA in Figure 2.14(c). Good linear dependence can be observed in Figure 2.14(c), and it further confirmed SRS detection mechanism we discussed in section 2.1.3.

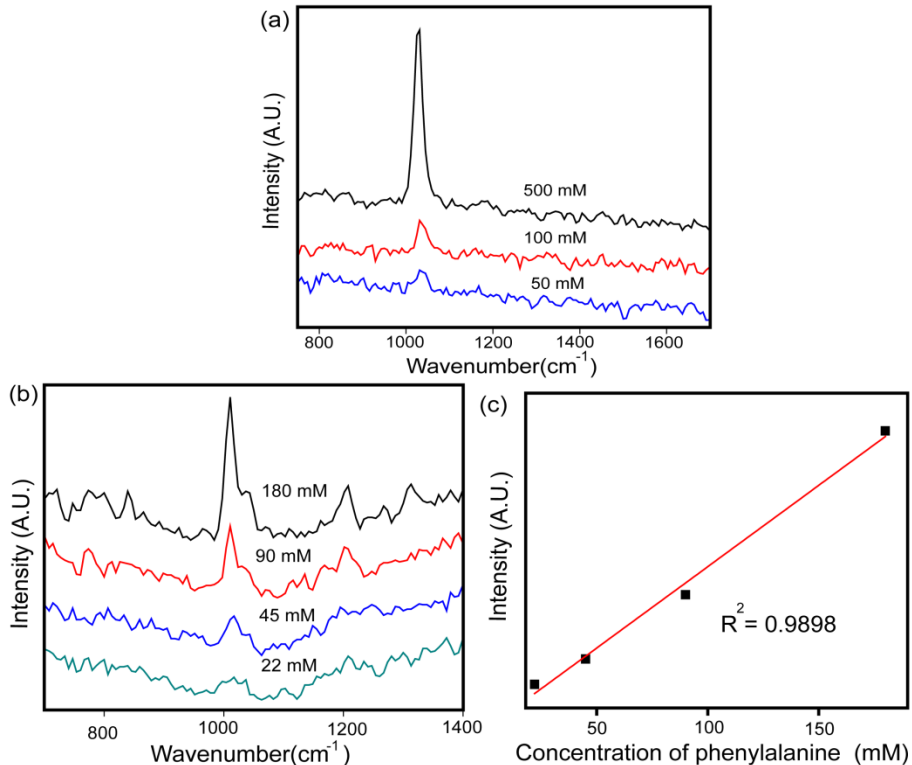


Figure 2.14: The SRS spectra of (a) sodium nitrate (b) phenylalanine with different concentrations. The time constant of lock-in amplifier was 30 ms (total acquisition time was 135 s) for both (a) and (b). (c) is the plot of concentration of phenylalanine versus SRS intensity and linear fitting at 1010 cm⁻¹ peak.

We also attempted to change the experimental conditions including longer acquisition time and more averages to see if we can push the detection limit of our system. Figure 2.15(a) shows different conditions for 50 mM sodium nitrate. Originally, our detection limit was 50 mM for sodium nitrate with 30 ms time constant (135 second acquisition time) and one spectral average (top trace in Figure 2.15(a)). Compared to 30 ms situation, one can see larger time constant (longer acquisition time) made the noise fluctuation become smaller (middle trace). In addition, by comparing middle and bottom trace of Figure 2.15 (a), one can see more spectral averages also decreased the fluctuation

of spectra. Figure 2.15(b) shows different conditions for 22 mM PA. Noise also decreased by longer acquisition time. However, although noise can be decrease by change of experimental conditions, long experimental time was the price needed to be traded off. For example, 300 ms time constant and one spectral average took about 20 minutes to obtain a spectrum. Therefore, one has to choose the optimum conditions to match with experimental requirements.

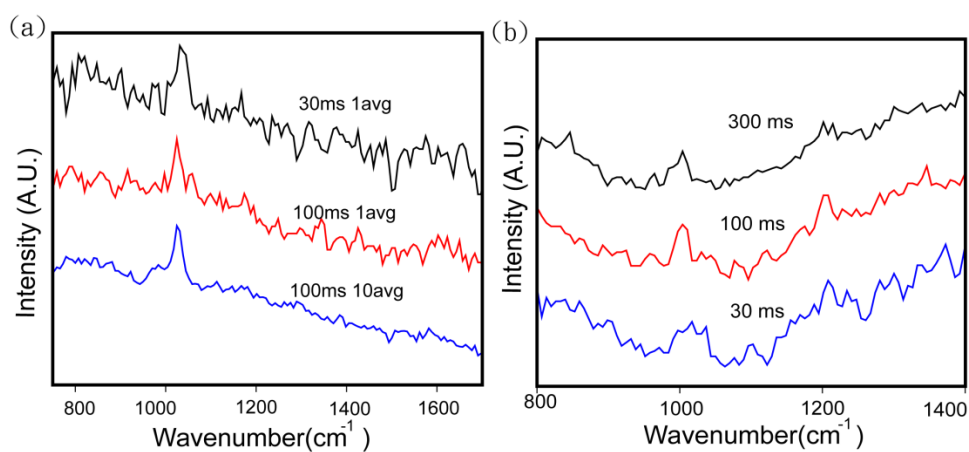


Figure 2.15: Different experimental conditions for (a) 50 mM sodium nitrate solution. From top trace to bottom: 30 ms time constant, 1 average; 100 ms, 1 average; 100 ms and 10 average (b) 22 mM phenylalanine, from top trace to bottom trace: 300 ms, 100 ms and 30 ms time constant, all are with 1 average.

In the last part of SRS, we investigated the relation between SRS signals and numerical apertures (NA)⁴⁷. For SRS, the signal in our system is a ratio $\Delta I_{Stokes}/I_{Stokes}$ and this ratio depends on pump fluence (energy per area) and sample concentration linearly. Integrating the signal (ratio) over the entire sample volume leads to no dependence of NA because signals are integration of fluence (power per unit area) multiply action area and multiply concentration over the optical axis, and fluence

multiply action area equal to power irrespective of area. Therefore, the signal does not depend on NA. Figure 2.16 shows SRS signals of toluene by using different objectives and the NAs are 0.4, 0.25, and 0.1 respectively from top panel to bottom. One can see the spectra among three different conditions were almost same, and it verified our assumption.

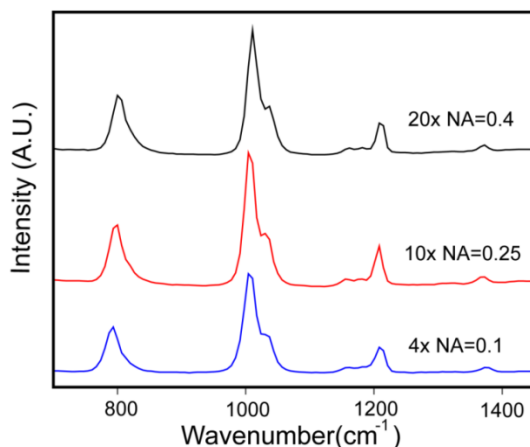


Figure 2.16: SRS of toluene spectra for different objectives. Three spectra are taken at same condition. The y axis scales are same for all three SRS spectra.

2.4 CONCLUSION

In coherent Raman project, we successfully investigated the resonance effect of different dyes for CARS and demonstrated the feasibility of spectral focusing mechanism for SRS. We found that the detection sensitivity can be enhanced several orders of magnitude due to the molecular resonant effect, and our results showed the detection limit was 10 μM for the most resonance-assisted dye for CARS. For SRS, we quantitatively characterized the performance of spectral focusing SRS system for spectroscopy purpose. It led us to conclude that we needed much higher pump pulse energy to make SRS useful in biology imaging purpose. Regenerative amplifier typically

has pulse energy more than 1mW in 1 kHz. With the amplified laser pulse, the SRS signals can be enhanced more than 10^4 because our pump power is 10 nJ, which is 20 mW in 2MHz, and 100 uJ, 100 mW in 1 kHz, will give us 10^4 signal enhancements.

Chapter 3 Surface Enhanced Raman Scattering

3.1 INTRODUCTION

As stated in chapter 1, surface enhanced Raman scattering (SERS) is another way to enhance Raman signals enormously, and this effect has been known for 30 years⁴⁸. In 1997, it was also demonstrated that SERS effect can enhance Raman signals even up to the single molecule level⁴⁹. Since the discovery of single molecule SERS, there have been intense research efforts aiming at understanding the SERS mechanism⁵⁰. In the early stage of SERS research, it was found that the aggregate noble metal nanoparticles are the key requirements of single molecule SERS measurements. As the nano-fabrication techniques are improved, researcher can study SERS phenomena of nano- structures of well-controlled shapes. Nowadays, most researchers have consensus of SERS mechanism, and it's closely related to the optical properties of noble metal nanoparticles⁴⁹⁻⁵⁰. Hence, before introducing the current accepted SERS mechanism, it is necessary to understand the optical properties of noble metal nanoparticles.

3.1.1 Introduction to localized surface plasmon resonance (LSPR)^{6, 9, 12, 51}

To understand the optical properties of noble metal nanoparticles, we first have to know the behavior of the conduction electrons of metal particles when the metal particles are excited by electromagnetic field (light). We first assume the conduction electrons of metal particles behave like free electrons, and conduction electrons can be treated as classical harmonic oscillator without considering restoring force^{12, 51c, d}.

Therefore, similar to the discussion in SRS section (Section 2.1.3), we can write the equation for free electron model as 1-D harmonic oscillator model^{12, 51c, d}:

$$\frac{d^2x}{dt^2} + \gamma \frac{dx}{dt} = -\frac{eE(t)}{m} \quad (3.1)$$

where t is time, γ is damping constant, e represents charge of an electron, m is mass of an electron, and $E(t)$ is electric field. Note that two things are different from previous discussion in section 2.1.3. First, because of the properties of free electrons, we do not have to consider restoring force here. In other words, we neglect the x term in harmonic oscillator equation. The other is that the force term is just simple interaction between electron and applied electric field. We just assume the electric field is simple harmonics $E(t) = E_0 e^{-i\omega t}$, and we can use $x(t) = x_0 e^{-i\omega t}$ as the trial solution to solve the equation. After plugging the trial solution into equation, we obtain^{12, 51d}

$$x(t) = \frac{eE(t)}{m} \frac{1}{\omega^2 + i\gamma\omega} \quad (3.2)$$

We also know that the macroscopic polarization $P = -nex$, so^{12, 51d}

$$P = -nex = -\frac{ne^2 E(t)}{m} \frac{1}{\omega^2 + i\gamma\omega} \quad (3.3)$$

In electrodynamics, dielectric displacement D is commonly used in Maxwell equation^{12, 51d, 52}

$$D = \varepsilon_0 E + P = \varepsilon_0 \varepsilon E \quad (3.4)$$

where ε is dielectric constant. We can plug Equation 3.3 into 3.4, and obtain^{12, 51d}

$$\varepsilon(\omega) = 1 - \frac{\omega_p^2}{\omega^2 + i\gamma\omega} \quad (3.5)$$

where $\omega_p^2 = (ne^2/m\varepsilon_0)$, which is plasma frequency. This is the famous Drude model of free electron gas^{12, 51c, d}. We can rationalize equation 3.5 into real part and imaginary part, which is $\varepsilon = \varepsilon_R + i\varepsilon_I$, and we have

$$\varepsilon_R(\omega) = 1 - \frac{\omega_p^2}{\omega^2 + \gamma^2} \quad (3.6)$$

$$\varepsilon_I(\omega) = \frac{\gamma\omega_p^2}{\omega(\omega^2 + \gamma^2)} \quad (3.7)$$

Equation 3.6 and 3.7 can describe the behavior of metal particles under illumination of light with frequency ω . Note that for typical noble metals at visible and infrared region,

$\omega_p > \omega$, and it makes the real part of dielectric constant is negative^{12, 51c, d}. From Maxwell equation and few steps calculation, we can obtain the dispersion relation $k^2 c^2 = \omega^2 - \omega_p^2$, where c is speed of light and k is wavevector. When $\omega_p > \omega$, the wavevector k is pure imaginary number, and it means light cannot penetrate into metals, which matches general properties of metals, shiny and colorful. If $\omega_p < \omega$, k becomes a positive number, and it means light can penetrate into metal at such high frequency region. Metals become pure dielectric materials and transparent at this region^{12, 51c, d}.

Free electron gas model (Drude model) provide a successful qualitative explanation of how metals behave under illumination of light. However, this model only has acceptable prediction at infrared region, and the experimental values of dielectric constants deviate greatly from prediction of this model in visible region especially for the imaginary part. The detailed comparison of the experimental values and theoretical values can be found in standard textbooks^{12, 51d}. To correct the deviation from theory, we need to correct the free electron model. The effect we need to consider is the transition of electrons from lower energy bands into the conduction band, the interband transition^{12, 51c, d}. This situation can be considered as excitation of bounded electrons instead of free electron. We can still treat this problem as harmonic oscillator, but we have to consider the restore force term, which can be written mathematically as^{12, 51c, d}

$$\frac{d^2x}{dt^2} + \gamma \frac{dx}{dt} + \omega_0^2 x = -\frac{eE(t)}{m} \quad (3.8)$$

where ω_0 is resonance frequency of bounded electron. The interband dielectric constant can be solved by the same trial solution technique. Therefore, we can obtain

$$\varepsilon(\omega) = 1 - \frac{\omega_p^2}{(\omega^2 - \omega_0^2) + i\gamma\omega} \quad (3.9)$$

Again, we can separate real part and imaginary part of dielectric constant for this interband model, so we have

$$\varepsilon_R(\omega) = 1 - \frac{\omega_P^2(\omega^2 - \omega_0^2)}{(\omega^2 - \omega_0^2)^2 + \gamma^2\omega^2} \quad (3.10)$$

$$\varepsilon_I(\omega) = \frac{\gamma\omega_P^2\omega}{(\omega^2 - \omega_0^2)^2 + \gamma^2\omega^2} \quad (3.11)$$

After interband transition effect is considered, the theory values and experimental values of dielectric constants are pretty consistent with wavelength higher than 500 nm and still deviate greatly in the region with wavelength below 500 nm^{12, 51d}.

Now, we have a model to describe dielectric constant behavior at different incident light frequencies for noble metal particles. From this model, we realized that the conduction electrons on the surface of noble metal particles play an important role. After excitation of light, the surface conduction electrons will oscillate coherently with incident light. If the particle size d is much smaller than wavelength of incident light λ ($d \ll \lambda$), the surface electrons oscillate in the same phase with incident light, and retardation effect is not necessary to be considered. Researchers name the oscillating surface electrons as surface plasmons, and the condition of $d \ll \lambda$ is quasi-static approximation^{12, 51d, 53}. Next, we examine the relationship among electric field, dielectric constant, and shape of metal particles. Consider a noble metal sphere, the simplest geometry, under quasi-static limit (Figure 3.1(a)), and incident field E_0 is along z direction. The dielectric constant of the sphere particle is $\varepsilon_1(\omega)$, which includes real part and imaginary part. The dielectric constant of the surrounding medium is $\varepsilon_2(\omega)$. To simplify the discussion, we assume that the medium is pure dielectrics, and dielectric constant is real number. Next, we can solve the related Maxwell equation. In this electrostatic situation, there is no surface charge. The Maxwell equation we need to solve is $\nabla^2 V = 0$, also known as Laplace equation, where V is the potential, and ∇ is gradient⁵². After we solve Laplace equation and obtain V , electric field E is equal to $E = -\nabla V$. The techniques to solve Laplace

equation are well-documented in many textbooks and literatures.^{12, 51d, 52} Here, we just write the solution

$$V_{in} = -\frac{3\varepsilon_2}{\varepsilon_1 + 2\varepsilon_2} E_0 r \cos \theta \quad (3.12)$$

$$V_{out} = -E_0 r \cos \theta + \frac{\varepsilon_1 - \varepsilon_2}{\varepsilon_1 + 2\varepsilon_2} E_0 d^3 \frac{\cos \theta}{r^2} \quad (3.13)$$

where in and out represent the potential inside the sphere and outside the sphere. E_0 is the incident electric field, d is the radius of the sphere, r and θ are the position and angle in spherical coordinate respectively. After taking derivatives of both potentials, we can obtain electric field inside the sphere and outside the sphere^{12, 51d, 52}.

$$E_{in} = -\frac{3\varepsilon_2}{\varepsilon_1 + 2\varepsilon_2} E_0 (\cos \theta \cdot \hat{r} - \sin \theta \cdot \hat{\theta}) \quad (3.14)$$

$$E_{out} = E_0 (\cos \theta \cdot \hat{r} - \sin \theta \cdot \hat{\theta}) + \frac{\varepsilon_1 - \varepsilon_2}{\varepsilon_1 + 2\varepsilon_2} E_0 d^3 \frac{(2\cos \theta \cdot \hat{r} + \sin \theta \cdot \hat{\theta})}{r^3} \quad (3.15)$$

where \hat{r} and $\hat{\theta}$ are unit vectors of r and θ direction respectively. The first term $E_0 (\cos \theta \cdot \hat{r} - \sin \theta \cdot \hat{\theta})$ of both equation 3.14 and 3.15 is equal to $E_0 \hat{z}$, which is the incident field. In classical electrodynamics, if one places an electric dipole p at the origin of the coordinate, the resulting electric field is^{12, 51d, 52}

$$E_{ind} = \frac{p}{4\pi\varepsilon_0\varepsilon_2 r^3} (2\cos \theta \cdot \hat{r} + \sin \theta \cdot \hat{\theta}) \quad (3.16)$$

which is very similar to the second term of E_{out} . We define dipole moment p ^{12, 51d, 52}

$$p = 4\pi\varepsilon_0\varepsilon_2 d^3 \frac{\varepsilon_1 - \varepsilon_2}{\varepsilon_1 + 2\varepsilon_2} E_0 = \alpha \varepsilon_2 E_0 \quad (3.17)$$

and α is corresponding polarizability^{12, 51d, 52}

$$\alpha = 4\pi\varepsilon_0 d^3 \frac{\varepsilon_1 - \varepsilon_2}{\varepsilon_1 + 2\varepsilon_2} \quad (3.18)$$

Therefore, we have $E_{out} = E_0 + E_{ind}$. It means if incident field E_0 interacts with the dielectric sphere, the sphere is polarized and behaves like an electric dipole under the quasi-static approximation. The induced dipole produces extra electric field E_{ind} . These equations are the fundamentals of localized surface plasmons. One can see that the E_{ind}

approaches to maximum if the dielectric constant of sphere and dielectric constant of medium match the relation $\varepsilon_1 = -2\varepsilon_2$. Typically, the dielectric constant of medium is a positive real number such as water and air. Therefore, this condition can be fulfilled with the sphere composed of noble metal, whose real part of dielectric constant has negative number and imaginary part is a small number. We can say it is the resonance condition of noble metal spheres when $\varepsilon_1 = -2\varepsilon_2$.

Scattering and absorption are also two important light and matter interactions and can be determined experimentally. Scattering cross section C_{sca} and absorption cross section C_{abs} for a sphere can be written as^{12, 51a}

$$C_{sca} = \frac{k^4}{6\pi\varepsilon_0^2} |\alpha|^2 = \frac{8\pi}{3} k^4 d^6 \left| \frac{\varepsilon_1 - \varepsilon_2}{\varepsilon_1 + 2\varepsilon_2} \right|^2 \quad (3.19)$$

$$C_{abs} = 4\pi k d^3 \text{Im} \left[\frac{\varepsilon_1 - \varepsilon_2}{\varepsilon_1 + 2\varepsilon_2} \right] \quad (3.20)$$

where $k = 2\pi/\lambda$. Both equations clearly show the relation among cross sections, dielectric constants of a sphere and medium, size, and excitation wavelength. The experimental scattering spectra of gold nanoparticles are well-known for their resonance peak around 550 nm and match with the theory prediction^{12, 51a, 51d}.

From the discussion above, one can see that the localized plasmon is sensitive to the composition, and size of particles, excitation wavelength and properties of medium. Also, shape is an important factor of surface plasmon. Different shapes lead to various solutions of Maxwell equation, and thus, the optical properties are different. For example, we can consider cylinder shape, and the solution of dipole moment is $p \propto \frac{\varepsilon_1 - \varepsilon_2}{\varepsilon_1 + \varepsilon_2}$, which is different from sphere⁶. Therefore, the following properties such as scattering and absorptions between sphere and cylinder are also different. Moreover, only some particular shapes can have analytical solutions, and most shapes need numerical solutions

such as discrete dipole approximation (DDA)⁵⁴ and finite-difference time domain method (FDTD)⁵⁵.

So far, localized surface plasmon theory can successfully explain the scattering and absorption behaviors of single noble spheres. However, in SERS history, single nanosphere is seldom reported to be a SERS active substrate. In the beginning, SERS was discovered in rough electrodes surfaces⁴⁸. Pioneering two independent single molecule SERS works⁴⁹ and continuous work by Brus et al suggest that the aggregates of nanoparticles are good SERS active substrate while single nanoparticle is not⁵⁶. Figure 3.1(b) is the smallest unit of aggregate, dimer spheres with gap. Simply speaking, both spheres are polarized and behaved like electric dipoles, and both dipoles couple strongly with short gap distance. Therefore, the electric field is enhanced enormously by decreasing gap distance. Also, the electric field is confined between two spheres (at gap). It is analogy of antenna theory in communication field^{51d}. Some researchers also call these structures which can confine strong electric field as nanoantenna^{51d}. With the fast development of computational techniques, such dimer structures can be performed easily to obtain the values of electric field. For example, Schatz and coworkers report radius 30 nm Ag sphere has maximum value of square module of electric field E^2 about 100 at excitation wavelength 369 nm^{51b, 57}. The maximum E^2 is 10^4 of 2 nm gap and radius 30 nm dimer structures at 520 nm excitation and mostly is confined at gap⁵⁷. Different gap sizes have different effect on field enhancement. Such highly enhanced local electric field is a key to have observable SERS signals. In addition, one can see the plasmon resonance wavelength has a significant red shift for aggregation structures compared to single sphere in their papers^{53, 57} and other literatures^{6, 9}. The choice of excitation wavelength is also an important factor for SERS study.

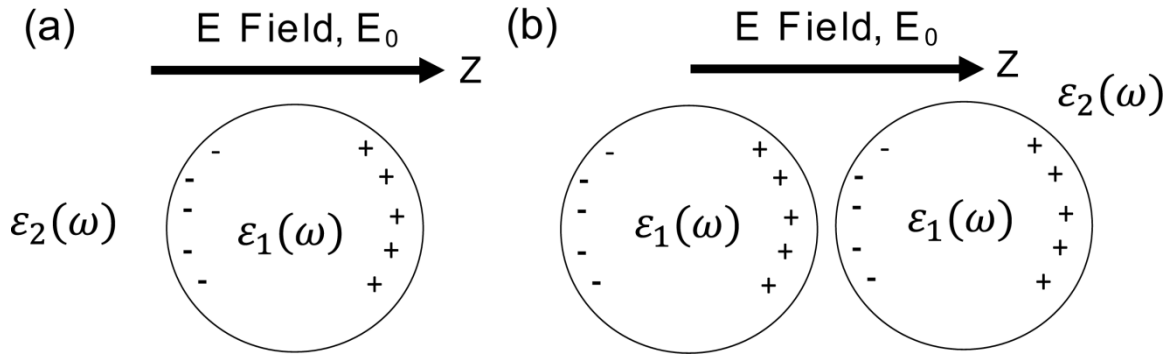


Figure 3.1: (a) The sphere with radius d and dielectric constant $\epsilon_1(\omega)$ is placed in the medium with dielectric constant $\epsilon_2(\omega)$. After interacting with electric field E_0 along with z direction, one can see the surface charges are induced by E_0
 (b) Dimer structure with small gap under E_0 excitation

3.1.2 Introduction to surface enhanced Raman scattering (SERS)^{6,9}

Since the discovery of SERS, researchers have been attempted to understand how Raman signals can be enhanced so many orders. They have believed that SERS can be widely applied to various areas such as biological sensors⁵⁸ if its mechanism is well-understood. Now the most researchers have consensus that incredible enhancement of SERS^{6,9} can be explained by two main mechanisms—electromagnetic field (EM) enhancement and chemical (CM) enhancement—to explain. The origin of EM mechanism is from localized surface plasmon resonance (LSPR), which we already discuss in previous section. We know that LSPR is closely related to the composition element, size, shape, and environment of nanoparticles^{50e, 53}. We also know that the aggregate structure is a good SERS substrate, and the electric field of dimer structure can be several orders of magnitudes higher than monomer under surface plasmon resonance condition^{6,9}. Because of the improvement of fabrication techniques on nanotechnology, researchers have developed different nanostructures to investigate their field enhancement effects⁵⁹. In general, the discontinuity of the structures such as gap, void and sharp tip can generate

high electric field when interacting with EM field. The electric fields of these structures can be explained mostly by plasmon theory, and the lightning rod effect is minor effect if the structure has sharp tip^{12, 51d}. These structures can be modeled by electrodynamic computational programs to calculate the theoretical field enhancement and compare with experimental results. The upper part of Figure 3.2 shows some examples of high localized field enhancement structures listed in literatures including aggregates⁶⁰, gap⁶¹, sharp tip⁶², crescent⁶³, V-groove⁶⁴ and void⁶⁵, and the corresponding simulation results in literatures are presented in the bottom panel of Figure 3.2.

Until now, we only consider the metal part of SERS and have not discussed the molecular effect yet. In brief, we hope to understand how much Raman signals are enhanced after placing molecules on metal nanoparticles; in other words, we need to find the enhancement factor. We know that Raman scattering results from the induced dipole radiation of molecules, and induced dipole is proportional to the incident field E , i.e. $P_M = \alpha_M E$, where p is dipole moment, α is molecular polarizability, and capital M refers to the molecular properties to distinguish from the dielectric materials^{6, 9}. We also see the similar equation in section 2.1.1 where we expand polarizability by Taylor expansion and discuss its physical meaning. Therefore, we need to consider both effects of electric field enhancement by plasmon and polarizability of molecules when we discuss the origin of SERS^{6, 9, 66}. Next, we place molecules on the metal particles such as sphere and excite the system with incident field E_0 . From the discussion section 3.1.1, we know that the electric field is enhanced at plasmon resonance condition, and the electric field becomes⁶⁶

$$E_{out} = E_0 + E_{ind} \quad (3.21)$$

which we know the exact solution of E_{ind} for metal sphere. A molecule placed very closed to metal surface experiences the electric field E_{out} and induces a dipole moment

$P_M = \alpha_M E_{out}$. The induced oscillating dipole creates its own electric field E_{dip} and radiates at Raman frequency. This new induced electric field E_{dip} also interacts with the metal particle again to generate a new secondary scattering dipole and electric field at Raman frequency. After introducing the molecules on metal particles, one can see that the interactions between molecules and metal particles become much complicated. Kerker et al solved the special case of a molecule placed closed to metal sphere⁶⁶, and they found that the field enhancement is closed related to factor $g = \frac{\epsilon_1 - \epsilon_2}{\epsilon_1 + 2\epsilon_2}$, which we discuss in previous section. However, as we state earlier, only few specific cases can have analytical solution, so the field enhancement question is really complicated for different morphology samples. Therefore, appropriate approximation is needed, and many researchers have reported the approximated electric field enhancement factor (EF)^{6, 9} as

$$EF = \frac{|E_{out}|^2 |E'_{out}|^2}{|E_0|^4} \quad (3.22)$$

where E_0 is incident field, and E_{out} is output field after local field enhancement mechanism. The fields are evaluated at the frequency of incident light and the frequency of Raman scattering, which represented without primed and with primed symbol respectively. One can further assume that the output fields at two frequencies are almost the same, i.e. $E_{out} \sim E'_{out}$, so EF is proportional to E^4 . This is so-called E^4 approximation and is commonly reported in the literatures^{6, 9, 50a, 67}.

Until now we discuss the representation of enhancement factor based on electromagnetic theory. In reality, the evaluation of enhancement factors is one research topic, and many authors reported their enhancement factors in various evaluation methods. Le Ru and Etchegoin's SERS textbook⁶ and paper⁶⁸ have very detailed

discussion of all possible ways to evaluate enhancement factors. Here, we just introduce the most common expression

$$EF = \frac{[I_{SERS}/N_{surf}]}{[I_{RS}/N_{vol}]} \quad (3.23)$$

where I_{SERS} is SERS intensity, I_{RS} is Raman intensity in bulk measurement, N_{surf} is numbers of molecules bound on metal surface, and N_{vol} is numbers of molecules having Raman scattering in bulk measurement. It is easy to see that this equation evaluates the ratio between averaged SERS intensity for each molecule on metal surface and averaged Raman intensity for each molecule in excitation volume. In other words, equation 3.23 tells us how much Raman signals one molecule can be enhanced by SERS compared to the normal Raman process. Many researchers have synthesized various structures and performed SERS experiments^{6, 9, 51b}. They have evaluated experimental enhancement factors and compared to theoretical values by computational simulation. One thing needs to keep in mind is the evaluation of experimental enhancement factor is difficult and has huge possible errors. One possible source of errors comes from the estimation of N_{surf} , and it is difficult to estimate a precise value of N_{surf} .

Another effect on SERS enhancement mechanism is chemical enhancement. Chemical enhancement (CM) is due to chemical effects from the interaction between molecules and metal surfaces such as charge transfer effect^{9, 50a, b, 50d}. Remember that $P_M = \alpha_M E$ of an induced dipole, and it generates Raman scattering. EM enhancement mainly modulates the electric field E term. The CM effect results from the formation of new molecule-metal surface complex and changes the polarizability of the molecule⁹. The polarizability is a tensor, so the molecular orientation is one of the factors to change polarizability. After molecules and metal surface form a surface complex, the molecular orientation is restricted, and the polarizability is changed. Also, the surface complex may

change the selection rule of bulk Raman scattering, the so-called surface selection rule⁶⁹. Charge transfer effects from molecule to metal surface are also commonly reported in literatures⁷⁰. These effects cause the CM enhancement. Typically, most SERS experiments demonstrate that enhancement factor^{6, 9, 51b} is about 10^6 - 10^8 . From theoretical electrodynamic calculation, EM enhancement factor is usually less than 10^6 . Therefore, CM enhancement factor is well-accepted from 10^1 to 10^2 much less than EM mechanism^{6, 9, 50a, b} although there still some reports show unexpectedly high CM enhancement factor⁷¹. Because the EM mechanism contributes much more enhancement of overall signals, our research mainly focuses on studying the correlation between EM enhancement and SERS signals.

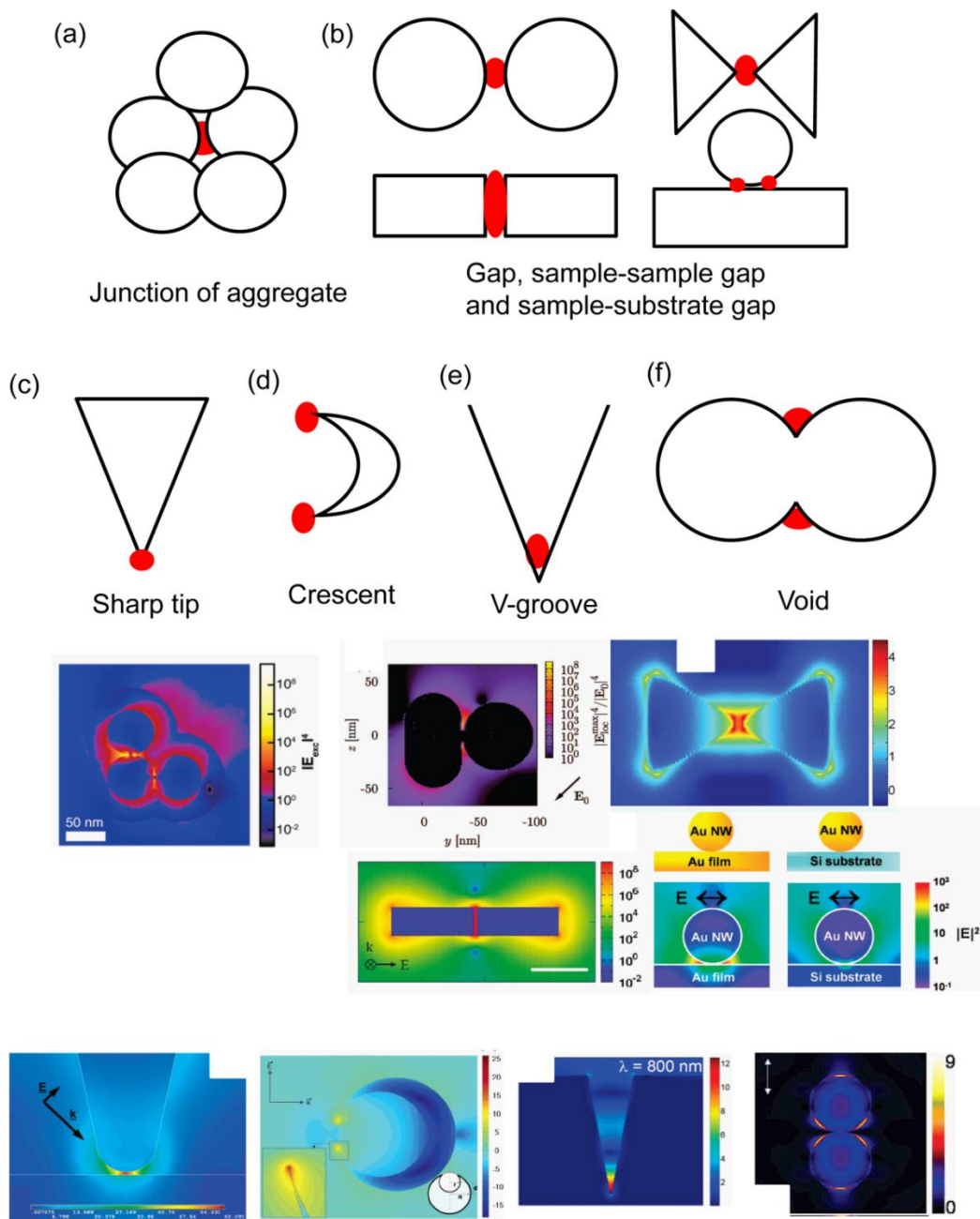


Figure 3.2: Various reported structures with strong localized electric field enhancement (top) and corresponding simulation results in literatures. The red spots represent highest electric field position (a) junction of aggregate⁶⁰, (b) gap⁶¹ between sphere, rod, and bowtie and gap between sample and substrate (c) sharp tip⁶², (d) crescent⁶³, (e) V-groove⁶⁴ (g) void⁶⁵

3.1.3 Nonlinear optics and SERS

From the discussion above, we know that EM and CM mechanisms now are researchers' consensus of SERS origin, and EM contributes most of signal enhancement. The important work conducted by Van duyne group showed that the maximum enhancement can be achieved by exciting the blue-shifted spectral position relative to plasmon resonance position⁷². This phenomenon can be explained by considering the EM effect. EM effect predicts that the enhancement factor is roughly proportional to $|E_{out}|^2|E'_{out}|^2$. The products should reach maximum when we excite the system at blue shifted position of plasmon resonance position instead of directly exciting at plasmon resonance position. Some groups controlled polarization direction to study the relation between SERS intensity and electric field direction to demonstrate the valid EM enhancement argument⁷³. In our work, we aimed at finding direct correlation between electric field and SERS intensity experimentally.

Here, we chose nonlinear spectroscopy as our weapon to fight with SERS, and we hoped that using nonlinear optics can provide clear experimental evidence of EM mechanism of SERS because nonlinear spectroscopy is a great tool to probe local field enhancement by EM field. For example, two photon luminescence (TPL) signals should show a quadratic dependence on the intensity of incident laser¹⁶, more significant dependence than linear spectroscopy such as Raman spectroscopy. Many research groups already performed TPL^{65, 74} on various gold systems thus far to study local field enhancement. The early classic work was done by Shen's group¹³, and his group demonstrated not only TPL but also second harmonic generation (SHG)⁷⁵ on flat and rough gold films. Novotny's group also studied local field enhancement on gold films and gold tips, and they found very broad continuum TPL from these systems⁷⁶. Recently, due to the fast development of lithography techniques, many other groups can study these

nonlinear effects on different systems. Moerner's group synthesized bowtie structures by e-beam lithography and performed a series of studies on this bowtie structure such as two photon luminescence^{74a, 77}, polymerization of photoresist⁷⁸ and chemical enhancement effect⁷¹ on SERS. Bouhelier et al studied surface plasmon properties and two photon luminescence by adjusting both polarization and aspect ratio of the single gold nanorod^{74b}. Ghenuche et al demonstrated spectral mode mapping on single nanorod and nanoantenna (dimer nanorod with gap). They changed excitation wavelength to match with the size of single nanorod and nanoantenna for resonance effect⁷⁹. Potma and Penner groups used electrochemical method to synthesize nanowires and performed two photon luminescence and four-wave mixing to understand local field enhancement effect^{74e, 80}. Finally, TPL of noble metal nanoparticles is not only for a pure research topic of physics but also can be used in biological application. For example, Cheng et al used single nanorods to conduct in vivo imaging of biological system⁸¹. These results showed the possibility of probing local electric field of noble metal nanoparticle systems by nonlinear optics.

Theoretically, both SERS and nonlinear spectroscopy should correlate spatially because they are both related to electric field. For SERS, SERS intensity is proportional to the product of square modules of electric field at incident frequency and square modules of electric field at Stokes frequency, $|E_{out}|^2|E'_{out}|^2$. On the other hand, intensity is proportional to fourth power of electric field for TPL. However, most literature only focused on either SERS or TPL and studied one of their properties. Some literature explored both SERS and TPL properties in theoretical point of view. To our best knowledge, just few literatures discussed correlation between SERS and TPL experimentally. Okamoto's group studied the correlation between SERS and TPL on gold nanoparticle dimers⁸². They found TPL more focus on the gap of dimers, but SERS more

focuses on the edge of the dimer. Other reports are from Lupton group. When they excited fractal silver films, the white light (WL) is generated, and they assigned WL as a two photon process. They also found WL has anti-correlation with SERS⁸³. Very recently, they performed systematic investigation of SERS and two photon correlation on silver mirror films⁸⁴. They changed the laser polarization and wavelength, probed the emission anisotropy, and studied power dependence and the emission spectra. They concluded the excitation pathway of SERS and two-photon excitation was very similar, but emission pathway for both processes was very different. It caused the anti-correlation between both SERS and TPL. Their work was a very important reference for our work, and we shall discuss more in result and discussion section.

3.1.4 Our work of gold nanorods and pyramids

We know that the morphology of noble metal nanoparticles affects the plasmonic structure greatly. Hence, if we want to systematically study the field enhancement of nanoparticles, we need to choose a system whose structures can be manipulated easily. Also, we know that gap distance between two nanoparticles is the main factor of localized electric field enhancement, so we also have to control the size of gap. According to these considerations, we first conducted our field enhancement study in nanorod system. We adapted the template method from the literature⁸⁵ and deposited different component of nanorods such as gold, silver and nickel by electrochemistry methods. The silver or nickel can be etched by nitric acid (silver) or hydrochloric acid (nickel). Different lengths of nanorod compositions can be controlled by adjusting the amount of currents flowing to the system. We successfully synthesized the nanorods and etched the silver or nickel part to have gap structure. We obtained some preliminary results about nonlinear methods such as two photon photoluminescence and four-wave

mixing from this nanorod system. However, we found that short pulse laser and strong field enhancement effect easily damaged our samples. Although we used silica layer to protect the samples⁸⁶, samples still damaged after long time laser exposure. Therefore, we had to find another system to study field enhancement.

Next, we chose gold pyramids as our system to study correlation between SERS and TPL. The gold pyramids were on gold film, and we believed gold films can dissipate the heat generated by multiphoton processes faster than glass substrate which we used in nanorod experiments. The gold pyramid system was independently investigated by several groups before our work. Odom's group performed a systematic gold pyramid studies about linear optical properties such as Rayleigh scattering and SERS⁸⁷. Different from Odom's work which mainly focuses on the optical properties of single gold pyramid, Jiang's group synthesized pyramid arrays and performed SERS on these pyramid arrays⁸⁸. Moreover, by manipulating the structure of pyramid, which had the same effect as grating, Norris et al showed that they can focus plasmon on tip of pyramid⁸⁹. However, as we discussed previously, no literature discusses correlation between SERS and TPL on gold pyramid. Researchers studied correlation between SERS and TPL on gold nanosphere dimers and fractal silver films. Compared to their systems, we chose pyramid to study SERS and TPL properties because the morphology of pyramids can be controlled more precisely than nanosphere and silver film. We know that morphology of nanoparticles determine their LSPR structure, and LSPR structure is closely related to SERS and TPL. Also, ultrasmooth surfaces of gold pyramids^{89a} eliminate the possibility of field enhancement by rough surfaces.

Thus far, in our study, we found that pyramid structures affected SERS signals significantly. We also have some results to correlate both SERS and TPL signals. We synthesized several different shapes of pyramids and investigated their SERS and TPL

properties. We found SERS were very inhomogeneous in pyramid array structures although they are looked pretty similar under low magnification of scanning electron microscope (SEM). It was consistent with other groups' results of other SERS substrates⁹⁰. Moreover, polarization of incident light played an important role in both in SERS^{73a, b, 82a} and TPL^{74e, 82a}. We adjusted two polarization directions of SERS and TPL excitation laser to the same direction. We find that the small gap structure (V-groove) has high possibility to generate high SERS and TPL signals as discovery of other groups⁹¹. However, we cannot conclude both of them are totally correlated as theory predicted. Lupton and his coworkers provided a possible explanation to our results⁸⁴. Another possible reason is the different coupling among SERS, TPL and LSPR. We know that the enhancement of SERS and TPL are related to the frequency of incident laser and the frequency of emission light. Both local field at frequency of incident light and emission light also couple with LSPR, so the structures of LSPR at both frequencies determine the coupling efficiency. Although we use almost same frequency for both SERS and TPL to excite sample, their emission frequencies locate at both sides of incident light. Therefore, the uncorrelated SERS and TPL results might result from this inconsistency.

3.2 EXPERIMENTAL SECTION

3.2.1 Synthesize Metal Nanorod by Template Method⁷⁸

Here, we briefly introduced our experimental methods of template synthesis and nanorod synthesis. The detailed procedures can be found in the appendix of this dissertation. We slightly modified Masuda's method^{85b} to synthesize porous anodic aluminum oxide (AAO) templates. Figure 3.3 summarizes the synthesis procedures. First, a high-purity aluminum foil was electropolished in a mixture of HClO₄ and C₂H₅OH (volume ratio 1:4). The polished aluminum was then anodized in 0.4 M oxalic acid

aqueous solution under constant voltage of 40 V for 12 hours. Next, the anodized aluminum oxide was immersed in 0.2 M chromium oxide of 0.6 M phosphoric acid solution for six hours to etch out the top oxide layer. The foil was then anodized again in 0.4 M oxalic acid again under 40 V for 24 hours. In order to detach top porous layer, the second anodized aluminum was dipped into saturated HgCl_2 solution. Finally, the pore-widening step was performed by immersing AAO membranes in 8.5% phosphoric acid solution for one hour. We deposited 200 nm silver layer on the AAO membrane. This metal layer served as a conductive layer for later electrochemical deposition. Different kinds of plating solution and deposition potentials were used for electrochemical deposition of different metal segments. Here, we deposited gold for plasmon study and nickel for sacrifice metal. For controlling the length of different segments, controlled amount of charges and potentials were applied (see Figure 3.4 and appendix). After depositing nano-barcode, we used concentrated nitric acid to dissolve silver conductive layer, and concentrate sodium hydroxide to dissolve the AAO template to obtain a colloidal solution of nano barcodes. Concentrated hydrochloric acid was used to etched out the sacrifice nickel layer to obtain nano dimer.

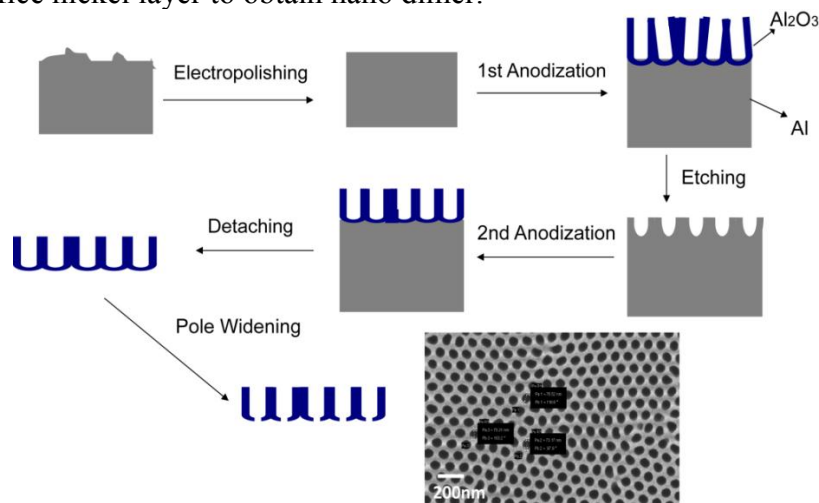


Figure 3.3: The synthesis procedures of anodized aluminum oxide (AAO) template

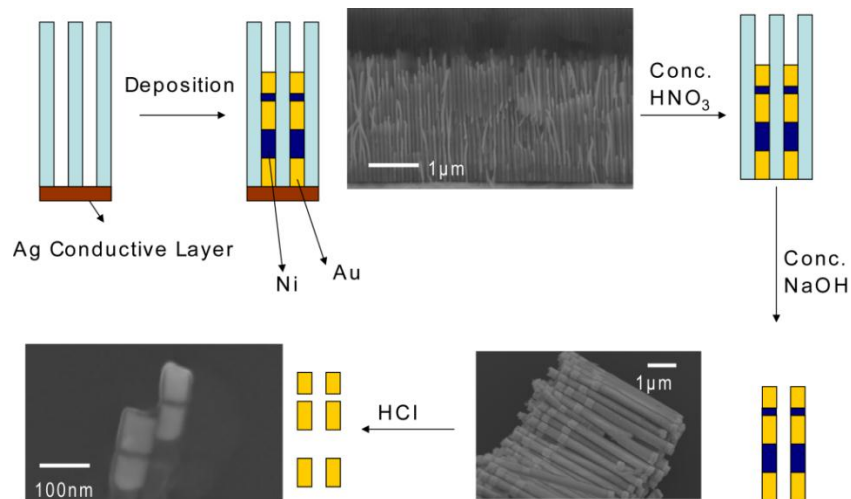


Figure 3.4: The synthesis procedures of nanorods and nanodimers by template method

3.2.2 Coating Silica on Nanorod

We adapted the Xia's method to make silica coating on nanorods⁸⁶. First, we mixed 0.01M citrate and the nano-barcode colloidal solution. This process coated the surface of nano barcode with citrate anions. Then, we added the colloidal solution into the mixture of 0.01M tetra-ethoxy silane (TEOS) solution in 2-propanol, water, and 30% ammonium mixture solution. After stirring for 1hr, we centrifuged the solution and redispersed nano-barcodes in 2-propanol solution to obtain well-dispersed silica-coated metal nanobarcode solution. Before optical measurement, the sample was stirred with 1M HCl overnight to etch out the sacrifice metal. Figure 3.5 shows typical TEM images (FEI Tecnai) of silica coated nanorod (a) and nanodimer etched by acid (b).

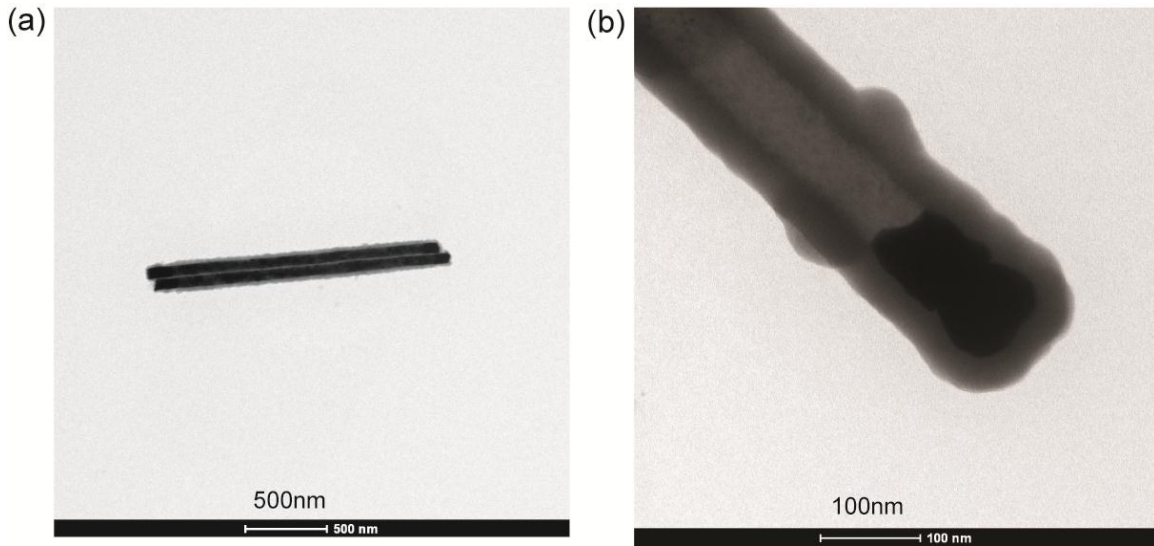


Figure 3.5: TEM images of (a) silica coated nanorods and (b) etched nanodimers

3.2.3 Simulation of nanorods by discrete dipole approximation (DDA)

There are several numerical methods to simulate the electric field distributions around metal nanoparticles such as multiple multipole method, the finite difference time domain method (FDTD)⁵⁵ and discrete dipole approximation (DDA)⁵⁴. Among all these methods, DDA is an easy and robust method to simulate the plasmon structure of arbitrary shaped nanoparticles. We used DDA to simulate the possible monomer and nanodimer structures whose plasmon resonances match our laser wavelength. According to our results, a monomer of 130 nm length and 70 nm of diameter had a resonance at 790 nm, which is the maximum intensity of our laser output. For nano-dimers, a structure with monomers of 84 nm long and the 70 nm diameter with the gap size of 10 nm had the same resonance wavelength as monomer. The grid size we used here was 2 nm.

3.2.4 Pyramid synthesis procedures^{87a, 88a, 89a}

Polystyrene with different diameters (Polyscience), isopropanol and methanol (Fisher Scientific), gold (Materion), silicon wafer (100) (University wafer), chromium

etchant (Transene 1020AC), benzenethiol (Aldrich) are used as received without further purification. The suitable size ($\sim 1 \text{ cm}^2$) of wafers were cut along crystallographic orientation, and cleaned with piranha solution (the volume ratio $\text{H}_2\text{SO}_4:\text{H}_2\text{O}_2 = 3:1$) for 30 minutes. Piranha solution not only cleaned the wafer surface but also modified the surface from hydrophobic to hydrophilic. This step was critical for disperse the polystyrene on the wafer surface. Note that piranha solution is extremely dangerous. It should be operated in the hood very carefully. For clean purpose and safety reason, we didn't boil the piranha solution and just keep it warm. The waste piranha solution needed to be treated with huge amount of water and then disposed in a waste container. Then rinse the wafers with a great amount of DI water. Finally, clean wafers were preserved in DI water before use.

In the pyramid project, we have synthesized several kinds of pyramids. According to their numbers and morphology, we can divide them into two main categories: regular pyramid and shaped pyramid, and connected and isolated pyramid. Figure 3.6-3.7 shows the fabrication scheme of both kinds of pyramids. The detailed synthetic procedures were provided below. Basically, the difference between regular pyramid and shaped pyramid was whether the pyramid is completely connected to the flat substrate. As shown in Figure 3.6, the regular pyramid is connected to the substrate. On the other hand, because of the Cr mask, the shaped pyramid was selectively connected to the substrate. In regular pyramid, we can further divide it into two categories, connected and isolated pyramids, if there were more than one pyramid in our system. Here, connected and isolated mean whether the pyramids were connected with each other or not. The detailed synthesis procedures for both connected and isolated pyramids are also provided below.

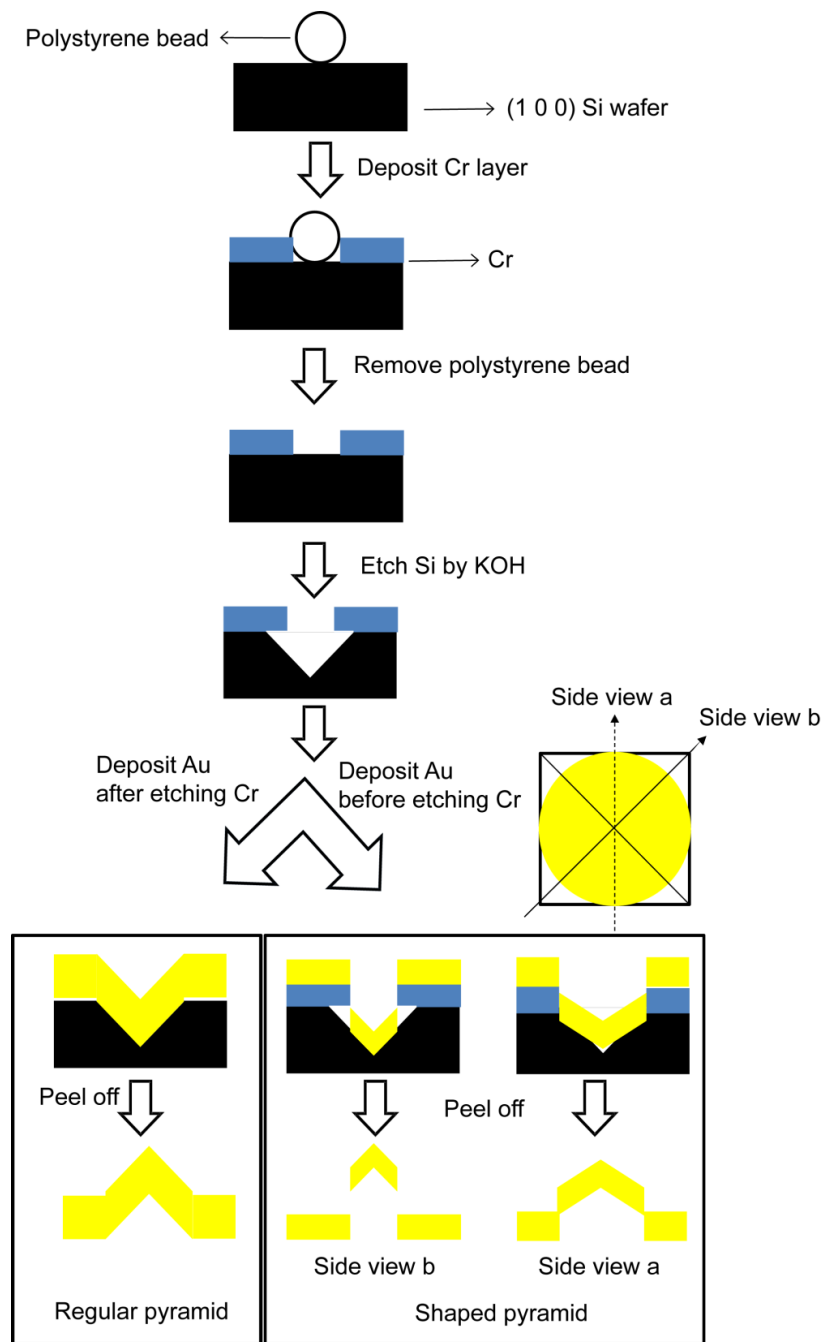


Figure 3.6: The scheme of fabrication of regular pyramid and shaped pyramid

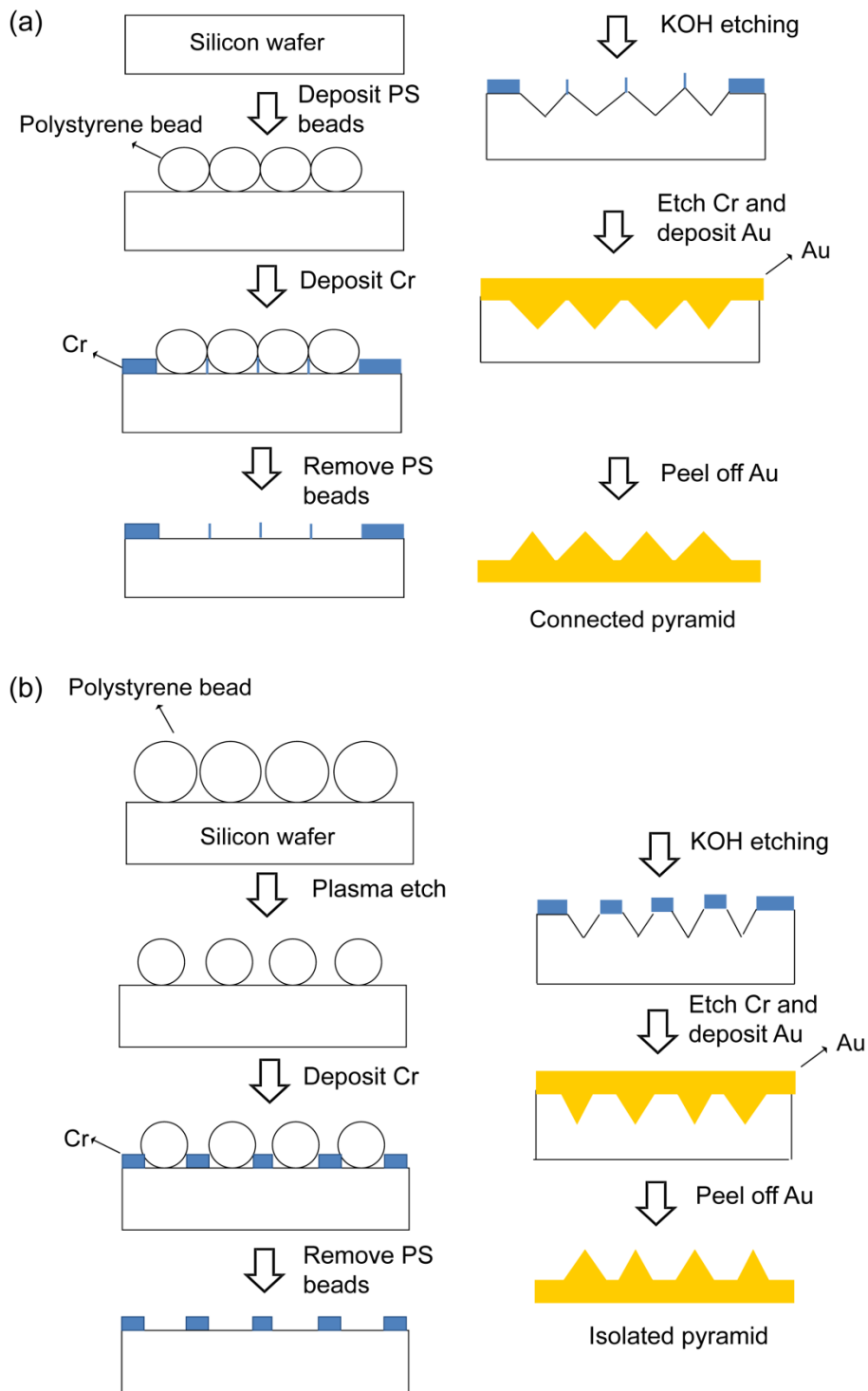


Figure 3.7 The scheme of connected pyramid and isolated pyramid synthesis

3.2.4.1 Fabrication of regular and shaped pyramids

We modified the fabrication process of gold pyramid from literature^{87a, 88a, 89a}. First, different sizes of polystyrene beads were spin coated on piranha treated silicon wafer as mask. While taking wafer out of DI water, keep the wafer surface wet. It was very difficult to disperse polystyrene beads on dry wafer surface. The separation of each polystyrene bead can be controlled by the concentration of stock polystyrene solution and spin coating speed, and it also depended on how homogeneous hydrophilic surface is. Typically, I roughly diluted 10 times of stock solution by DI water, dropped the diluted solution (~200 μ l) on the wafer, and then spin-coated it under 8000 rpm for 1 minute to obtain well-dispersed single polystyrene bead. To obtain higher aggregation, less dilution and lower spin speed were needed. The polystyrene dispersion can be easily checked by looking at the color of wafer surface or by common microscopes. Next, 10 nm chromium layer was deposited as protecting layer by thermal evaporator (Denton). The thickness was monitored by quartz detector, and the deposition rate was 0.1 $\text{\AA}/\text{sec}$ under 5×10^{-5} torr. Then, wafers were sonicated in ethanol for 2 mins to remove polystyrene beads. These wafers were placed in potassium (23 g), isopropanol (33 ml), and water (100 ml) mixture under 65 $^{\circ}\text{C}$ to perform etching process. The etching time differed from various sizes of polystyrene samples (see table 3.1). Next step is main difference between shaped pyramid and regular pyramid. For regular pyramid, chromium layer was first removed by commercial chromium etchant (Transene 1020AC). The optimum chromium etching rate is 32 \AA per second under 40 $^{\circ}\text{C}$ (from the instruction on the bottle). A little longer etching time was applied to the sample to confirm complete removal of chromium. After removing chromium, wafers were rinsed with DI water and treated with piranha solution again to clean organic residues of etchant on the wafer. For shaped pyramid, the remained chromium layer acted as the mask of gold deposition in next step. 200 nm gold and then

10 nm chromium were deposited on both regular and shaped pyramid substrates by thermal evaporator (Denton). The deposition rate is 1.5 Å per second for gold and 0.1 Å per second for chromium. Here, 10 nm chromium layers were deposited to increase the adhesion between gold and adhesive layer from next step. Finally, gold layers can be peeled off by template-stripping method^{89a}. Here, I applied instant Krazy Glue on the wafer and attached a piece of glass on the wafer as a support layer. Finally, I used razor blade to peel off the gold film with pyramid. The morphology and size of gold pyramid was characterized by scanning electron microscope (SEM, Zeiss Supra 40VP). Before SERS experiments, gold layer of pyramids was incubated in 1 mM benzenethiol of methanol solution for 3 hrs and then rinsed with copious amount of methanol to remove extra benzenethiol⁷². The energy-dispersive X-ray spectroscopy (EDX) was performed on SEM (Quanta 650 FEG FEI) with attached detector (Bruker XFlash detector 5010).

PS size (um)	0.20	0.465	0.65	1.0	3.0	4.5	6.0
Etching time (min)	1.5	3.0	4.0	5.0	11	20	25

Table 3.1: The polystyrene (PS) size and the corresponding KOH etching time

3.2.4.2 Fabrication of connected and isolated pyramids

For connected and isolated pyramids, most of fabrication procedures are similar to regular pyramid described in previous section. The fabrication procedures are summarized in Figure 3.7. To make small aggregation of connected pyramid, higher concentration of polystyrene solution and lower spin-coating speed were used. For example, I dropped 200 µl of original 3 um polystyrene stock solution without any dilution and spin coat it under 2000 rpm for 1 minute. The following procedures are same as regular pyramid. To make isolated pyramids, we used reactive ion etching (RIE)

technique to etch deposited polystyrene beads. We first examined the feasibility by applying RIE on both 3 μm and 6 μm polystyrene bead samples. 35 sccm O_2 and 10 sccm Ar were mixed to perform RIE (March Plasma CS170IF) under 60 W⁹².

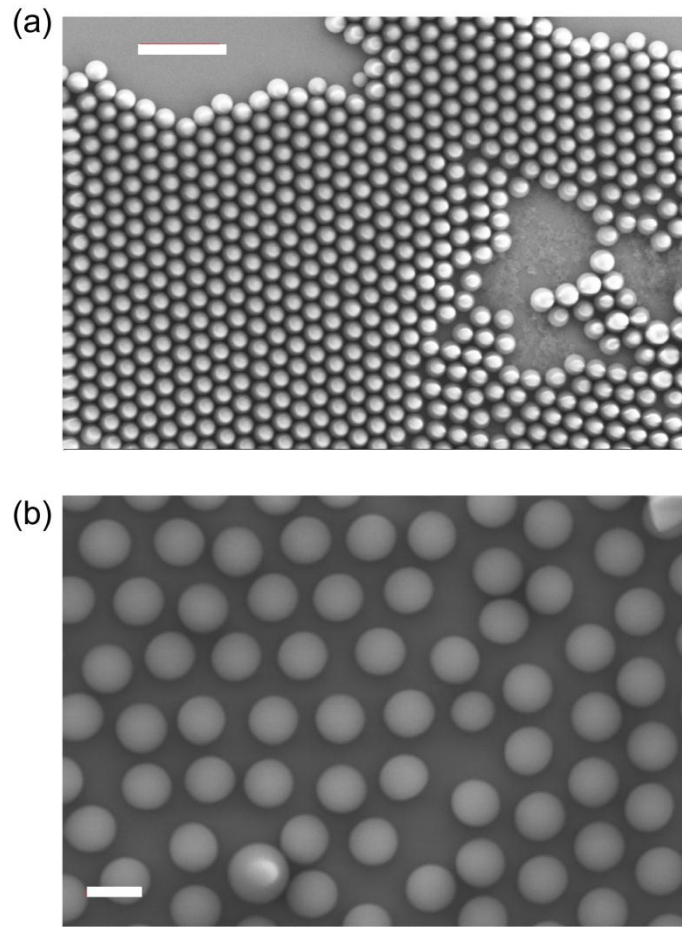


Figure 3.8: The SEM images of RIE treatment effect on self-assembled polystyrene beads (a) 3 μm polystyrene beads without RIE treatment, All polystyrene are closed packing. (b) 3 μm polystyrene beads with 6 min RIE treatment (see text for detailed recipes) Scale bar for (a): 10 μm , (b) 2 μm

Figure 3.8 shows the example of RIE treatment on 3 μm polystyrene beads. Figure 3.8(a) demonstrates polystyrene beads without RIE treatment, and polystyrene beads formed self-assembled monolayer on the wafer. After 6 min RIE treatment, one

can clearly see polystyrene beads are etched. The distances between beads were obviously larger than the ones without any RIE treatment. We also investigated the relation between particle diameter and etching time for 3 μm and 6 μm polystyrene beads. The relationship was plotted in Figure 3.9. One can see that with longer etching time, the diameter of the polystyrene bead became smaller. We attempted to fit both our experimental results linearly. Therefore, we had empirical equations for our system, and we can approximately obtain the required size by both equations. Note that the shapes of polystyrene beads were no longer perfect sphere if we performed too long RIE etching. Safely speaking, RIE time for 3 μm beads is necessary to be less than 10 minutes and is less than 18 minutes for 6 μm beads to maintain sphere shape of beads (Images are not shown).

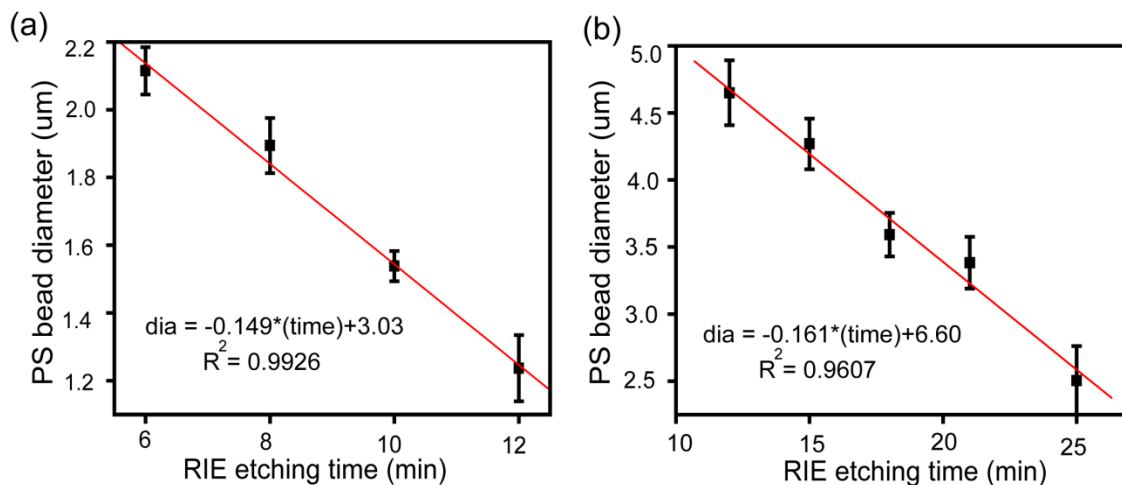


Figure 3.9: The plot of RIE etching time versus the remaining polystyrene (PS) diameter for two sizes of polystyrene beads: (a) 3 μm , (b) 6 μm

After we obtained the empirical relation between etching time and polystyrene diameter, we continued to synthesize pyramids following the procedures described in section 3.2.4. However, we found that the chromium layer of RIE etched samples cannot

resist KOH etching, and almost all the chromium layer were damaged. Therefore, we changed our recipes to fabricate isolated pyramids. Instead of two gas mixture, we only used 35 sccm of pure oxygen and power of 60 W to perform RIE etching. We found that new recipes have much less damage than old recipes. We also found that the chromium layer damaged more seriously while applying longer RIE etching time. According to our experience, isolated pyramids can be successfully synthesized by performing RIE etching time less than 6 minutes (c.f. Figure 3.8(b)). We thought the reason why mixed plasma cannot be used is because the mixed plasma damaged the wafer surface. Therefore, the following chromium layer cannot attach to wafer as perfect as wafers without plasma treatment. We also believed the wafer surface was also damaged by excessively long oxygen plasma etching. After we fixed the etching problem, we can successfully synthesize isolated and connected pyramids to investigate their SERS activity and nonlinear behavior. More results are discussed in result and discussion section.

3.2.5 Optical Setup

3.2.5.1 Optical setup for nanorod experiment

In plasmon project, we aimed at the correlation between nonlinear spectroscopy such as TPL and FWM and linear spectroscopy such as white light scattering and SERS. For nanorod part, as Figure 3.10 shows, we combined three different kinds of optical methods including white-light scattering, TPL, and FWM. For TPL and FWM, the excitation source is a Ti-Sapphire oscillator laser. The repetition rate of the laser is 2 MHz. The laser pulse is controlled by a pulse shaper which is a 640 pixel dual bank liquid crystal spatial light modulator (SLM). Our pulse shaper is designed to cover a 250 nm bandwidth centered at 800nm. The wavelengths of the laser shorter than 740 nm are blocked by a razor blade placed just before SLM. Polarization of Ti-Sapphire laser is

controlled by half wave plate. The pulse is tightly focused by a high NA oil immersion objective. The epi-detected signals are measured by photomultiplier tube (PMT) after filtered by a suitable short wave pass filter. TPL and FWM images are performed by moving XY piezo-stage (P-542.2SL PI) to scan the sample. The scattering spectra, TPL and FWM spectra are recorded by spectrometer (QE6500 ocean optics).

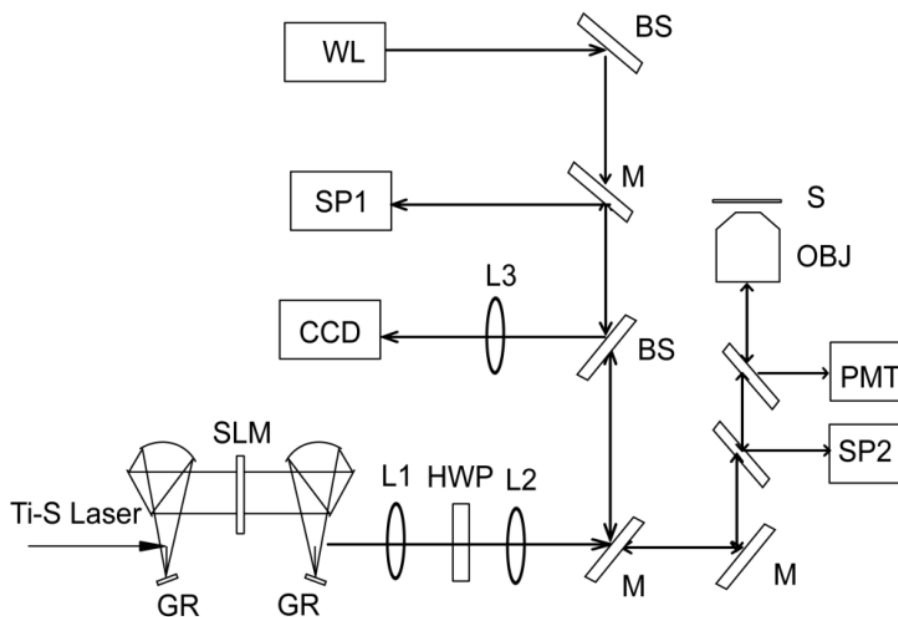


Figure 3.10: Optical setup for nanorod project where white light scattering and femtosecond laser are combined together. The arrows mean the laser direction. M: mirror, L: lens, GR: grating, SLM: spatial light modulator, HWP: half wave plate, BS: beam splitter, WL: white light, SP: spectrometer OBJ: objective, and S: sample.

3.2.5.2 Optical Setup for pyramid experiment

The optical setup in the pyramid experiment is similar to nanorod project and is shown in Figure 3.11. Here, white light transmission image, laser scattering image, SERS image, and TPL image can be acquired within the same setup. A white light source is placed on top of the sample and CCD (Princeton instruments CoolSNAP) is used to

acquire transmission white light image. We replace white light with 785 nm continuous fiber coupled diode laser (B&W TEK Inc), and it serves as SERS excitation light source. The polarization of laser can be adjusted by rotating the output fiber. To precisely control the polarization, a polarizer is placed in front of laser. 795 Dichroic long pass filter (795 DRLP) reflects and the wavelength shorter than 795 nm in 45 degree (laser) and transmits the light with wavelength longer than 795 nm (Stokes Raman shift). The Ti-Sapphire laser is used as TPL excitation light source. Excitation bandwidth and intensity of Ti-Sapphire laser are controlled by SLM. Because the pyramid sample is basically thin gold film attached on glass by glue, the thin film is easily detached from glass by immersing in water for long time. Therefore, water and oil objectives are not suitable choices for pyramid experiments. We use 20X air objective whose NA is equal to 0.75 (Olympus) to focus the laser to the sample. SERS and TPPL signals are collected through the same objective by epi-detection. SERS signals are directed through 795 DRLP to spectrometer, and proper notch filter (Kaiser Optics) is used to eliminate most reflection and scattering of laser. SERS image for each sample is acquired by integrating 1076 cm^{-1} peak, and sample scanning is performed by moving XY piezo-stage (P-542.2SL PI). The setup for TPL image is the same as nanorod part. Because of the correlation purpose, it is critical to confirm the signal position of samples. To achieve the requirement, laser scattering image is first obtained by moving the stage and collecting epi-scattering signals to a photodiode (Thorlabs). Next, with the same scanning parameters, SERS and TPL signals are collected to the corresponding detectors to obtain the image. Finally, we can use image processing software (Photoshop) to overlap scattering images and SERS / TPPL images to know the position of signals.

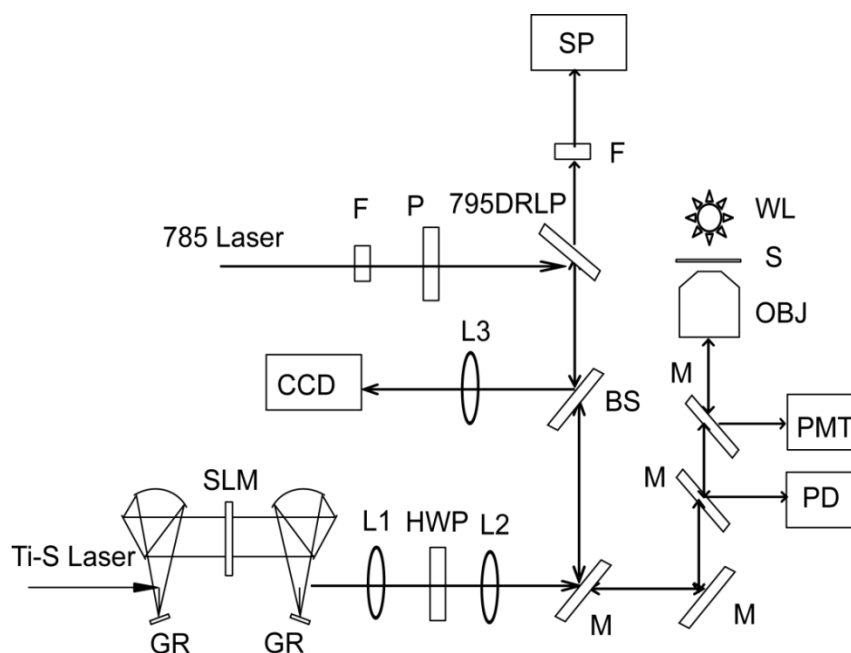


Figure 3.11: Optical setup for pyramid project where two lasers are combined together. The arrows mean the laser direction. M: mirror, L: lens, F: filter, P: polarizer, GR: grating, SLM: spatial light modulator, DRLP: dichroic long pass filter, HWP: half wave plate, BS: beam splitter, WL: white light, SP: spectrometer, PD: photodiode, OBJ: objective, and S: sample.

3.3 RESULTS AND DISCUSSION

3.3.1 Nanorod and nanodimers

In the beginning of this project, we first used DDA to simulate the desired structure of monomer and dimer unit. Because 790 nm was the output spectra maximum position of our Ti-sapphire laser at cavity-dumping mode, we aimed at the structure whose plasmon resonance was about 790 nm. Also, our diameter of AAO was about 70 nm. From these parameters, we first performed far field scattering spectra simulation, and we obtained our desired structure for monomer nanorod was length 130 nm and diameter 70 nm. For dimer, the length of desired structure was 84 nm, diameter was 70 nm, and gap was 10 nm. The simulation results for such dimer structure are summarized in Figure

3.12, and Figure 3.12 represents the results of (a) far-field scattering spectrum, (b) near-field scattering spectrum and (c) square modulation of electric field contour for dimer structure excited at 790 nm, respectively. One can see that the far-field spectrum and near-field spectrum were quite different in structure. For far-field scattering spectrum, only one plasmon resonance was observed in 600-1000 nm region. For near-field spectrum, two peaks were observed; one was about 700 nm, and the other is about 810 nm. One of our goals in this project was to establish near field excitation spectrum of different wavelengths. Finally, field contour in Figure 3.12(c) demonstrated that the most intense field was confined at the gap which is the same as results shown in Figure 3.2. The sharp corners of each nanorod also had high electric field, but the magnitudes are much smaller than the one confined in gaps.

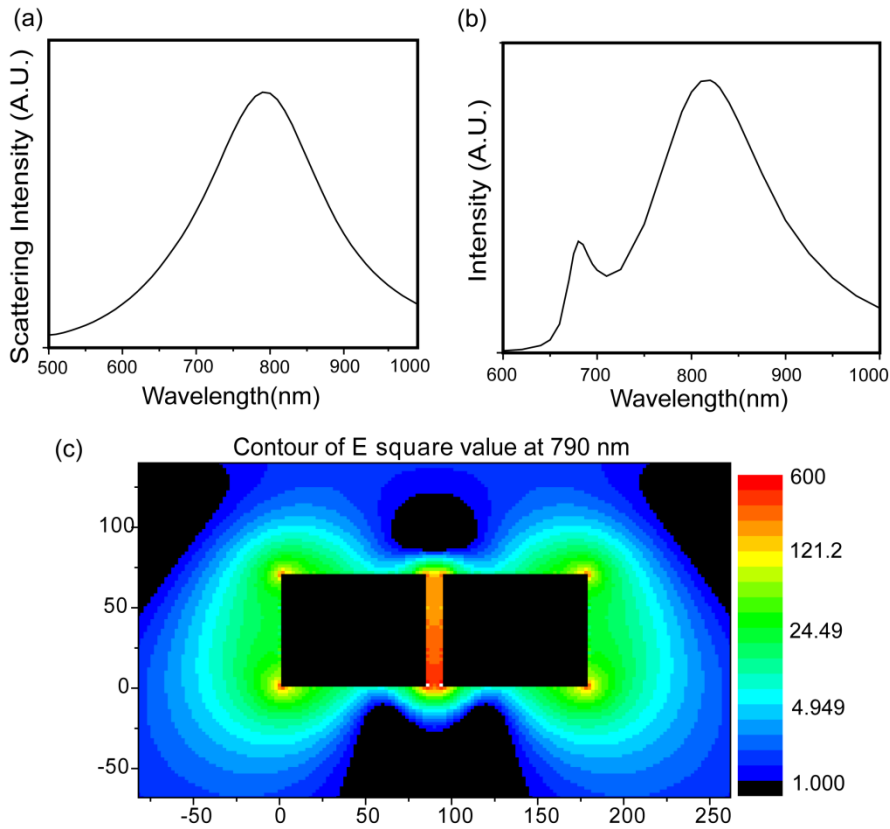


Figure 3.12: DDA simulation results for nanodimers (a) scattering spectra (b) near field spectra (c) the contour of square modulation of field whose excitation wavelength is 790 nm.

We already showed that we can successfully synthesize AAO template, nanorod and nanodimer structures in experimental section. To etch gap, we found that using nickel as sacrifice layer and hydrochloric acid as an etchant are better combination than silver and nitric acid because we can etch the sacrifice layer more completely and without considering any further oxidation of samples by nitric acid. After we obtained the samples, we started our optical experiments. We used TEM grid to label the absolute position of each sample on the glass substrate. Therefore, after finishing all optical experiments, we plugged the sample into SEM and obtained the morphology of each particle.

Figure 3.13 shows the correlation experiments which are consisted of Rayleigh scattering image, TPL scanning image, scattering spectra and corresponding scanning electron microscopy (SEM) images of etched particles. In our setup, we can obtain TPL signals and scattering spectra from an isolated nanoparticle. And we can also characterize the morphology of the same particle in SEM measurement. According to DDA simulation, the plasmon resonance peaks of these particles were around 800nm. However, we found that the plasmon resonance of each nanoparticle was very different and greatly depended on the shape and the gap size of nanoparticles. The TPL image was performed by 790 nm laser excitation and the average power was 46.5 μ W. It is interesting that some nanoparticles were shown in scattering image but not shown in TPL image. Also, there was no obvious correlation between scattering images and TPL images for each sample. Due to the diffraction limit, we cannot determine the real size and structure from our sample by optical measurement. The shape and size of nanoparticles were determined by SEM. We found that the strong TPL signals come only from the aggregate nanoparticles and nanodimers, and we only saw very small TPL signals for isolated nanorods.

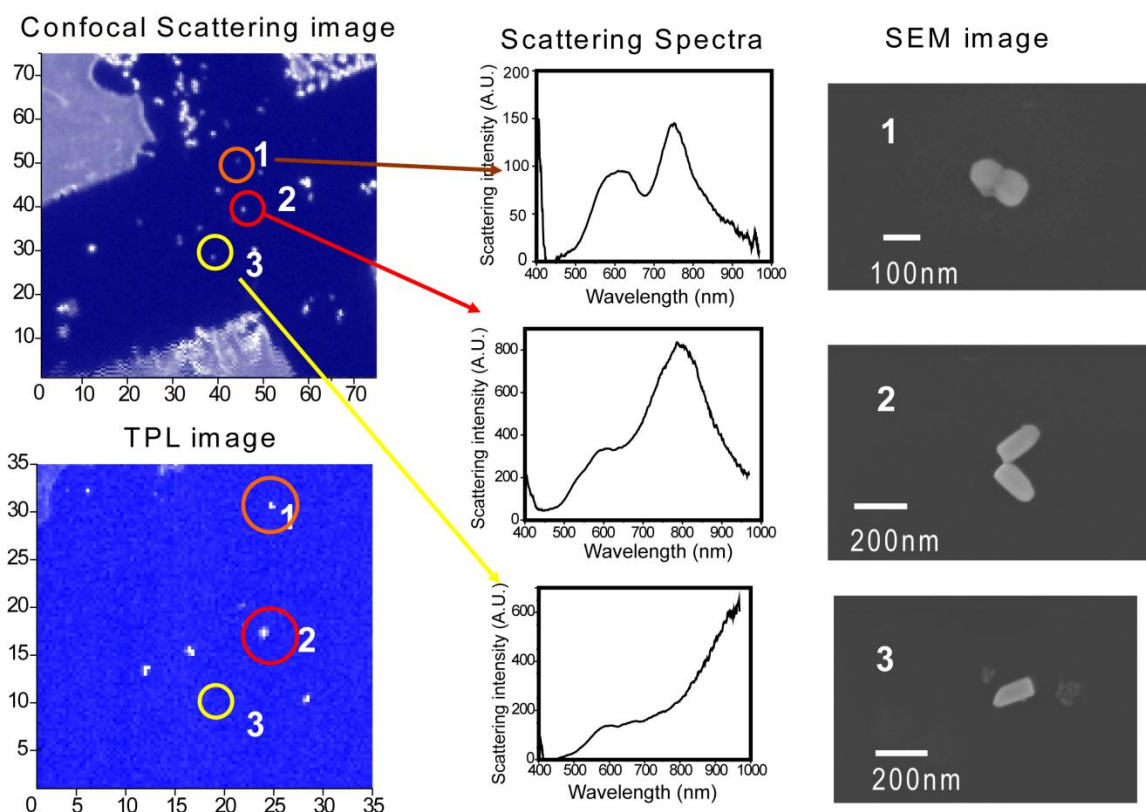


Figure 3.13: The correlation experiment of scattering image, TPL image, scattering spectra and corresponding SEM image

There were two main problems for experiments with bare metal nanoparticles; particle aggregation and photodamage. Metal nanoparticles had strong tendency to aggregate together due to their high aspect ratio. Among our previous experiments, the percentage to find single nano-dimer was less than 10 % and others were aggregates. Another problem was photodamage. From our observation, we found bare metal particles change the plasmon structure and the brightness of samples even in low power of laser ($\sim 50 \mu\text{W}$).

We attempted to solve these two problems by coating the particles with $>10 \text{ nm}$ thick silica layer. The silica surface of the metal nanoparticles had lower surface tension than that of the bare metal surface to improve the dispersion inside hydrophilic solutions.

Van Duyne group also demonstrated that a thin oxide layer can increase photo-stability significantly⁹³. We also found that > 10 nm thick silica layer greatly increase the photodamage threshold to allow us to perform advanced nonlinear optics study. Figure 3.14 shows the comparison of photodamage between coated and uncoated metal nanoparticles. The silica-coated nanorods can resist the power as high as $300 \mu\text{W}$, but the uncoated nanoparticles changed the shape and intensity after three times scanning.

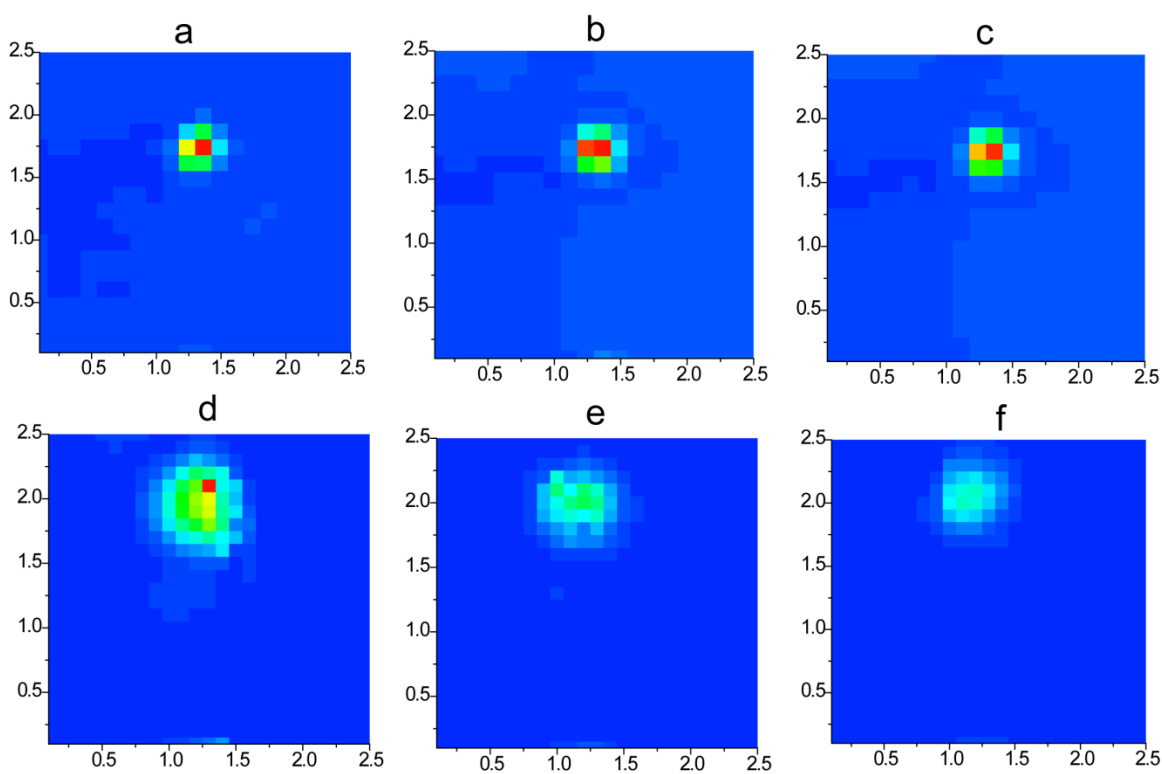


Figure 3.14: The photostability test of coated (a-c) and uncoated (d-f) nanoparticles, both panels are scan for three times under $300 \mu\text{W}$, the color scale for top panel is from 0 to 1.1, and the bottom panel is from 0 to 0.8.

TPL and FWM experiments were also performed with the silica-coated metal nanorods. The results are shown in Figure 3.15 and Figure 3.16. We performed the power dependence experiments, and we plot logarithm of power versus logarithm of TPL

signals to confirm that the signals are from two-photon process. The slope of the linear fitting in Figure 3.15(b) was 2, and it confirmed the source of emission was from two photon process. We also scanned different the excitation wavelength to obtain a TPL excitation spectrum (Figure 3.15 (c)). Although our laser has limited bandwidth, we can still see that the excitation spectrum had maximum peak at 760 nm when we excited our sample for every 10 nm excitation.

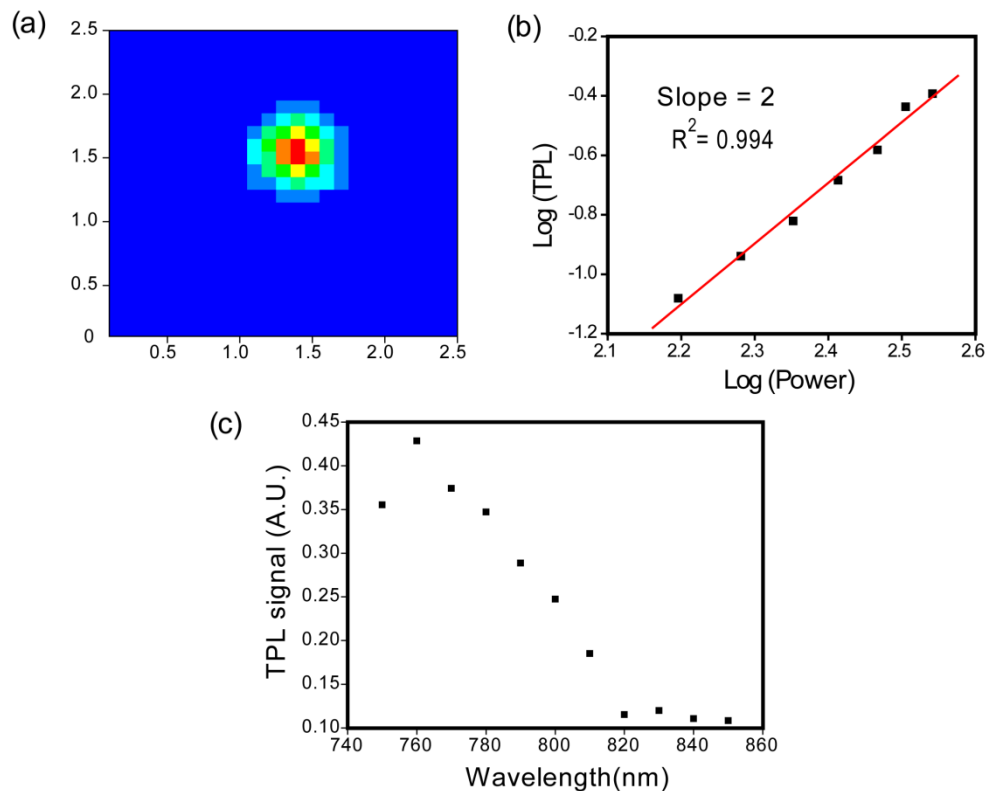


Figure 3.15: (a) TPL scanning image (Excitation wavelength is 790nm) (b) The dependence of TPL signal and power (c) TPL excitation spectra

We also obtained FWM spectrum from these samples. Figure 3.16 shows the TPL and FWM images and corresponding TPL and FWM spectra at similar conditions. For TPL, 790 nm was chosen as excitation wavelength, and a broad weak emission is

observed around 600-700 nm, similar to other groups' results^{74c, 94}. For FWM, 760nm (λ_1, ω_1), and 845nm (λ_2, ω_2) were chosen to excite samples, and emission wavelength of 690 nm (λ, ω) further confirmed the FWM process by $\omega = 2\omega_1 - \omega_2$ and $\omega \propto 1/\lambda$ relations. Another point needed to address here is the relative intensity of FWM was much stronger than one of TPL (Figure 3.16 (c) and (d)).

Although we successfully built a correlation system of morphology, scattering spectra, and nonlinear optical techniques and were able to obtain some reasonable results, the issues of photodamage and sample fabrication still hindered us to investigate further in our nanorod system. The silica coating alleviated the photodamage problem, but we found different silica coating particles had very different responses under short pulse laser excitation. Some coating sample helped, but some of them cannot resist short pulse laser excitation as bare nanodimer sample. This serious inconsistency of photodamage threshold leads us to find other system to study field enhancement effect.

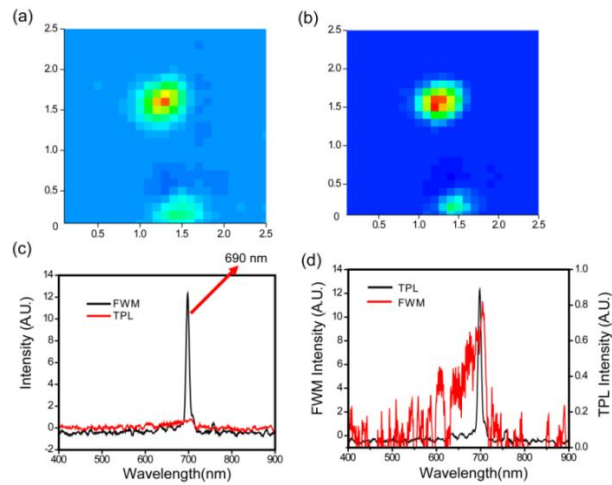


Figure 3.16: (a) TPL scanning image (Excitation wavelength is 790nm) (b) FWM scanning image (Excitation wavelength is 760nm and 845nm) (c) The spectra of TPL (red line) and FWM (black line) under similar condition (d) Normalized TPL and FWM spectra

3.3.2 Nanopyramids

3.3.2.1 *Connected and non-connected pyramids*

After searching literatures, we chose pyramid as next target to study the correlation between local field enhancement and SERS. There were three reasons for us to choose pyramid system. First, the synthesis procedures were simple, and size can be mainly controlled by the mask size. Here, instead of expensive e-beam or photolithography, we used polystyrene beads as our mask. Different sizes of polystyrene beads are commercially available, and sizes of pyramids were controlled by the diameter of polystyrene beads. Another important point is that pyramids can endure higher laser power excitation than nanogap structure which we discussed in previous section. We measured laser power in front of the objective, and according to our results, the highest power our pyramid system can endure is 1.0 mW without any further damage. To ensure free of photodamage, we used 0.8 mW of laser power to excite our samples through all our TPL experiments. For nanorod, the maximum power we can use is 0.3-0.4 mW, smaller than the one we used in pyramid system. We believed the reason why pyramids can endure higher power than nanorod and nanodimer was due to the substrate. The substrate of pyramid was composed of gold film which had better thermal conduction than glass substrate in nanorod experiments. The heat generated by high electric field enhancement mechanism can be removed faster by gold film substrate. Also, stronger TPL signals were expected because of high power usage in the pyramid system. Finally, pyramids have smooth surfaces, and it eliminate the possibility of local field enhancement by rough surfaces^{89a}.

In the beginning of this pyramid project, we had to examine the feasibility and find conditions for each fabrication steps. We first synthesize pyramids by homogeneously dispersing large area monolayer of polystyrene beads. The fabrication

procedures were summarized in experimental sections. Figure 3.17 represents the SEM images of different synthesis steps of pyramids made from 1 μm polystyrene beads. Figure 3.17(a) shows the inverted pyramid pits on a silicon wafer after KOH etching at 65 degree Celsius. Figure 3.17(b) is pyramid pits deposited thin gold film, and Figure 3.17(c) is the pyramid sample after being attached adhesive layer (Krazy glue) and then stripped off.

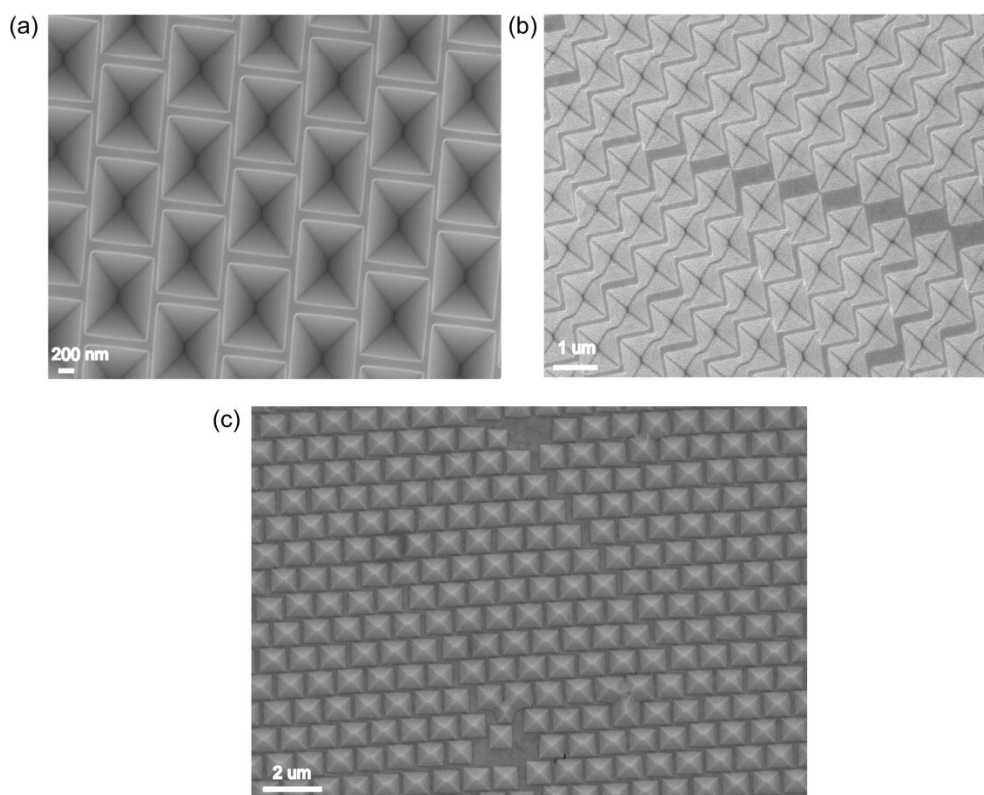


Figure 3.17: SEM images for different fabrication stages (a) silicon wafer after KOH etching. One can clearly see inverse pyramid pits. (b) KOH etched pyramid pits deposited thin gold layer. 50 nm gold layers are used here. (c) Stripped gold pyramid.

After we successfully synthesized the pyramids, we performed SERS experiments in our system. Benzenethiol is widely used as a probe molecule in SERS experiment

because benzenethiol can form homogeneous self-assembled monolayer on gold surface⁷². Also, benzenethiol doesn't have electronic resonance at our laser excitation wavelength and lacks of electron donating functional group such as amine group. We do not need to consider both electronic resonance effect and charge transfer effect in our system⁷⁰. The molecular structure of Benzenethiol, and our typical SERS spectrum shows in Figure 3.18. Three peaks were around 1000 cm^{-1} are 996, 1022 and 1071 cm^{-1} and consistent with literature values⁹⁵. Few wavenumber differences from Van Duyne group's results⁷² might result from different excitation wavelength. For later experiments, we integrated 1071 cm^{-1} peak (represented by * in Figure 3.18) to obtain SERS images. According to literature, 1071 cm^{-1} is assigned as in-plane ring bending + C-S bond stretching modes⁹⁵.

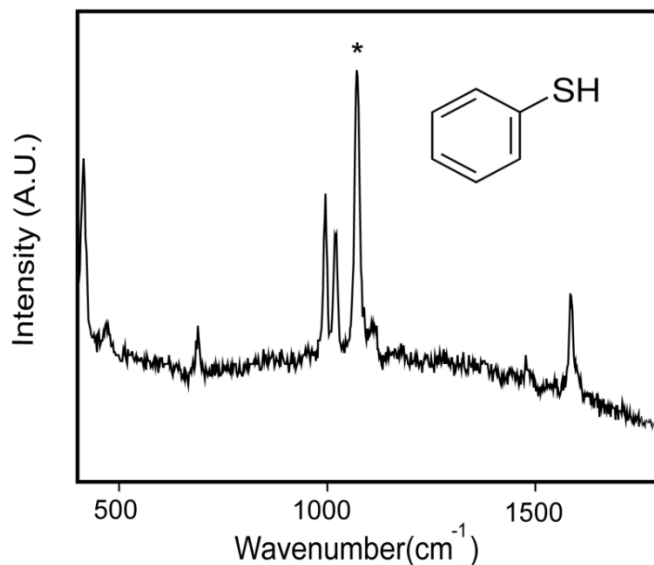


Figure 3.18: Benzenethiol SERS spectrum. Three peak positions around 1000 cm^{-1} are 996, 1022 and 1071 cm^{-1} respectively. * represents the peak integrated to acquire SERS image

We incubated our samples in 1 mM benzenethiol of methanol solution for 3 hrs, rinsed with copious amount of methanol, and then conducted SERS measurements. According to literature, 3 hrs were enough to form a good quality self-assembled monolayer⁷², and we maintained this condition for following experiments. First, we needed to examine SERS signals of our samples. We scanned large area (50-100 μm), and our step size was 1-2 μm to acquire SERS images of our pyramid samples. We found that we can acquire observable SERS signals and images by 100 ms acquisition time for each step. After SERS images were obtained, we used SEM to characterize morphology of our samples. Figure 3.19 shows the SERS images of three samples and their SEM images. Several observations can be addressed from these results. First, as other groups have observed, SERS signals were very inhomogeneous for every sample⁹⁰. Some spots had much higher signals. One of our goals was to find the relation between structure and high SERS signal spots. We also found that SERS signals altered significantly with different areas. For example, in Figure 3.19(a), I roughly circled the area with the high average SERS signals in red and corresponding pyramid area in SEM image. Note that it was very difficult to label same area in both figures due to measurements by different instruments. Here, we just labeled them qualitatively to conveniently illustrate the preliminary observation. In the red circle, the SERS signals were observable but very inhomogeneous. Some spots really had very huge SERS signals. SERS signals were invisible out of the red circle under our conditions although we still see pyramids over there. Similar results can be observed with the assistance of red box in Figure 3.19(b) and red circle in Figure 3.19(c).

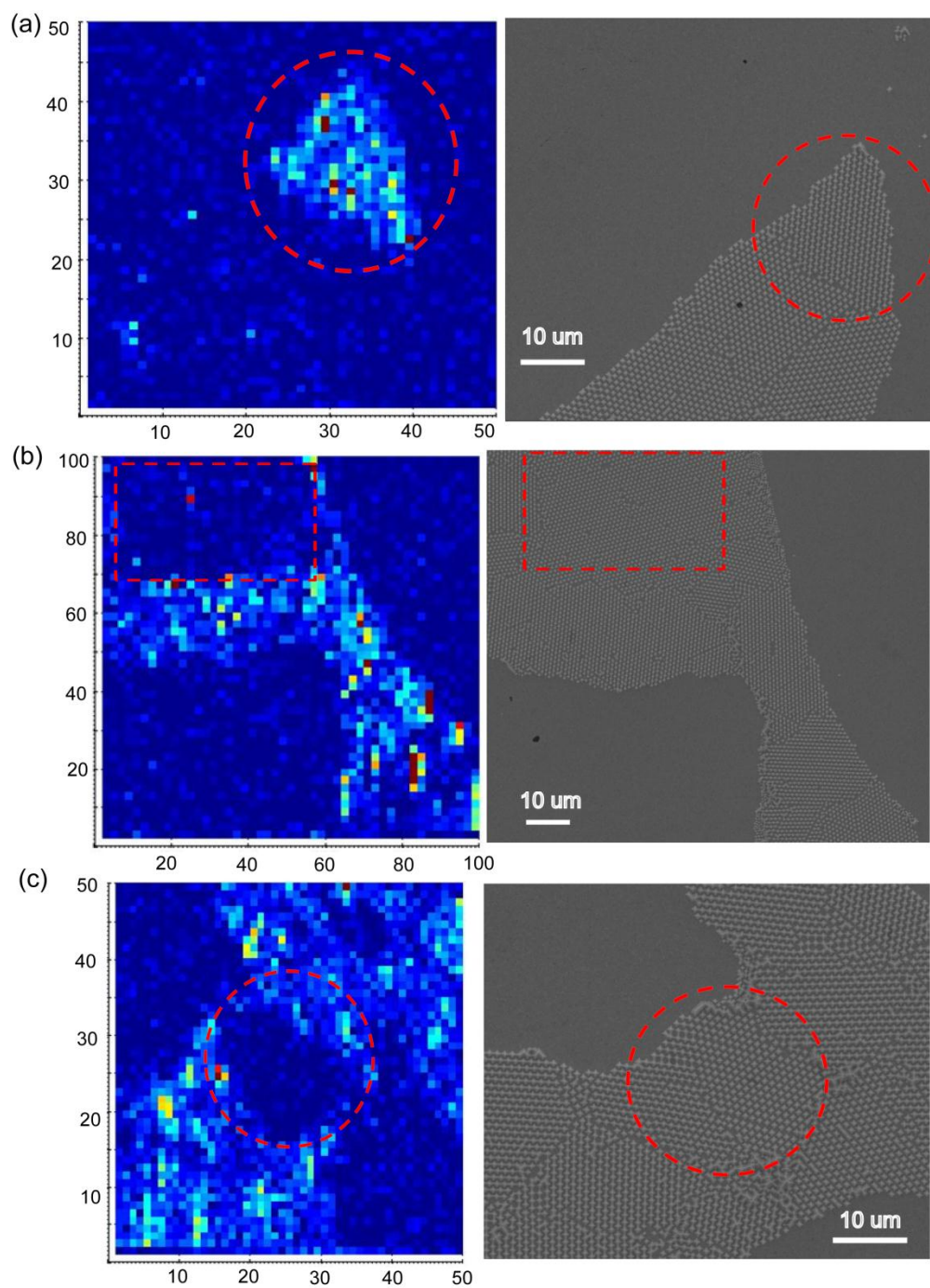


Figure 3.19: Three representative samples of large area pyramids (a)-(c), their SERS images (left panel) and corresponding SEM images (right panel). Note that the center of both SERS and SEM images are not exactly same. The numbers on SERS image axis represent actual scanning distance (μm). The scale of SERS images are same for three samples

After closely examination of our samples by SEM, we found that pyramid structures of both SERS active and inactive areas are different. It is well-known that structures strongly affect to SERS intensity. For the area having many high SERS intensity spots, we found that the pyramids were connected to each other. On the other hand, low SERS signals usually occur on pyramids which do not connect to each other. For convenience, we named the former connected pyramid and the latter isolated pyramids. Figure 3.20(a) and (b) are SEM images of typical connected and isolated pyramids respectively for both structures. The origin of both structures was from the relative position of the polystyrene self-assembled monolayer and crystal axis direction of silicon wafers. Wet KOH etching on a (100) silicon wafer is isotropic and forms inversed pyramid pits. Hence, the pyramid structures were determined by both polystyrene beads direction and etching direction. It was different from other researchers' work. In their work, they can control separation distance of polystyrene beads, so their pyramids were far from each other enough to assure pyramids were isolated to each other^{88a, 89b}.

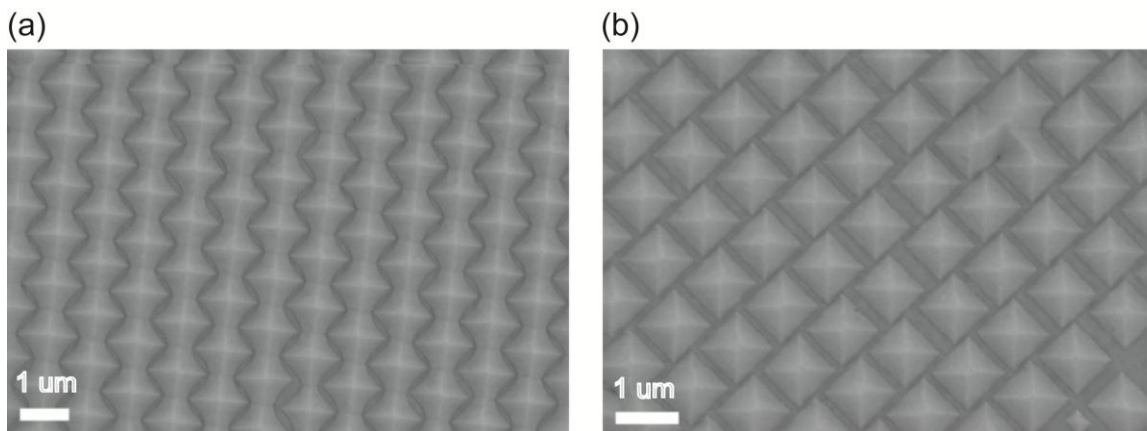


Figure 3.20: SEM images of two different types of pyramids: (a) connected pyramids (b) isolated pyramids

To explain the experimental results and relation between signal intensity and morphology, more experiments were required. First, instead of studying large area pyramid aggregation, we used spin coating technique to synthesize small pyramid aggregates. Figure 3.21 shows three examples of small pyramid aggregates. Left panel of Figure 3.21 is SERS image with 0.1 sec acquisition time for each step, and right panel is corresponding SEM images. The color scales for all three SERS images are from 0 to 500. One can see the shape of SERS images roughly corresponded to shape of pyramid aggregates in SEM images. In other words, only pyramid area had SERS signals, and there is no observable contribution from flat gold film. In addition, SERS signals were still very inhomogeneous in sample area although pyramids resembled each other except connection issue under such SEM magnification. From SEM images, we found the pyramid surface was smooth, so we can eliminate the surface roughness factor causing high SERS signals. According to literature, the pyramid pits surfaces of such etched silicon wafer can achieve atomic smoothness⁸⁹.

From Figure 3.21, it was still obscure to ascribe high SERS signals to connected pyramids. We attempted to overlap both SERS images and SEM images by image processing program (Photoshop), but again, it was very difficult to match exact position of both images. There were several reasons why it was difficult to obtain an exact matching position. First, the SERS signals were very inhomogeneous and hard to define a clear boundary between SERS region and non-SERS region. For example, the boundary of SERS images in Figure 3.21(b) and (c) were vague and difficult to define. Although long acquisition time can obtain more signals from boundary, it also increases the signals of hot-spots and made processing of the images difficult. Another issue was different scale definition between our system and SEM. The other reason was resolution and our resolution is $\sim 1.5\text{-}2\ \mu\text{m}$ because we used air objective with NA 0.75. Water immerse

objective was not appropriate in our experiment because long time immersion of water easily detached our sample from glass substrate. In Figure 3.21(a), the boundary was much more obvious than (b) and (c). When we attempted to match both images, we find that a small image shift and differences of magnification cause different fitting results. Hot spots may shift from the intersection between pyramids to the tip of pyramid, or from connected area to isolated area. If we use smaller aggregation, then clear boundary was difficult to obtain. Therefore, we needed some techniques to clearly label the relative position between pyramid boundary and SERS position. Only after developing such technique, we just can exactly compare both SEM images and SERS images.

Figure 3.22 shows SERS image and SEM image of another sample. Surprisingly, the sample had very high SERS signals although all pyramids are isolated. Also, as mentioned earlier, no obvious boundary of the image was observed in Figure 3.22, and only two very bright spots are observed. It provides another example that exact correlation is very difficult for such sample only showing few bright SERS spots.

So far, we can safely conclude that pyramids synthesized from self-assembled polystyrene beads had higher possibility to have strong SERS signals. In other words, we assume if pyramids are separated far enough, SERS signals should decrease significantly. Figure 3.23 shows three SERS and SEM images of isolated samples whose separation was controlled by oxygen plasma etching on polystyrene beads. The SEM images showed that we can successfully synthesize completely isolated pyramids by oxygen plasma processes. Some pyramids had irregular edges because the plasma etched polystyrene beads were not perfect spheres especially with long etching time. Here, our acquisition time of SERS images for each step was 0.5 second, 5 times longer than Figure 3.21 and 3.22. The color scale is 0-200, about twice smaller than Figure 3.21 and 3.22. In Figure 3.23, the SERS intensity of isolated pyramids was still inhomogeneous and is

much weaker than the closed packing pyramids. We can estimate these isolated pyramids had average 5-10 times weaker signals than closed packing pyramids. In addition, there is still no obvious SERS boundary among these samples and difficult to find the origin of SERS signals. Although we suspect irregular edge may produce high SERS signals, not all irregular samples show SERS signals. We can only conclude that close packing pyramids showed high possibilities to have high SERS intensity. If we separated pyramids far enough, the possibility of pyramids coupling decreases, and we only can observe weaker and fewer SERS hot-spots.

Until now, we only consider SERS effects. Next, we started to incorporate multiphoton effects. We first performed power dependence experiments to examine what multiphoton process involves although we already examined it in nanorod part. Figure 3.24 shows two examples of power dependence experiments. We plotted logarithm of power versus logarithm of emission and found slopes were 1.81 and 1.96 respectively, very close to 2. In addition, we placed a suitable short pass filter in front of PMT to eliminate the possibility of second harmonic generation and linear scattering effect. Hence, we confirmed this multiphoton process is two-photon luminescence (TPL). Figure 3.25 shows the SERS, TPL image and corresponding SEM images of small aggregate pyramid samples. The polarization of both laser source were adjusted to match with each other before the experiments, and the polarization was along x axis. The TPL excitation wavelength is 770 nm for all samples. One can see TPL image has black holes at pyramid position because TPL were from both pyramids and substrate of gold film and the 3-D structures of pyramids cause such black hole. Therefore, the black hole can indicate us the location of TPL signals.

Our results showed that TPL signals all were located on the junction between two pyramids, the edge of pyramids, the connection part of two connected pyramids, and

the broken corners of pyramids. SERS signals were located more randomly than TPL signals. Next, we examined the correlation between TPL and SERS at same pyramid array. Although we can conduct optical experiments at same small pyramid aggregated arrays, the detailed correlations between TPL, SERS and SEM images were still difficult. Thus far, our results showed that TPL signals were not totally correlated with SERS signals. Some TPL and SERS signals were at similar position, but some other TPL and SERS signals did not correlate at all. The results are not consistent with theory even though the polarizations of both lasers were same.

One possible reason why connected pyramids have high chances to have strong SERS signals is because the gap between pyramids and gold substrates. In literature, the gap between samples and substrates is reported to have strong SERS signals^{61b, 73a}. However, it is difficult to control gap size and its orientation, and it is well-known that SERS signals are strongly correlated with both gap size and polarization direction^{6, 9, 51b}. Therefore, we believe the issue of gap size and orientation control made our result difficult to explain and have some exceptions.

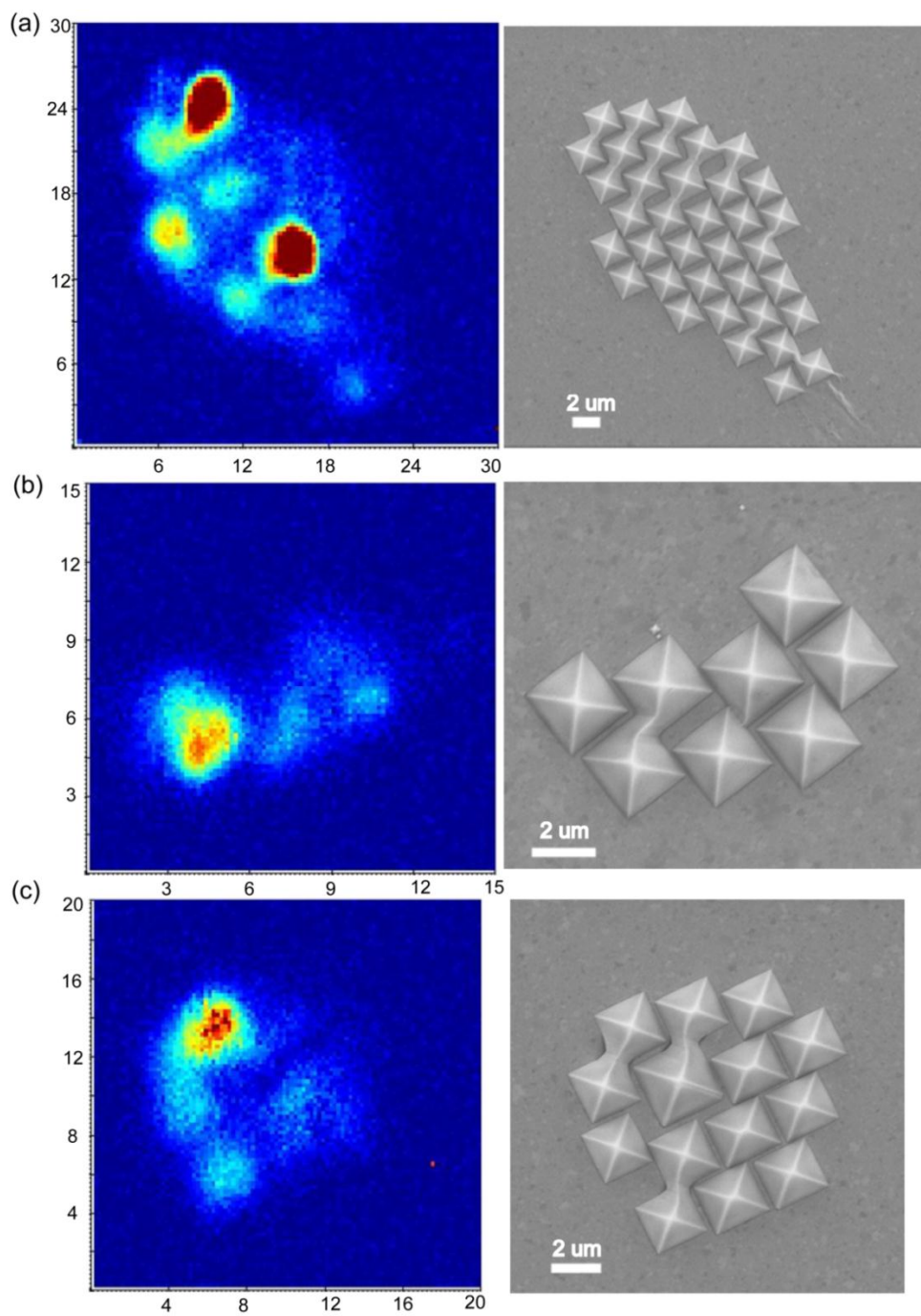


Figure 3.21: (a)-(c): Three examples of small aggregate pyramids, SERS images (left panel) and corresponding SEM images (right panel). The scales of SERS images are from 0 to 500 and same for all three samples. The acquisition time is 0.1 sec for each step. The numbers on SERS image axis represent actual scanning length (μm).

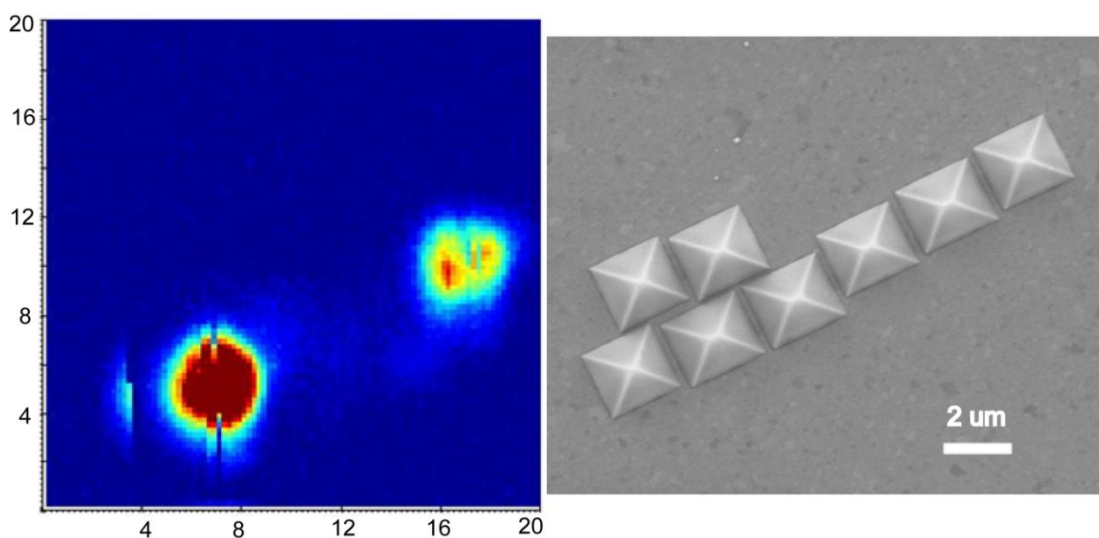


Figure 3.22: The example of small aggregate non-connected pyramids with high SERS signals. Left panel is SERS image and right panel is SEM image.

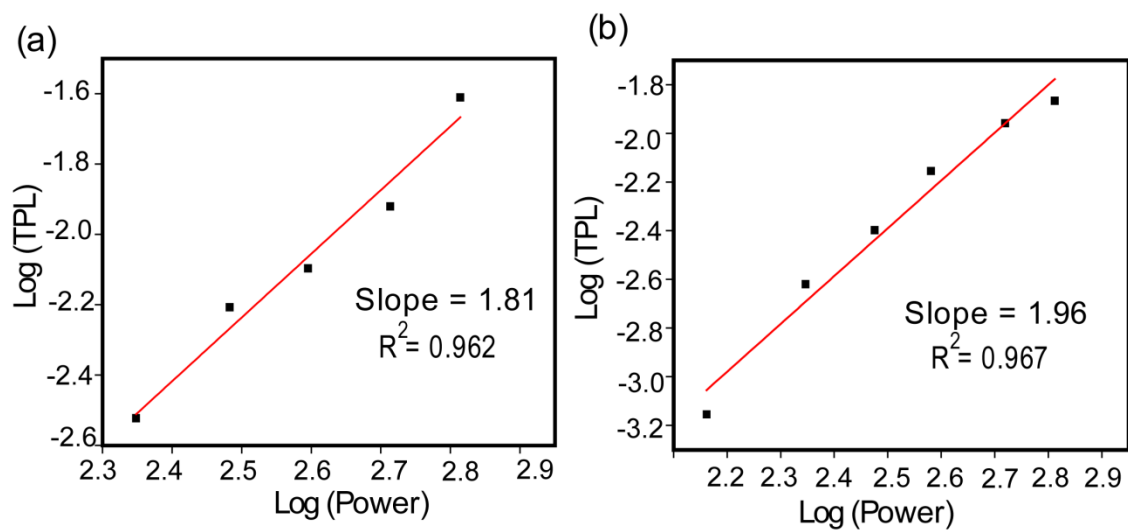


Figure 3.23: (a) and (b): The power dependence plots of two examples. The slopes are 1.81 and 1.96 respectively.

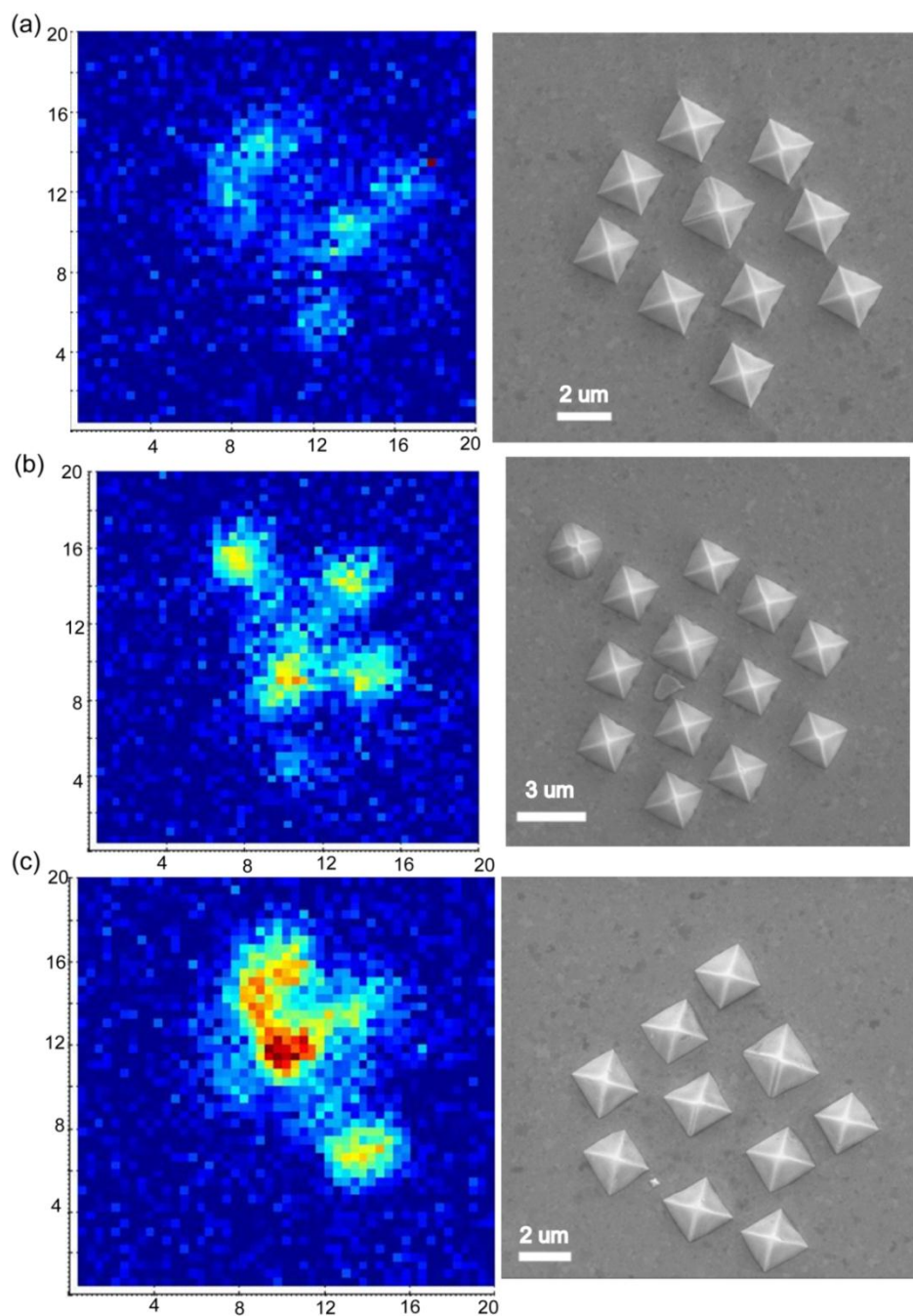
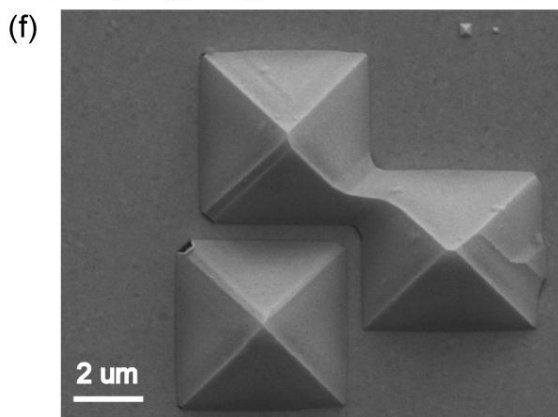
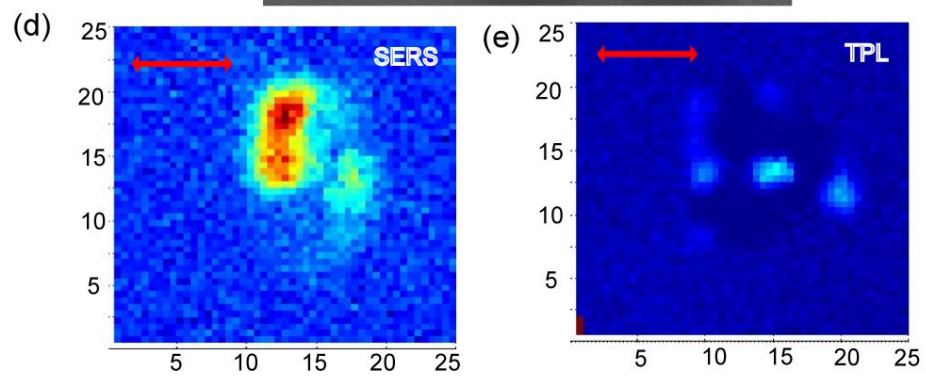
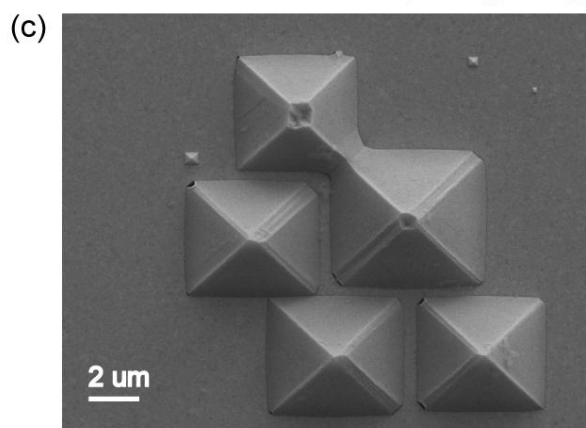
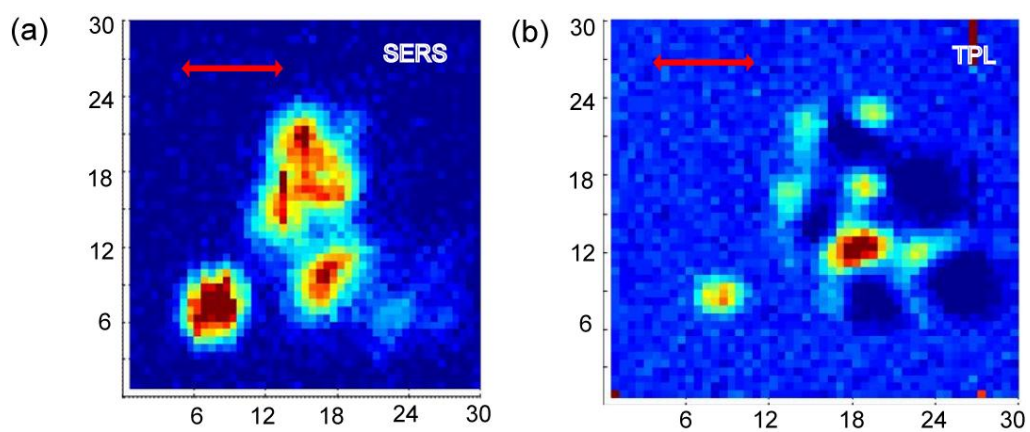


Figure 3.24: (a)-(c): Three examples of small aggregate pyramids fabricated by oxygen plasma processes, Pyramids are well separated from each other. Left panel is SERS images and right panel is SEM images. The scale of SERS images are from 0 to 200 and same for all three samples. The acquisition time is 0.5 sec for each step.



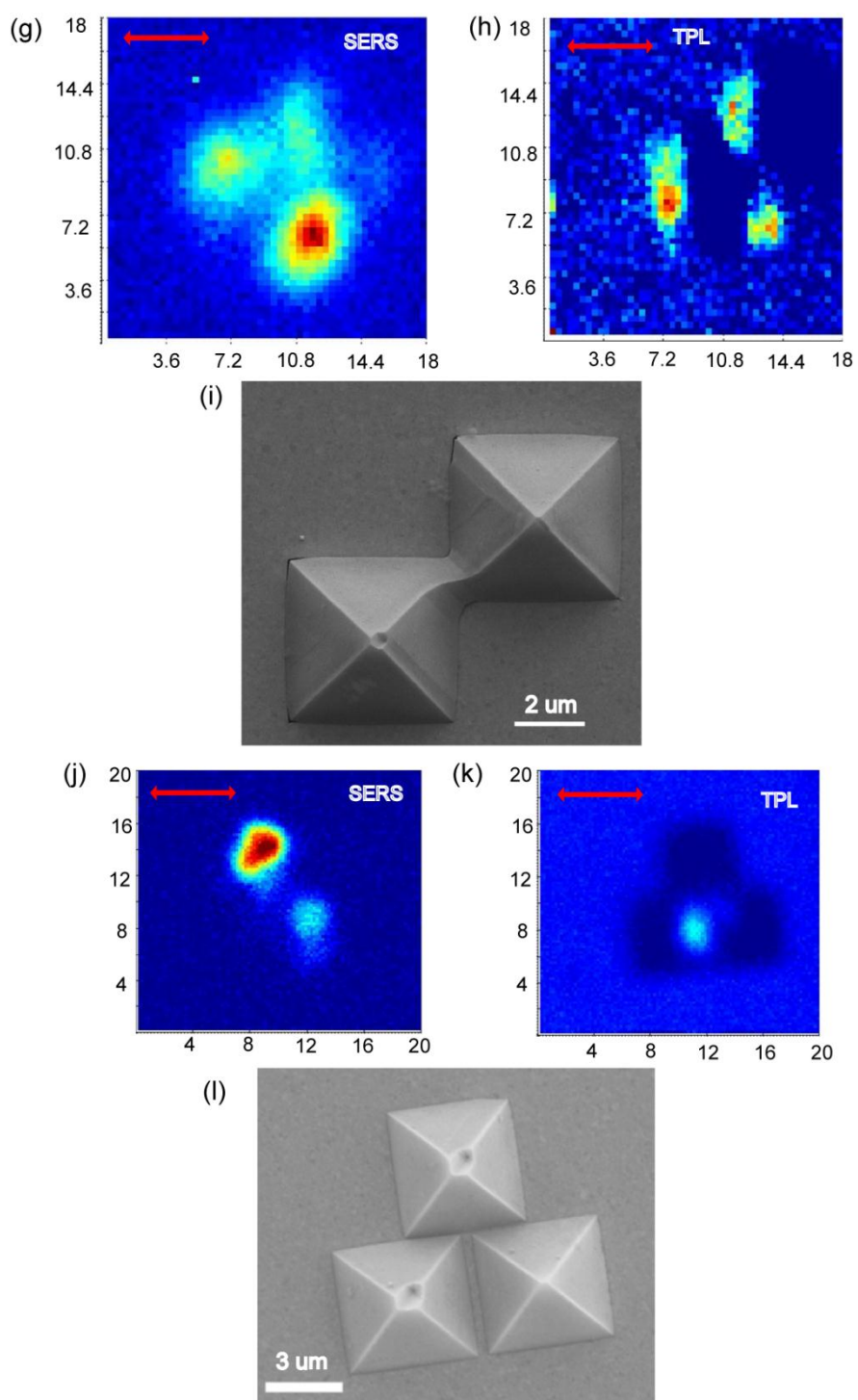


Figure 3.25: Four examples of small aggregate pyramids Their SERS, TPL and SEM images. (a)-(c) sample 1, (d)-(f) sample2, (g)-(i) sample 3 and (j)-(l) sample 4. The red arrows are polarization direction of both lasers.

3.3.2.2 Regular and shaped pyramids

From the previous discussion, we realized that small aggregates of pyramids were still too complicated to find the relation between high SERS signals spots and structures. Also, we knew that single pyramid has weak SERS signals if the structure of the pyramid is perfect. Therefore, we considered whether we can artificially create and control a SERS hot spot structure on perfect a gold pyramid. Fortunately, we can achieve this goal by modification of pyramid synthetic procedures.

For regular pyramid (old method), after we etch wafer by wet KOH etching, we removed the protecting Cr layer by commercial etchant and then deposited gold film. We found that we can switch the fabrication sequence to obtain different shapes of pyramids, and we called them “shaped pyramids.” For shaped pyramids, after we etched wafer by KOH etching, we first deposit desired thickness of gold layers instead of etching Cr layer and then peel pyramids off by template stripping method, same as regular pyramids. The remained Cr layer behaves as mask of gold layer deposition. We found that the adhesive force between Cr and silicon wafer was larger than the one between Cr and gold layer, so we can apply template stripping method. We also conducted the element analysis experiments by EDX technique (Energy-dispersive X-ray spectroscopy) on shaped pyramid surface. Figure 3.26 is our EDX result, and there is no observable Cr on shaped pyramid surface. Hence, we can synthesize shaped pyramids and investigate their SERS and TPL properties.

Moreover, we knew that it was difficult to indicate the position of SERS signals on pyramid structures. We solved this problem by referring TPL experiments. We found that if we used laser to scan the pyramid by laser and collected scattering light, we can identify the boundary of pyramids due to three-dimensional structure of pyramids. Figure 3.27 shows this idea. Figure 3.27(a) is the scattering image acquired from scanning single

shaped pyramid sample, and the circle in the middle was the boundary of the shaped pyramid. Then, we can scan same area to obtain SERS images (Figure 3.27(b)). After obtaining both images, we can overlap them to see where the SERS signals were located (Figure 3.27(c)). In Figure 3.27(c), we can tell that SERS signals were located at bottom left corner, upper left corner and right middle of pyramid boundary. With this new technique, we were able to identify SERS positions.

Figure 3.28 are SEM images of different angle views of regular pyramids (left panel) and shaped pyramids (right panel). From (a) to (c) are top view, tilt 25 degree, and tilt 70 degree respectively. We originally thought we can create artificial gaps between pyramid edges and substrate (gold film), and these gaps can produce huge field enhancement and had great SERS signals. In Figure 3.28 right panel, one can see we indeed successfully create gaps between edges of shaped pyramids and substrates. However, different from what we expected, we also created V-groove shape gap at four corners of pyramids. Figure 3.28(c) clearly shows both V-groove gaps at two corners.

After we successfully synthesized regular and shaped pyramids, we conducted systematic SERS and TPL experiments and morphology investigation by SEM. First, for the purpose of comparison, we examined SERS and TPL on regular single pyramids, and we found both SERS and TPL signals were extremely low as before (data not shown). Next, we investigated SERS and TPL on single shaped pyramid samples and morphology by SEM. Figure 3.29-3.36 are four examples of our experiment results. SERS signals (Figure 3.29, 31, 33, 35 left-hand side) and TPL signals (Figure 3.29, 31, 33, 35 right-hand side) were mainly located at corner of pyramids which are different from what we expected. For convenience, we labeled four corners of pyramid as 1 to 4 on all SERS, TPL and corresponding SEM images. We also changed the polarization (red arrows in SERS and TPL images) of both incident lasers to study the polarization effects.

Several observations can be addressed here. Strong TPL spots were always located at four corners of pyramids, and TPL behaved more regularly than SERS for all our experiment results. TPL also had clear polarization dependence definition. The polarization across the V groove generated strong TPL signals, and TPL signals are depressed if polarization was perpendicular to the V groove. However, SERS signals were more random and unpredictable. Besides corners, SERS signals also can be found at the gap between edge of pyramids and substrates. Moreover, unlike TPL signals, SERS signals were invisible in some corners. SERS signals also have polarization dependence effect, but the effect is less clear than TPL. From SEM images, it is difficult for us to distinguish the structural differences among all four V groove corners. The angle of V groove is also one possible factor to affect SERS and TPL. The edge of grooves of some samples had rough surface, and such roughness may lead to have high SERS and TPL signals^{6, 13}. However, we cannot clearly indicate the amount of roughness and how roughness affects SERS and TPL signals. Some grooves resembled each other from SEM images, and they had similar TPL responses, but totally different SERS signals. In addition, some SERS signals positions can correlate with TPL signals position, but some of them are independent from each other. It was still very difficult for us to make conclusion of correlation among SERS, TPL and morphology.

So far, our results showed some correlations between TPL and SERS. We thought the first possible reason might be because self-assembled layer of benzenethiol was not covered all the surfaces of pyramids, so such uncovered area showed invisible SERS signals. However, because TPL is related to gold properties, inhomogeneous benzenethiol SAM layers do not affect TPL intensity. This may be one reason why TPL and SERS have low correlation. Another possible reason was what Lupton and his coworker suggested⁸⁴. They performed a systematic investigation of both excitation and

emission parts of SERS and TPL properties including excitation polarization, polarization anisotropy, lifetime, and power dependence experiments. They suggested that both TPL and SERS had similar excitation pathway, and power and incident laser polarization dependence can explain similar excitation pathway. This was consistent with the plasmonic theory in section 3.1. However, from emission anisotropy and lifetime study, they suggested that both SERS and TPL had different relaxation pathways. The different pathways made both processes had low correlations. We believed it also can explain our results.

Another possible reason is the coupling among LSPR and local field at the frequency of incident light and emission light. For SERS, the enhancement factor is strongly related to the local electric field at both frequencies of incident light and emission light (Equation 3.22), and TPL is also similar to SERS. In our case, we used 785 nm lasers to excite our samples to obtain both SERS and TPL signals. For SERS, we acquired 1071 cm^{-1} peak of benzenethiol, so the emission wavelength is 857 nm. Therefore, we have to consider LSPR of our samples at both 785 nm and 857 nm for SERS. For TPL, we know the wavelengths of TPL are smaller than 785 nm from our experimental results (Figure 3.16) and literature results^{74c, 94}. Also, we place suitable filters to collect the TPL emission between 608 nm to 710 nm. Therefore, we have to consider LSPR of our samples at both 785 nm and the region between 608 nm and 710 nm for TPL. Hence, if our samples have different LSPR behaviors around 850 nm and between 600 nm to 710 nm, we may have different responses of SERS and TPL. Unfortunately, we did not measure reflection spectra of our samples, so we cannot compare LSPR behavior at different regions. However, we can compare reflection spectra of V-groove shapes and inverse pyramid pits whose structures are similar to our samples in literatures⁹¹ to explain our results qualitatively. In their results, the reflection

spectra are different at both sides of 785 nm, so LSPR are different at both sides of 785 nm as well. Because we did not measure reflection spectra of our samples, the reflection spectra in the literatures just provide a possible explanation to illustrate our results. In fact, we know that LSPR is very sensitive to the structure of samples, and we cannot find reflection spectra of structures exactly same as ours in literature. The reflection spectra in literature⁹¹ were measure the periodic structures and their size are smaller than ours. Therefore, we still need to measure reflection spectra to explain our results quantitatively.

Lupton's explanation of their results and LSPR coupling idea are two possible reasons to explain why TPL and SERS are not completely correlated in our results. To find the correct explanation, more experiments are needed to be performed to clarify the puzzles.

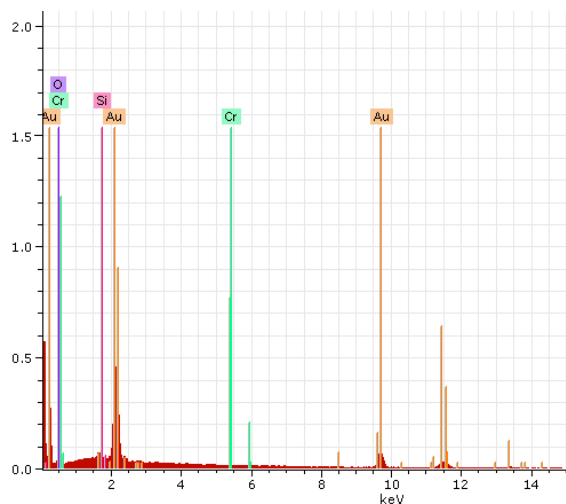


Figure 3.26: EDX spectrum of shaped pyramid after peeling from wafer substrate.

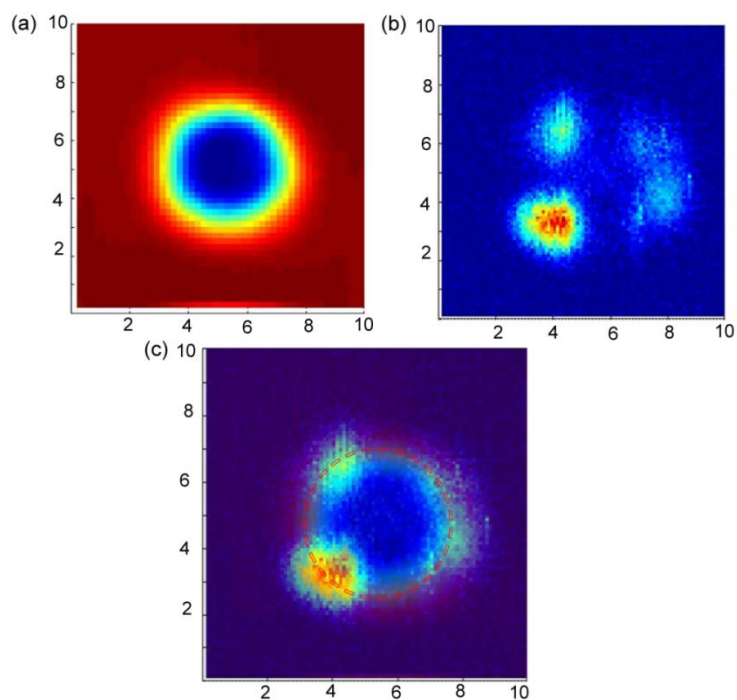


Figure 3.27: (a) Scattering image of single pyramid collected by a photodiode. (b) SERS image in same region of (a). (c) The overlap of (a) and (b), Dash circle line represents the circle in (a). The SERS spots are at bottom left, upper left, and right of circumference.

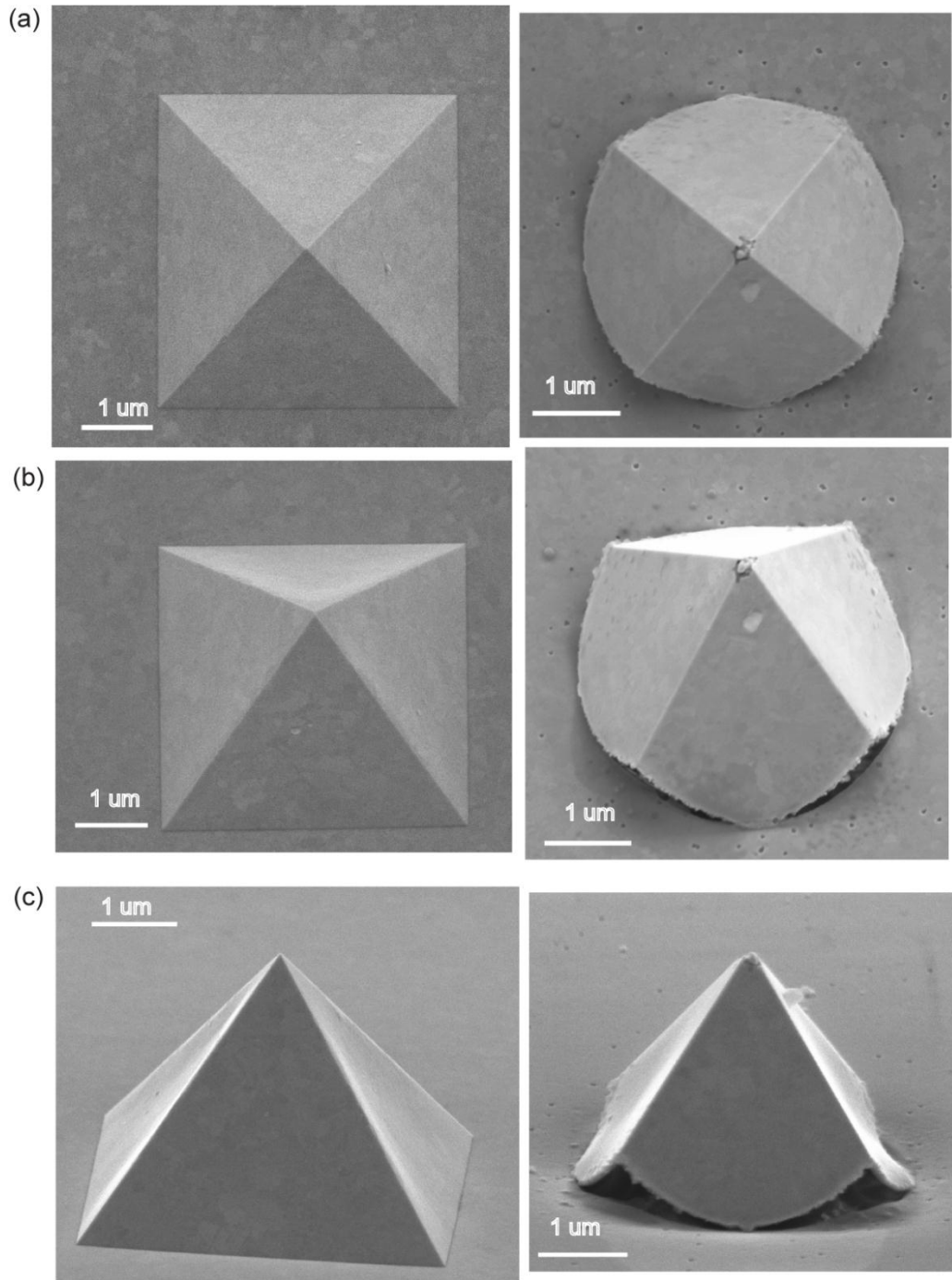


Figure 3.28: The different angle SEM images of regular single pyramid and shaped single pyramid. (a) top view (b) tilt 25 degree (c) tilt 70 degree.

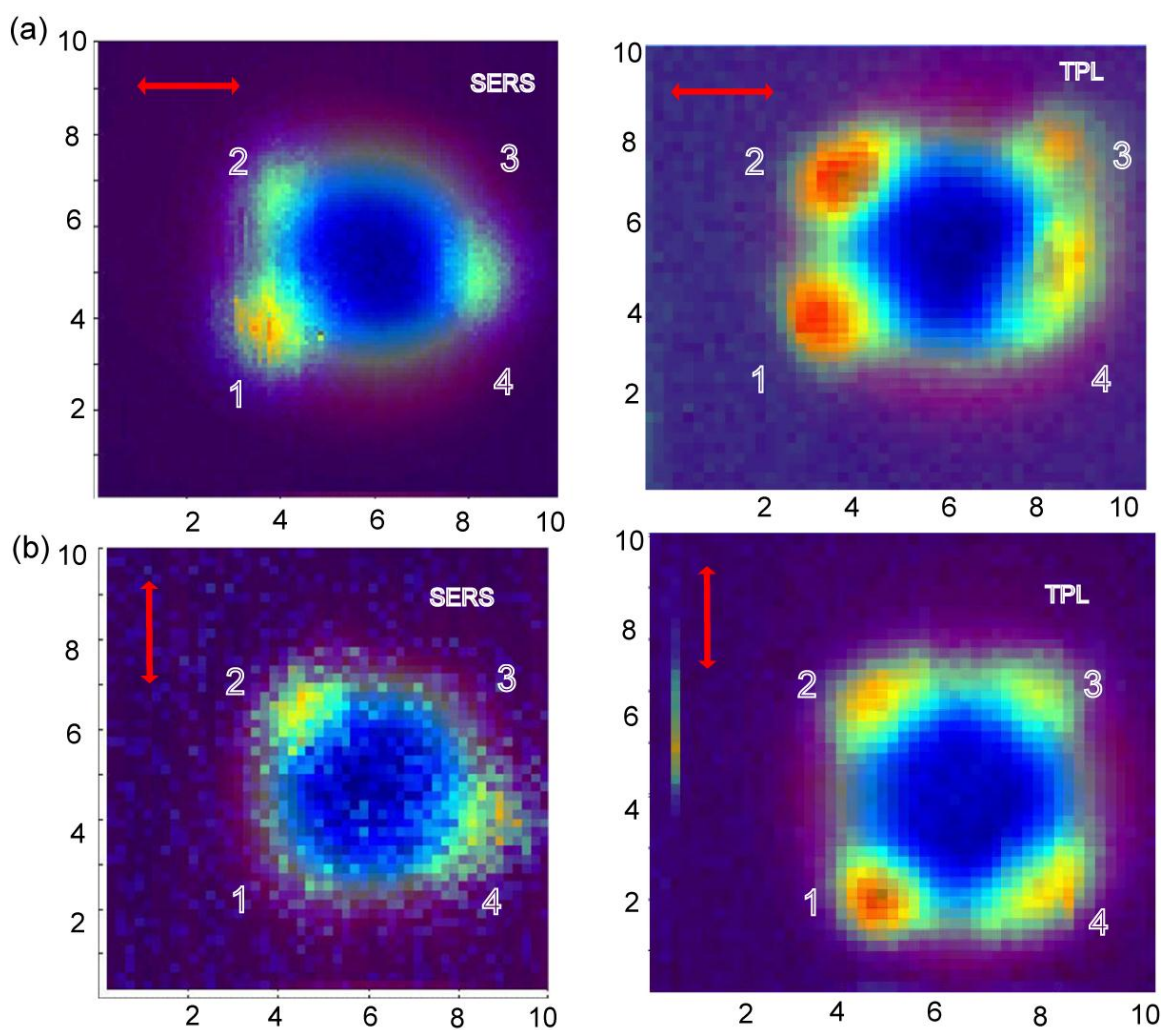


Figure 3.29: SERS images (left panel) and TPL images (right panel) of shaped pyramid of sample 1. Red arrows are polarization directions: (a) polarization is x direction (b) polarization is y direction. The numbers 1-4 on the images represent the four corners of shaped pyramid, same as SEM images in Figure 3.30.

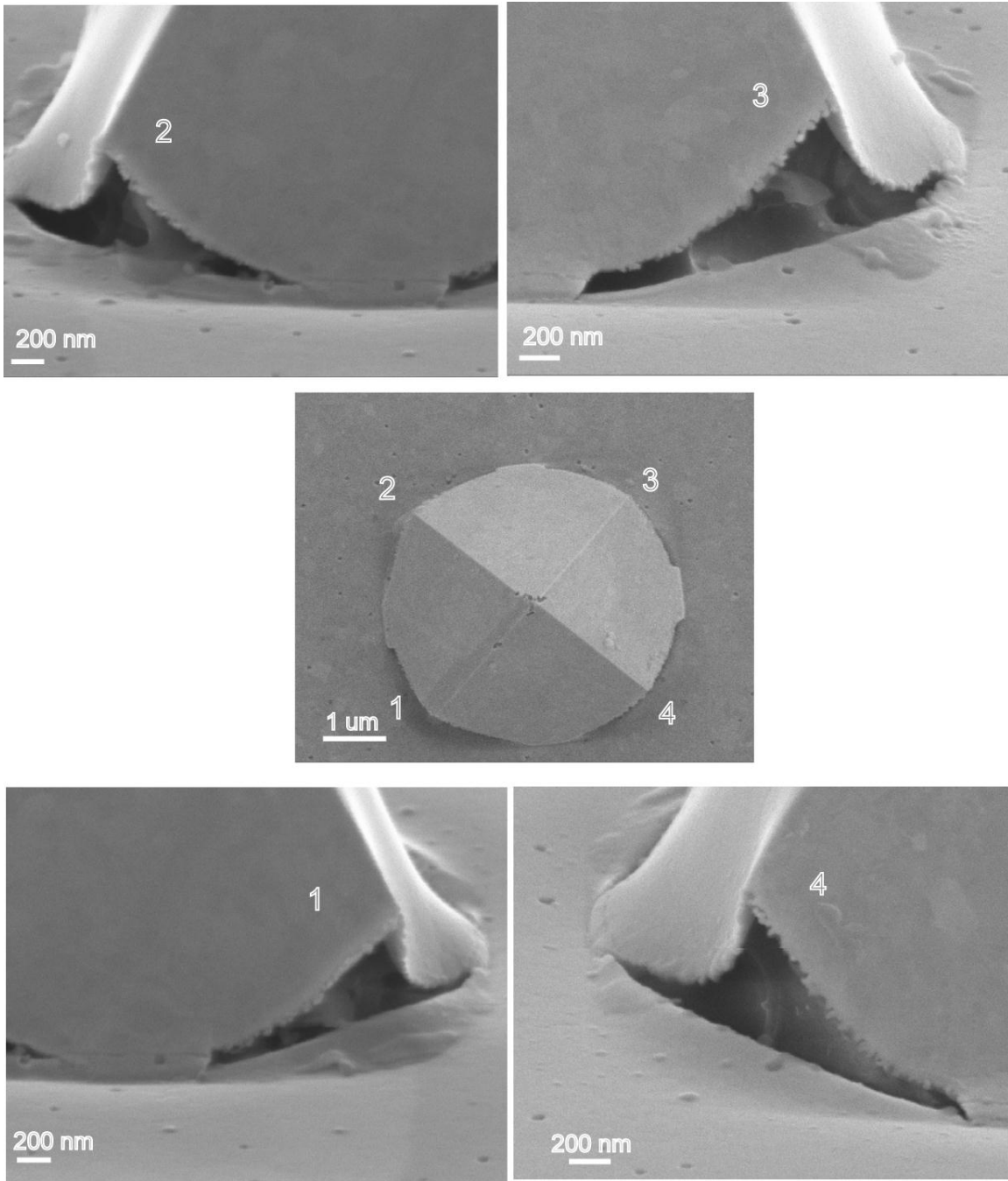


Figure 3.30: SEM images of shaped pyramid of sample 1. The top view is in the middle of the images. The other four are high tilt angle images of four corners labeling with different numbers from 1 to 4.

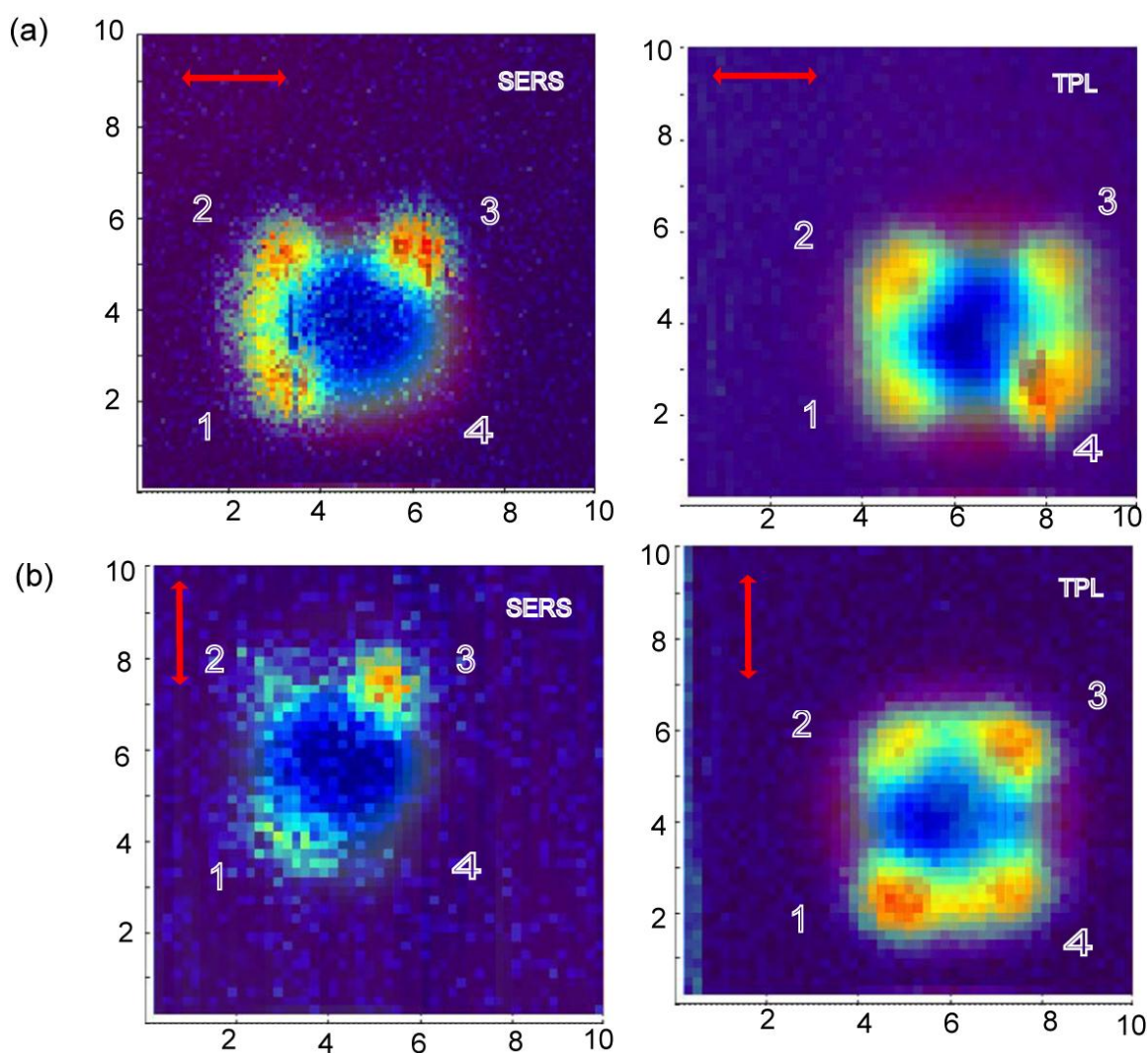


Figure 3.31: SERS images (left panel) and TPL images (right panel) of shaped pyramid of sample 2. Red arrows are polarization directions: (a) polarization is x direction (b) polarization is y direction. The numbers 1-4 on the images represent the four corners of shaped pyramid, same as SEM images in Figure 3.32.

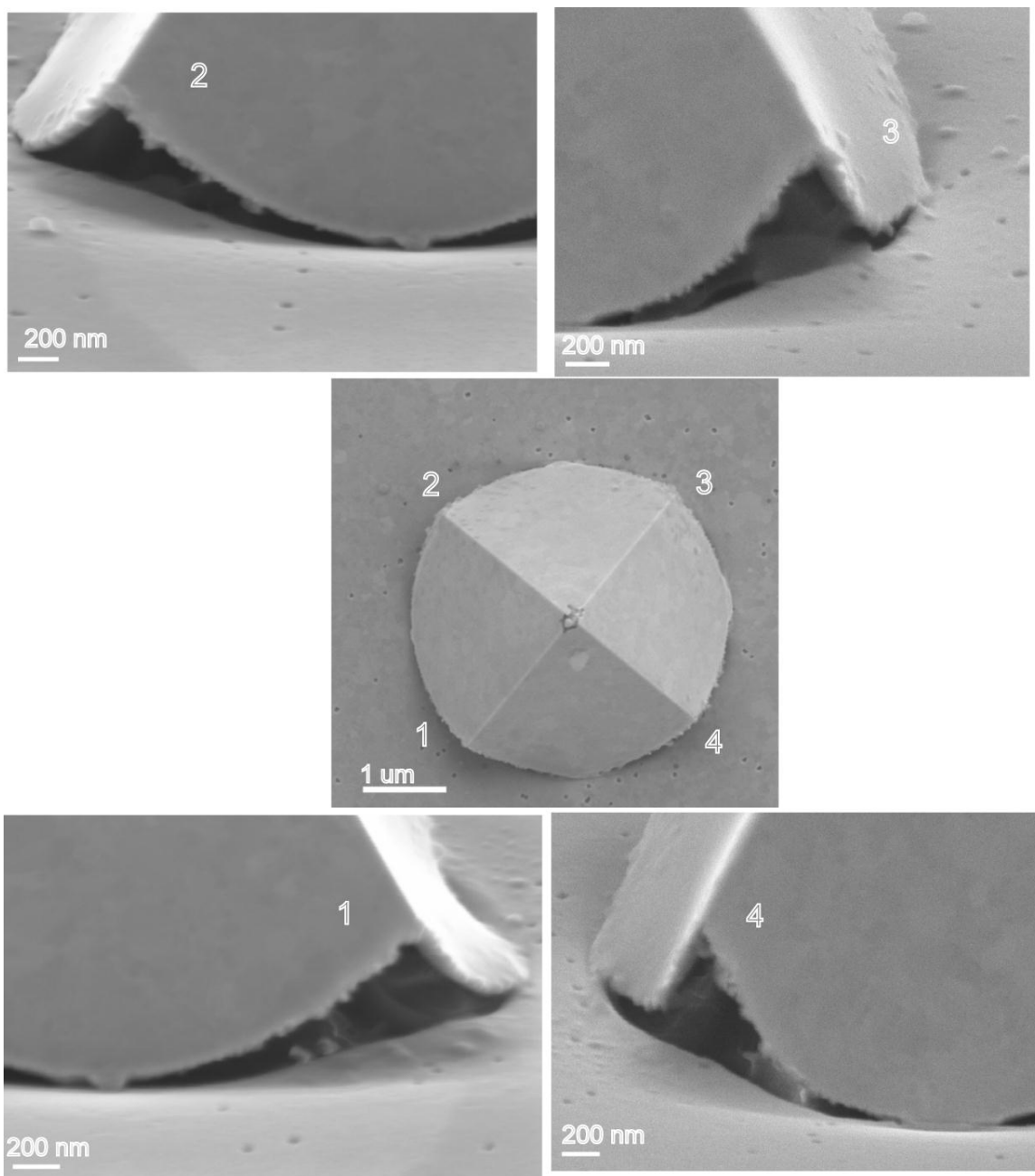


Figure 3.32: SEM images of shaped pyramid of sample 2. The top view is in the middle of the images. The other four are high tilt angle images of four corners labeling with different numbers from 1 to 4.

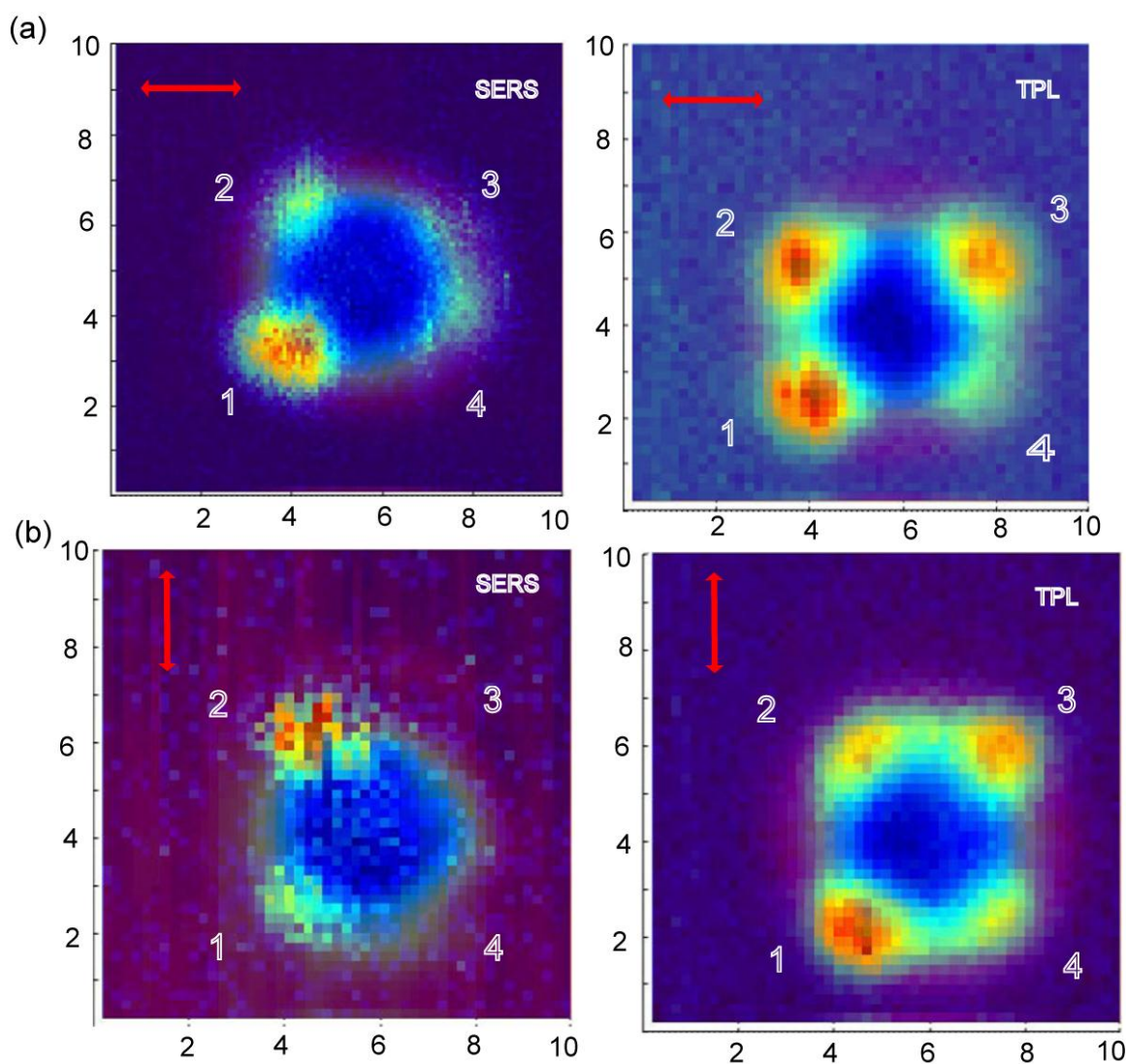


Figure 3.33: SERS images (left panel) and TPL images (right panel) of shaped pyramid of sample 3. Red arrows are polarization directions: (a) polarization is x direction (b) polarization is y direction. The numbers 1-4 on the images represent the four corners of shaped pyramid, same as SEM images in Figure 3.34.

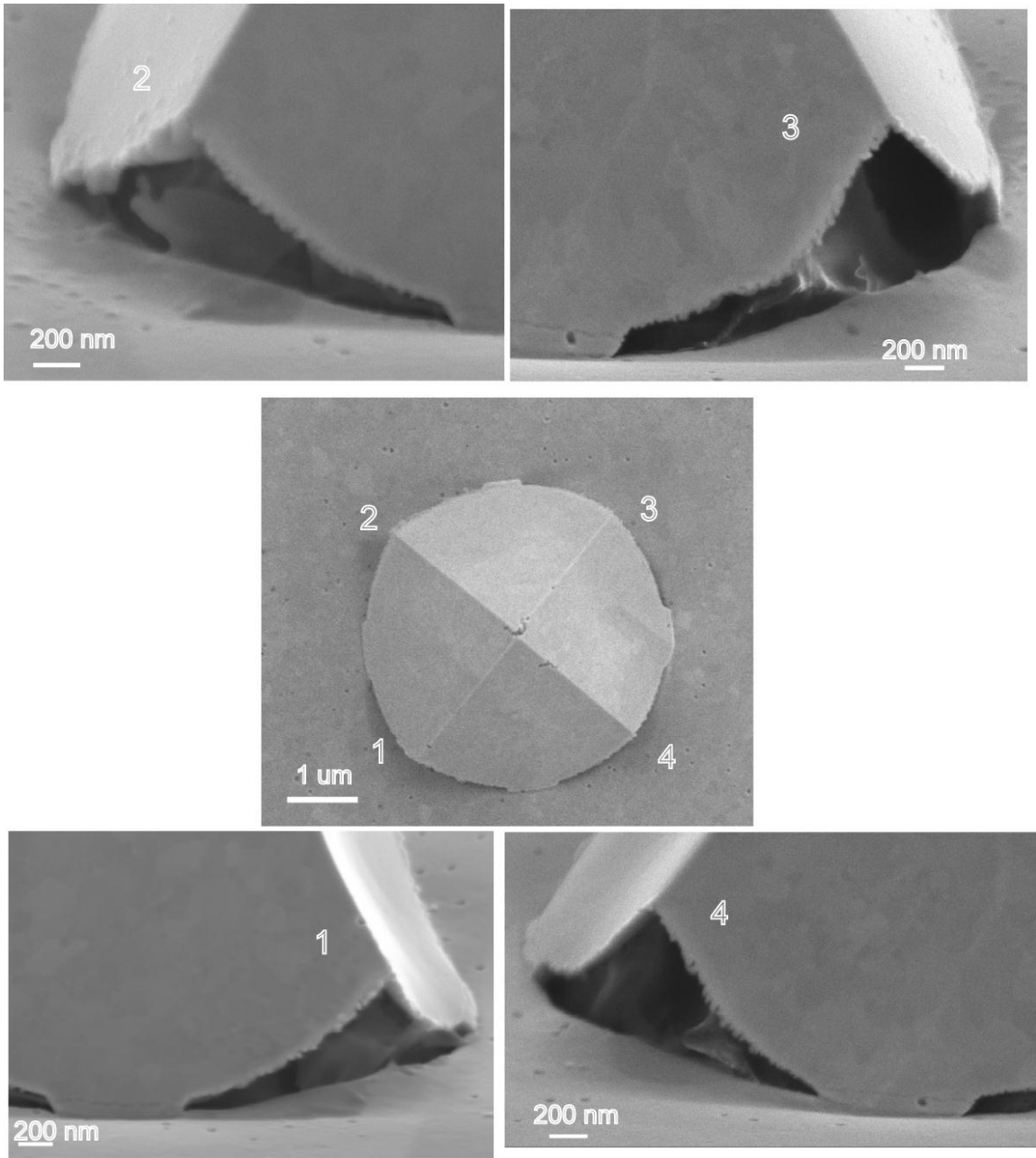


Figure 3.34: SEM images of shaped pyramid of sample 3. The top view is in the middle of the images. The other four are high tilt angle images of four corners labeling with different numbers from 1 to 4.

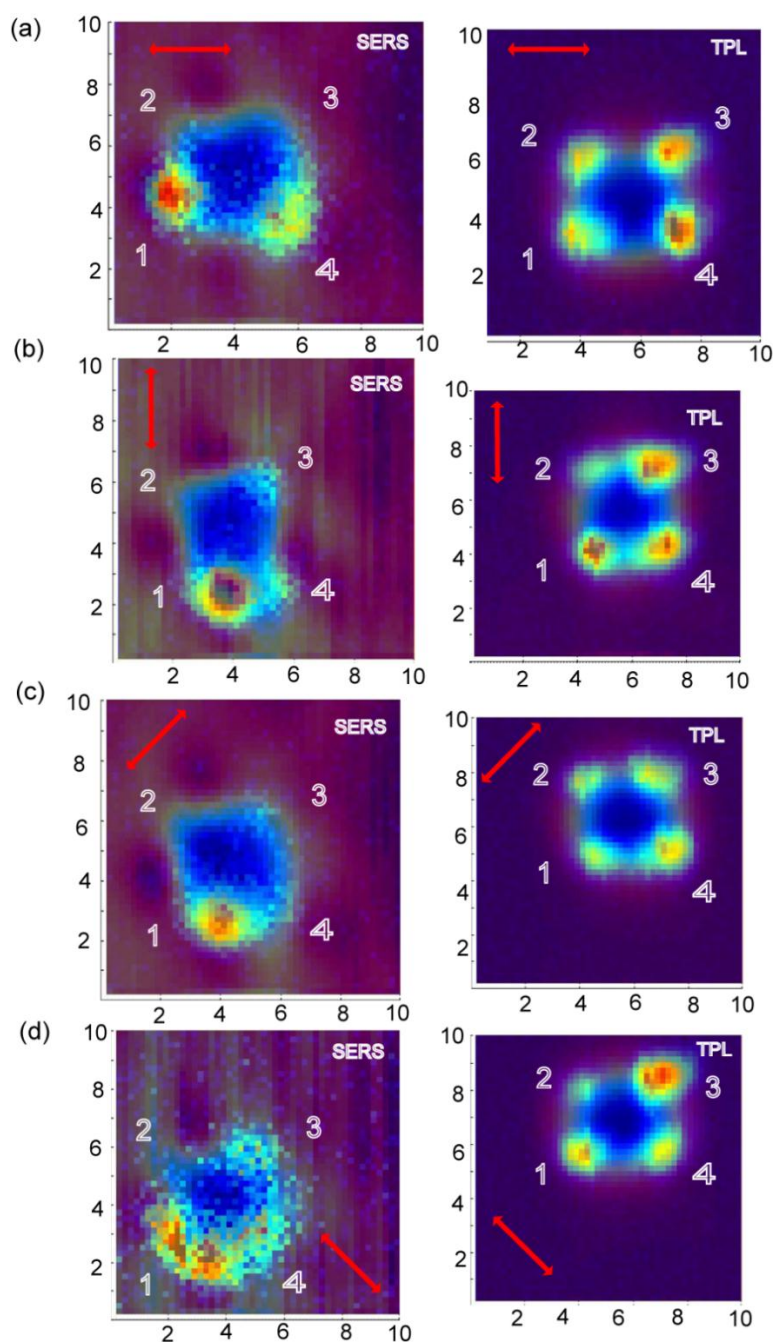


Figure 3.35: SERS images (left panel) and TPL images (right panel) of shaped pyramid of sample 4. Red arrows are polarization directions: (a) polarization is x direction (b) polarization is y direction (c) polarization is +45 degree (d) polarization is -45 degree. The numbers 1-4 on the images represent the four corners of shaped pyramid, same as SEM images in Figure 3.36.

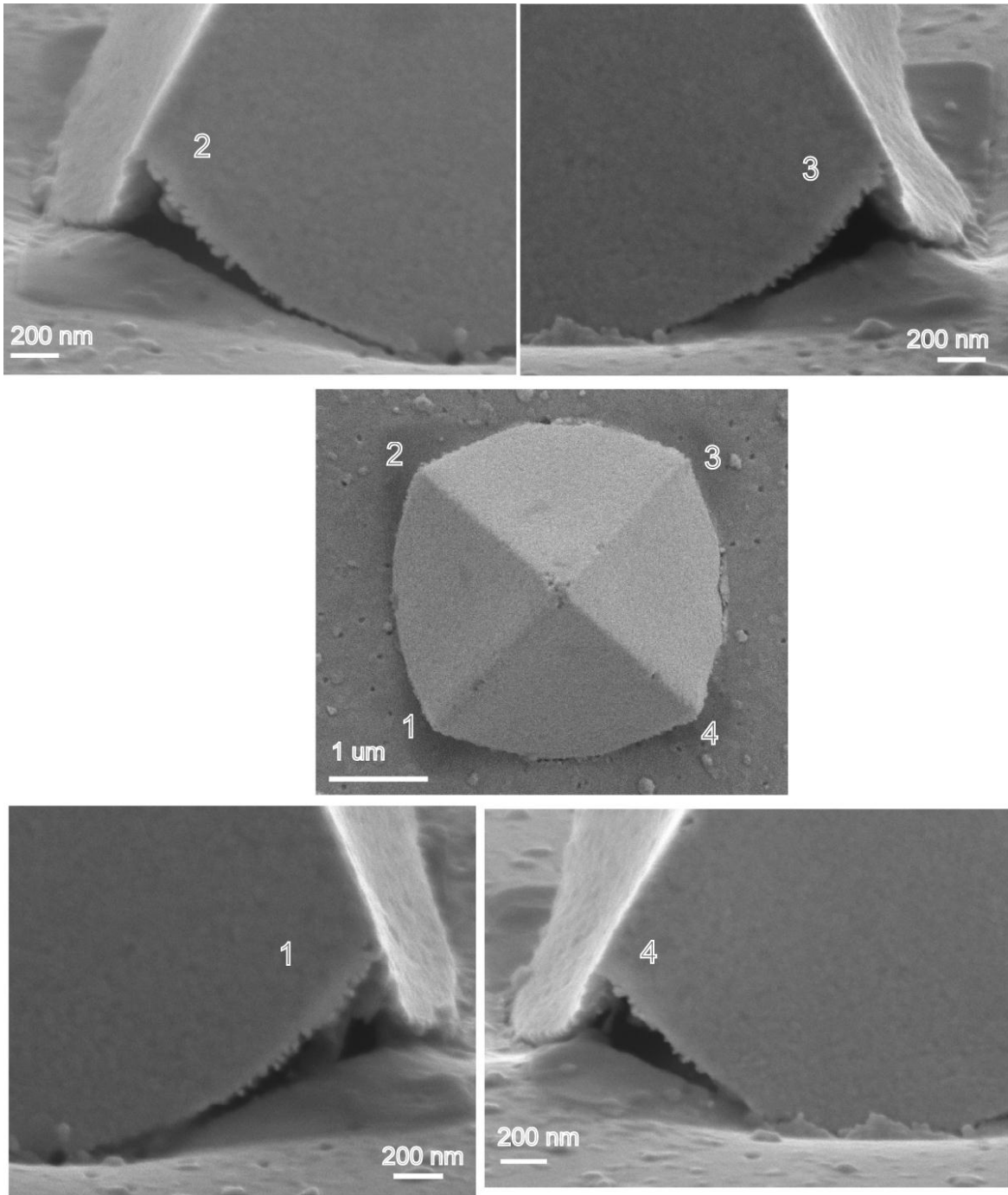


Figure 3.36: SEM images of shaped pyramid of sample 4. The top view is in the middle of the images. The other four are high tilt angle images of four corners labeling with different numbers from 1 to 4.

Chapter 4 Conclusion

In this dissertation, I focused on developing the new techniques to enhance Raman signals and studying the fundamentals of how Raman signals were enhanced. Coherent Raman scattering and surface enhance Raman scattering were two techniques discussed in this dissertation. Some of techniques were developed successfully, but some of fundamental mechanisms were still unclear.

For coherent Raman scattering, I investigated both CARS and SRS processes. I built an optical setup to retrieve Raman-like CARS signals from notorious nonresonant signals based our group's previous work. I also studied the molecular resonant effect in CARS. I used different absorption dyes to conduct CARS experiments, and I found the best detection sensitivity in our system is about 10 μM with the assistance of resonant effect. In SRS, I applied spectral focusing mechanism to build a new SRS setup. Besides spectral focusing mechanism, I also used lock-in amplifier, high frequency modulation, and home-made circuits to achieve acceptable SRS results. I examined the feasibility, spectral resolution, and detection limits of our SRS setup. I found the detection limit of our SRS setup is 10 times over the shot noise limit.

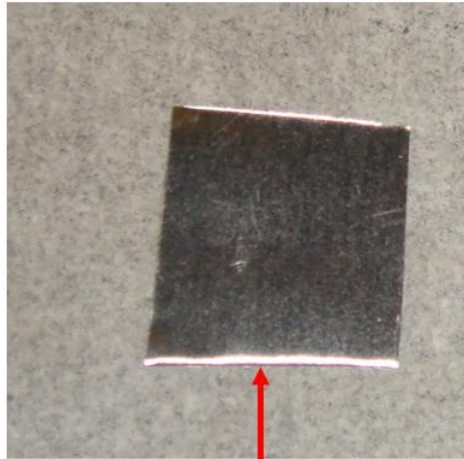
For surface enhanced Raman project, I first synthesized nanorod and nanodimers with gap structures by template methods. I also investigated the field enhancement of these samples by nonlinear optical methods such as TPL. However, the high peak energy pulse laser damaged the samples easily and made the results unpredictable. I solved photodamage problems by choosing gold pyramids as my new system and successfully performed SERS and TPL experiments on pyramids. I synthesized different kinds of pyramids. I found SERS signals were very sensitive with a tiny change of structure and led to random results. On the other hand, TPL is more predictable than SERS. For

aggregate pyramids, TPL was mainly located between junction of pyramids or the edge. For single shaped pyramid, TPL was located at the apexes, whose shape is V-groove. The correlations between SERS and TPL were still unclear so far. According to literature, different relaxation pathways of both SERS and TPL might be one possible reason to explain the vagueness of my results. Another possible reason is the different LSPR responses of our samples at frequencies of incident light and emission light for both SERS and TPL.

Appendix (manual of nanorod synthesis)

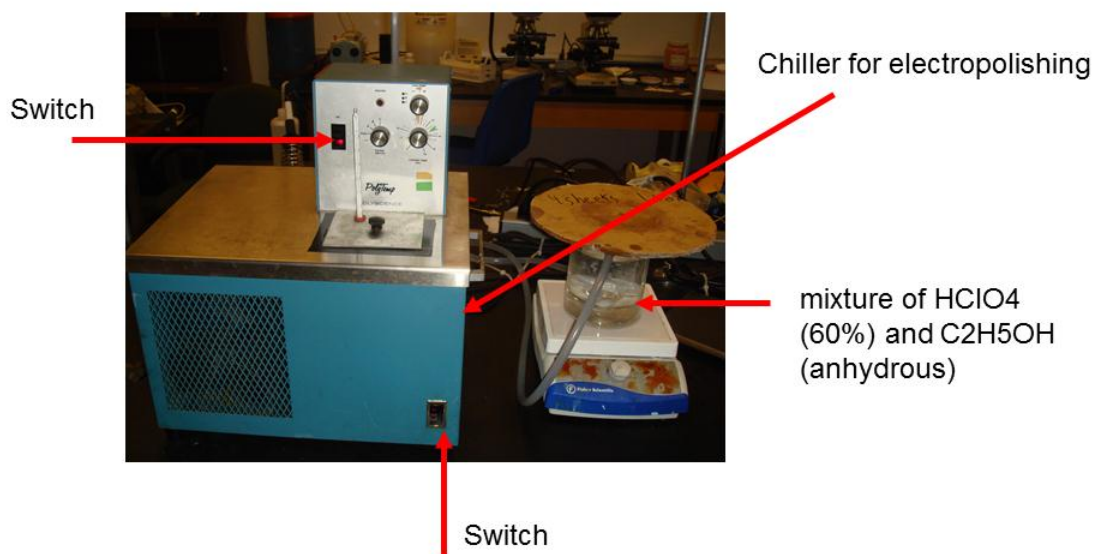
These are procedures of template (AAO) and nanorods synthesis. The original files are powerpoint files. I convert them into files of pictures and paste them below. First of all, these are procedures of AAO synthesis:

Cutting high-purity aluminum foil to 3 cm X 3 cm piece, and then press it to flat.

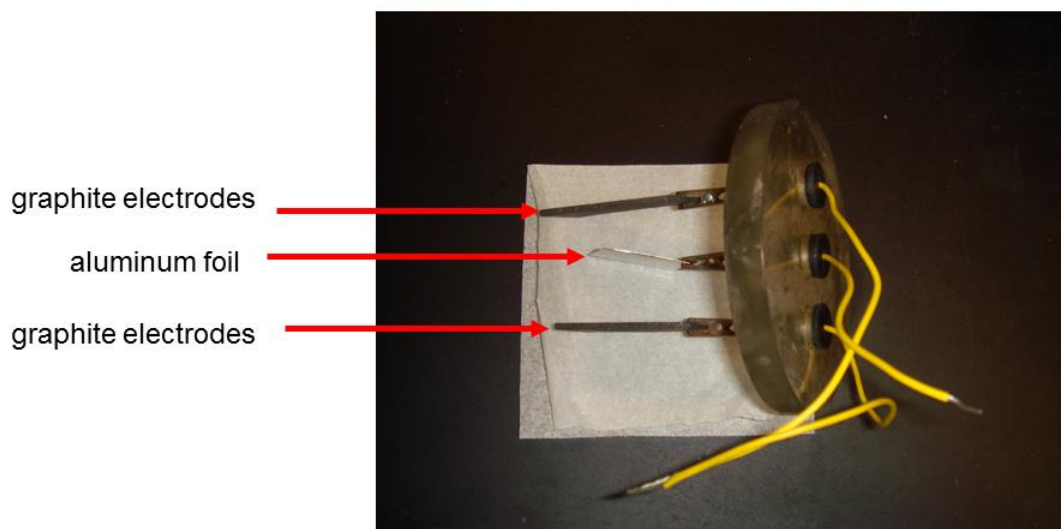


aluminum foil

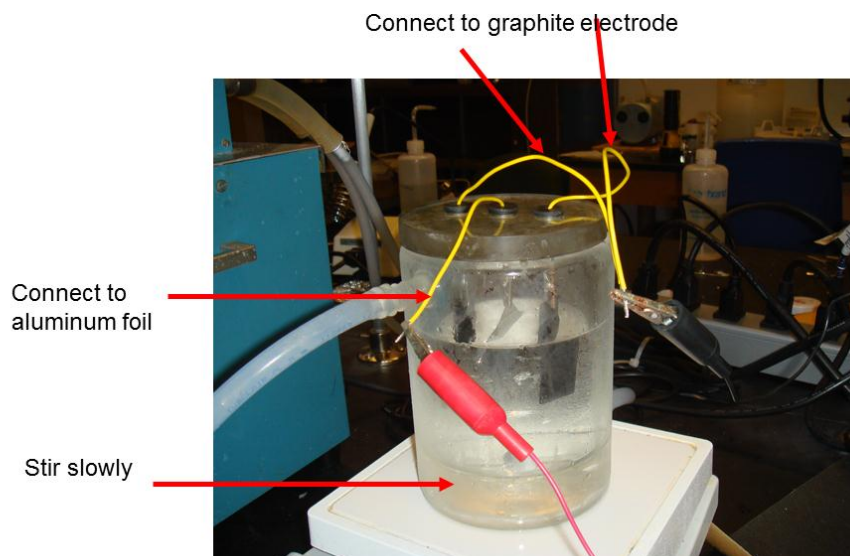
1. Prepare the mixture of HClO_4 (60%) and $\text{C}_2\text{H}_5\text{OH}$ (anhydrous) (volume ratio 1:4, 100ml + 400ml). Put the mixture into beaker with chiller
2. Turn on both switch of the chiller for electropolishing until 8 degree celcius. (~30 minutes)



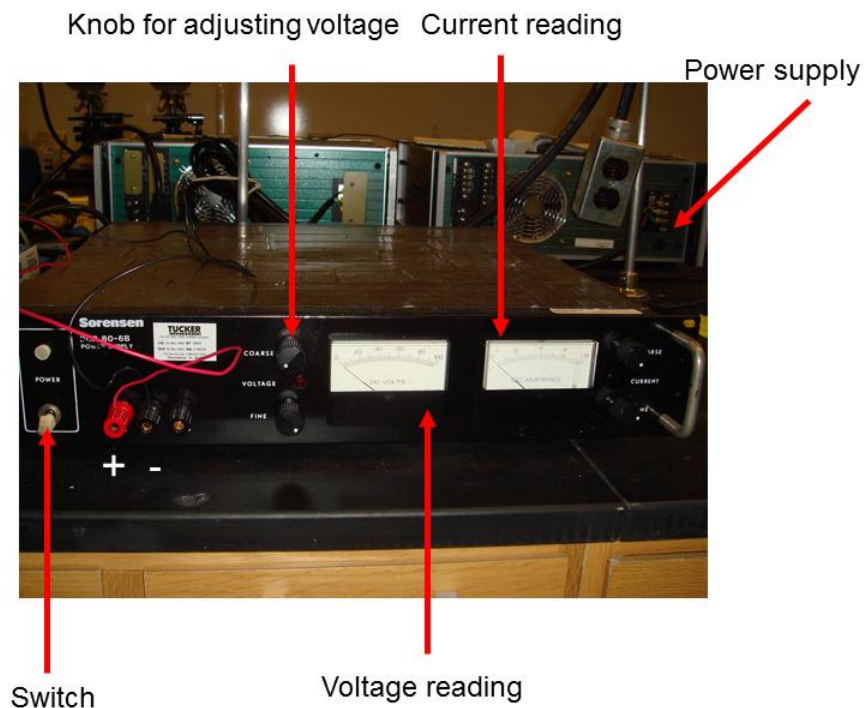
Clamp two graphite electrodes and aluminum foil



1. Connect power supply and electrodes, "+" (red line) to aluminum foil. "-" (black line) to graphite electrode
2. Put the electrodes and foil into solution and stir the solution slowly



Slowly apply voltage to 20 V and start count time. Note: if you apply the voltage too fast, the current will exceed to 2 A, and make sure that the current is always less than 2 A



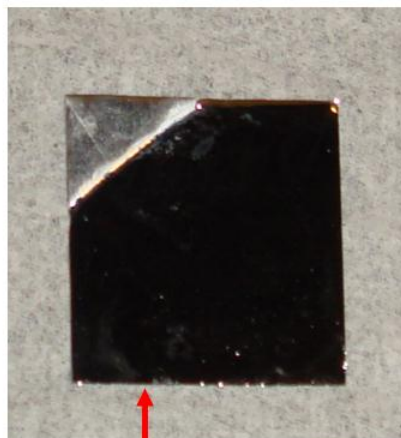
Keep 20 V until 4 minutes.



20V

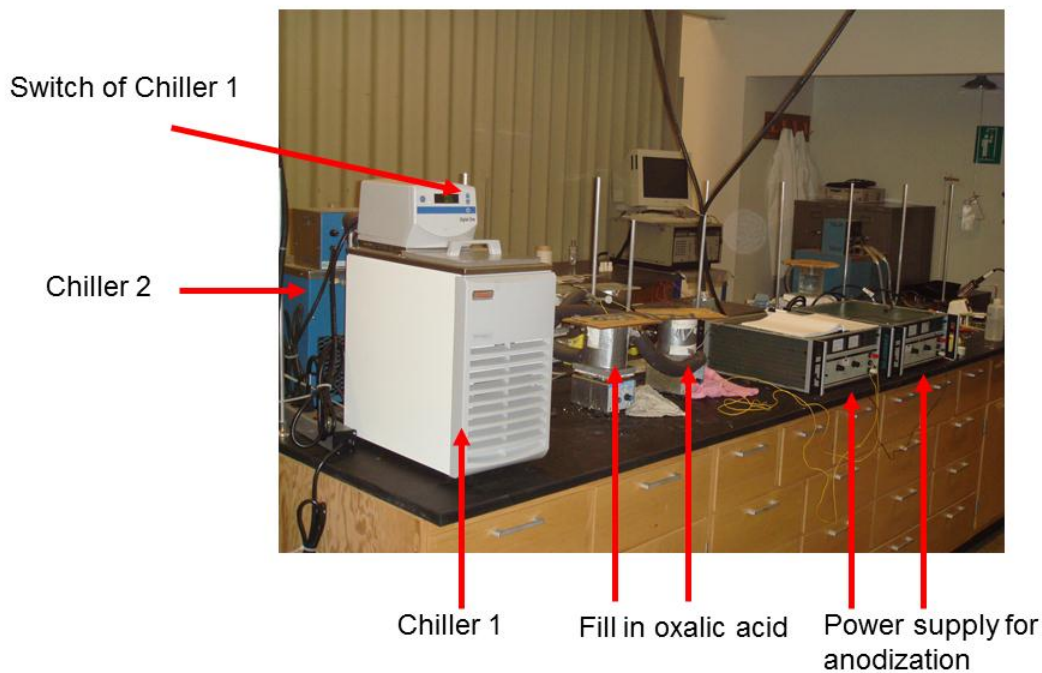
Always less than 2A

Take out the sample and rinse electrode and sample with DI water 10-15 sec and then dry it with Kimwipes



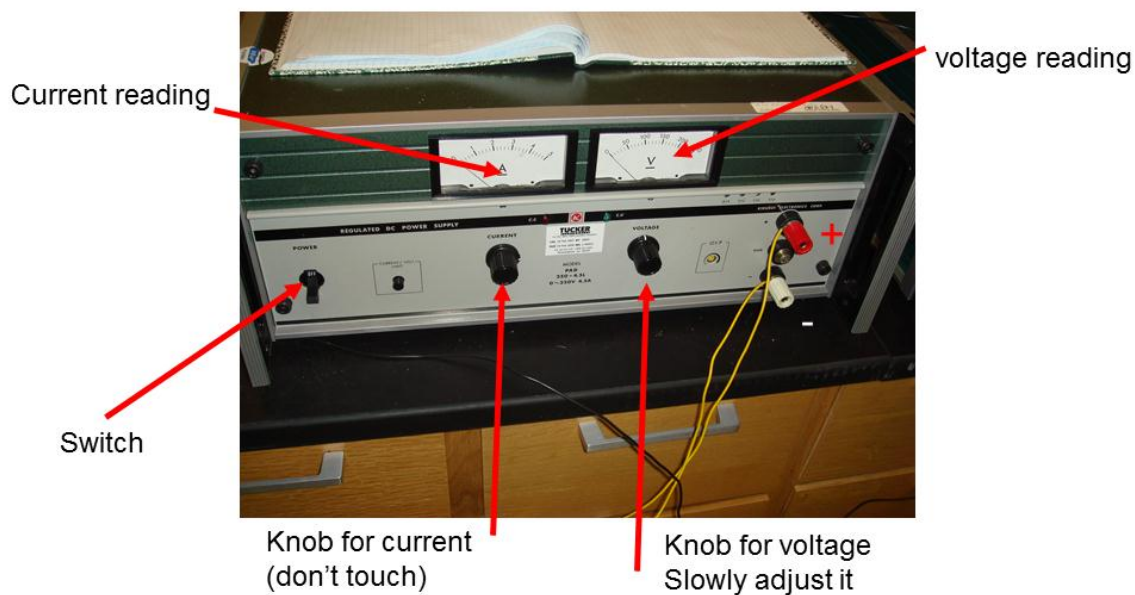
Sample after electropolishing
The color is shiny metal color

1. Turn on the chiller for anodination until the setting temperature (temperature of solution is 2-3 degree Celsius)
2. Prepare 0.3 M oxalic acid (37.82 g in 1 liter water)



1. Clamp two graphite electrodes and aluminum foil.
2. Connect power supply and electrodes, "+" (red) to aluminum foil. "-" (white) to graphite electrode.
3. Put the electrodes and foil into solution and stir the solution slowly. See the figure in electropolishing as reference

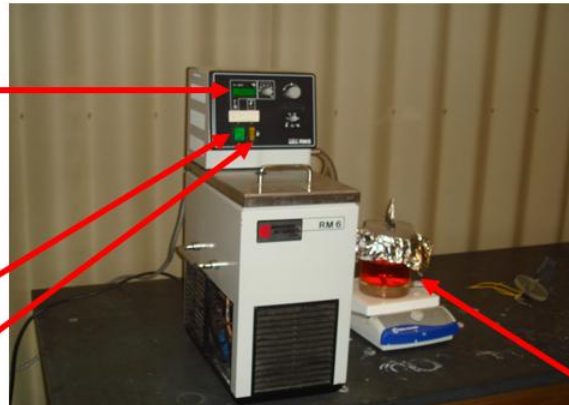
1. Apply voltage to 40 V, make sure that the current is always less than 0.2 A. Note1: if current is larger than 0.2 A, the sample will dissolve in solution. Note2: The status of anodization needs to be checked frequently in first one hour to prevent the high current.
2. Stir slowly and do anodization for 12 hours.
3. Take out the sample and rinse electrode and sample with DI water 10-15 sec and then dry it with Kimwipes
4. The sample color is same as the one after second anodization



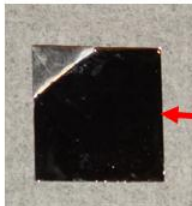
1. Prepare 0.6 M H_3PO_4 and 0.2 M CrO_3 aqueous solution (20 g CrO_3 and 41 ml 85% H_3PO_4 in 1 liter water solution)
2. Turn on the heater for etching step and wait until the setting temperature (56.2 Celsius degree) Clamp the sample and immerse into the mixture.
3. Stir slowly and etching 6 hours
4. rinse sample with a lot of DI water and then dry it

Temperature reading

Turn on both switches

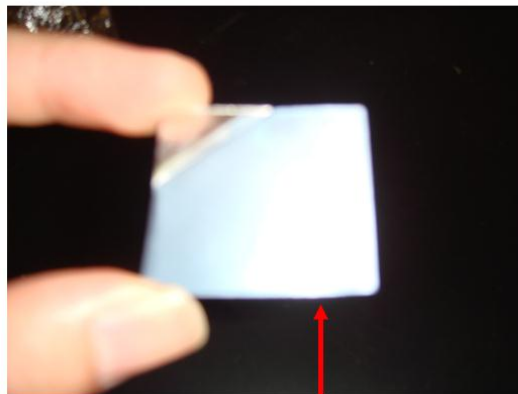


Fill in mixture
Solution of step 1



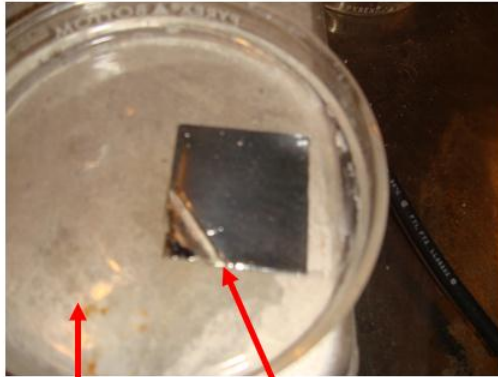
After etching, the color is shiny again

Repeat slide 9 but change to 24 hours



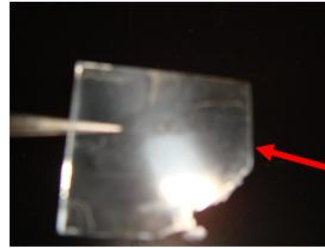
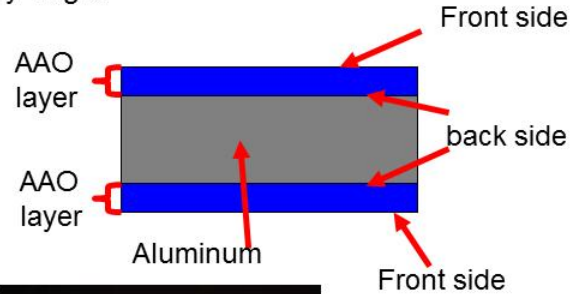
Sample after second anodization
The color is blue (hard to see from photo)

1. Immerse the sample into saturate mercury chloride solution.
2. The mercury chloride solution will react with aluminum and detach the both aluminum oxide layer. Note 1: you should see bubble when mercury chloride reacts with aluminum. If you don't see bubble, you should change new mercury chloride solution. Note 2: make sure which side of detached aluminum oxide is top side and which side is bottom side. This is very important for electrodeposition. Note 3: The detached aluminum oxide layer is very fragile



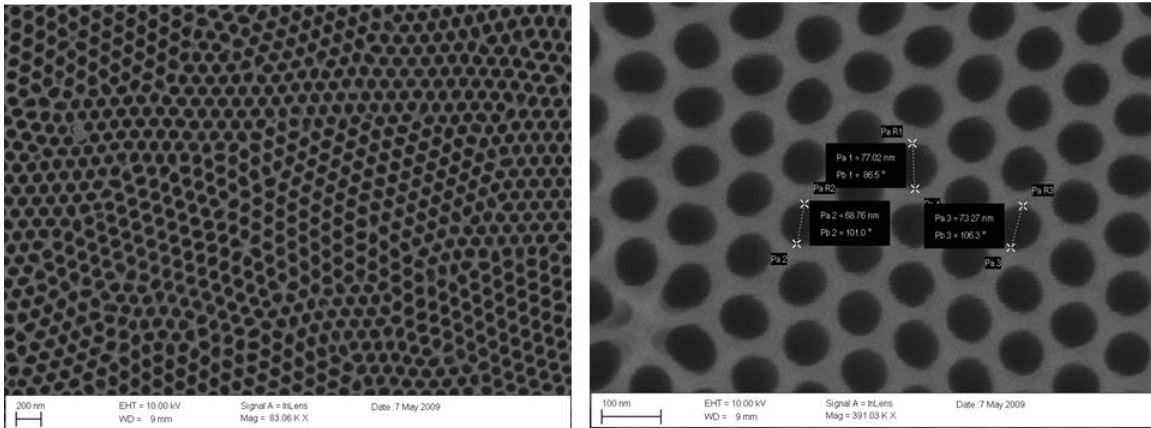
Mercury chloride solution

bubble

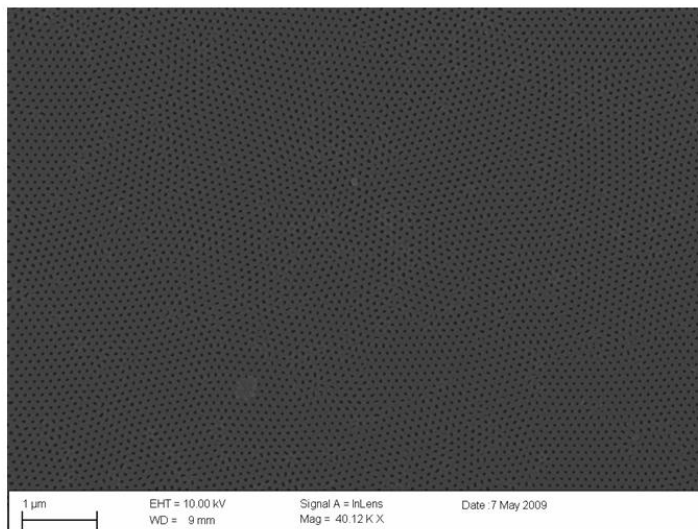


AAO layer transparent

1. prepare 8.5% H₃PO₄ solution for pore widening step
2. Float detached aluminum oxide layer on top of 8.5% H₃PO₄ solution (6.5ml 85% H₃PO₄ add water to 100ml), and the bottom part touches the solution for 1 hour, and you should see bubbles and the oxide layer sinks.

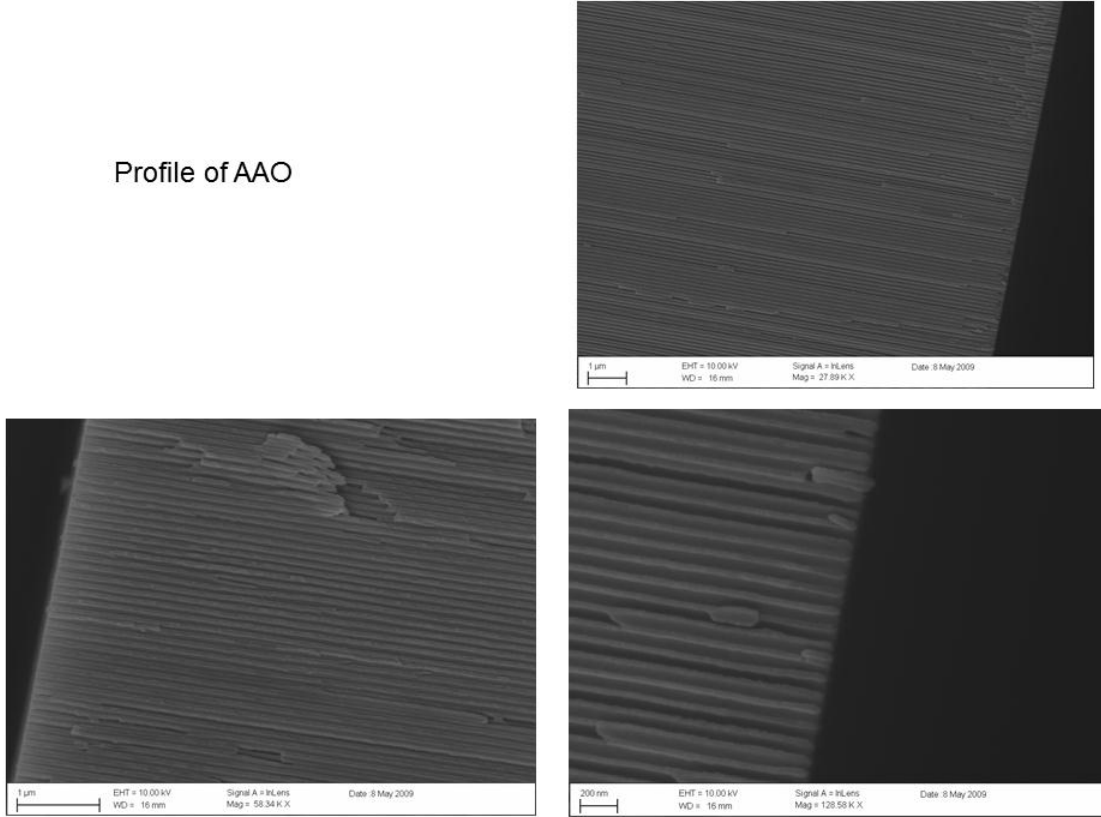


Front side and magnification of AAO which is after pore widening
Pore size ~75nm



Back side after pore widening

Profile of AAO



The procedures above demonstrate how to synthesize AAO templates. Next are the procedures of how to deposit different segments of nanorods electrochemically:

Thermal deposition of Ag layer onto AAO template (~ 500 nm)

1. The thermal deposition machine is in clean room of NST, and you need to get training before using it. The procedure of thermal deposition machine is skipped here. The deposition rate for this purpose is 1-1.5 A/sec. Note: the silver layer is for conducting so it should be deposit at back side of AAO
2. After thermal deposition, the good AAO should have the gold (yellow) color. That's good color for deposition purpose

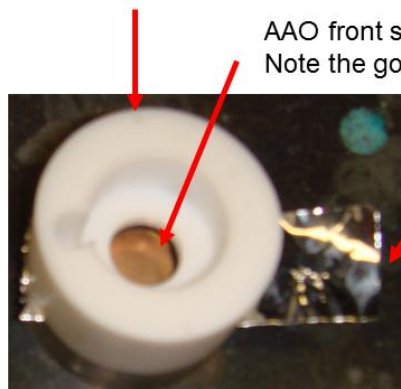
1. Cut the silver-deposited AAO template – 1.5 x 1.5 cm
2. Cut Aluminum foil 1.5 x 5 cm
3. Using Al foil as a electrode, assembly the electrochemical cell- tightly screw the bolt
 - a. Pt mesh is counter electrode
 - b. Al foil with AAO template is working electrode
 - c. Ag/AgCl is reference electrode
4. Add the silver plating solution (1.5 ml) in cell

Before assembling

Top view of electrochemical cell



After assembling aluminum foil and AAO



AAO front side face up
Note the gold color

aluminum
foil

There are two screws in the bottom for assembling

The deposition setup after assembling cell and connection

reference electrode (white) connect to Ag/AgCl

counter electrode (red) connect to mesh



Ag/AgCl
electrode

Pt mesh

Adding Plating solution inside cell

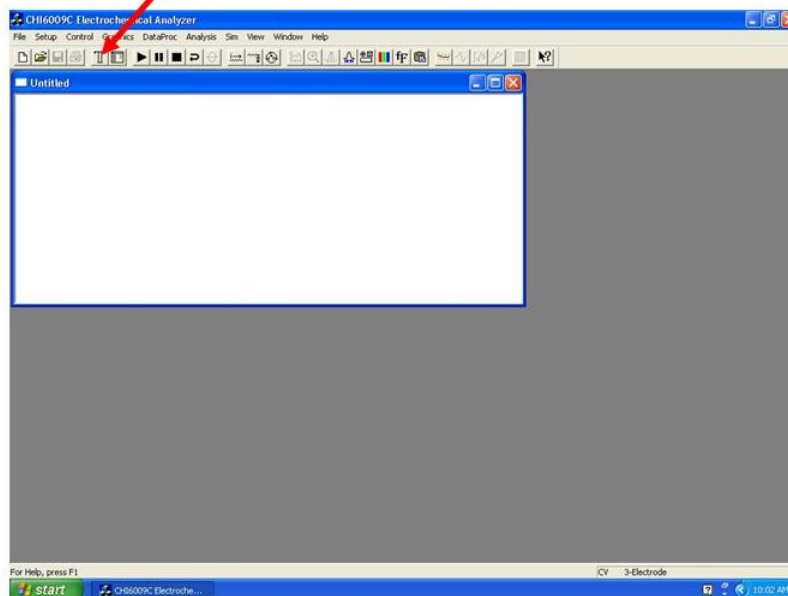
Working electrode (green) connect to foil

Open the e-chem computer program

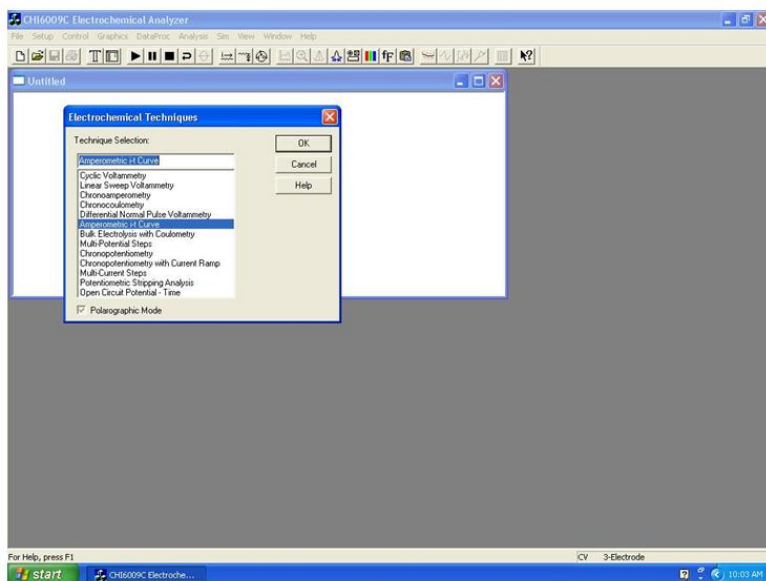


Choose the potential step method

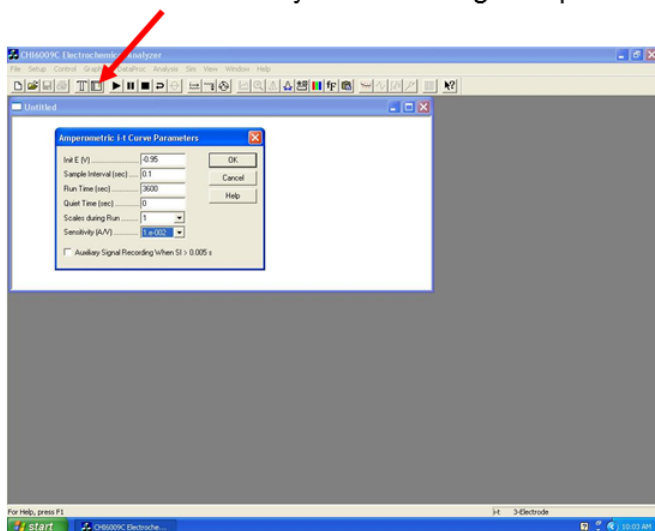
Click this "T" symbol



Choose Amper i-t curve



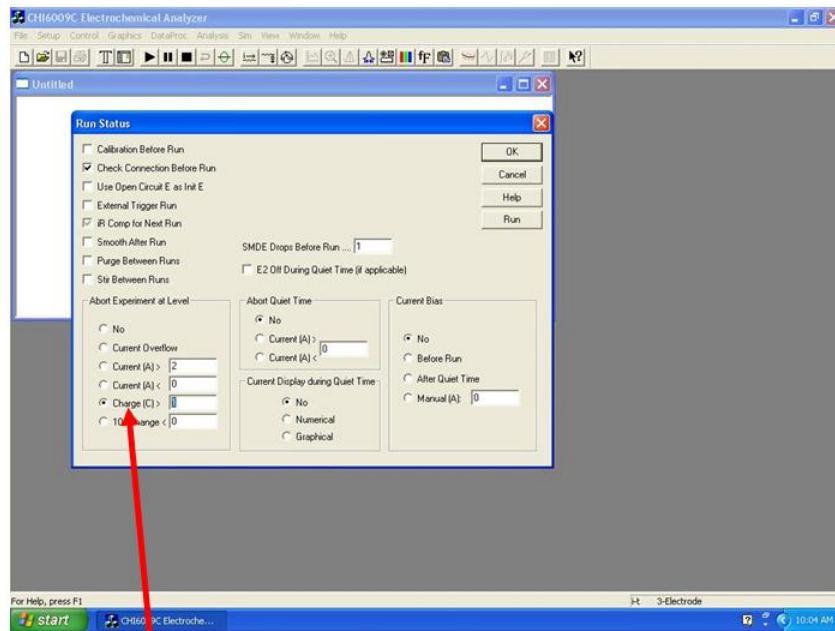
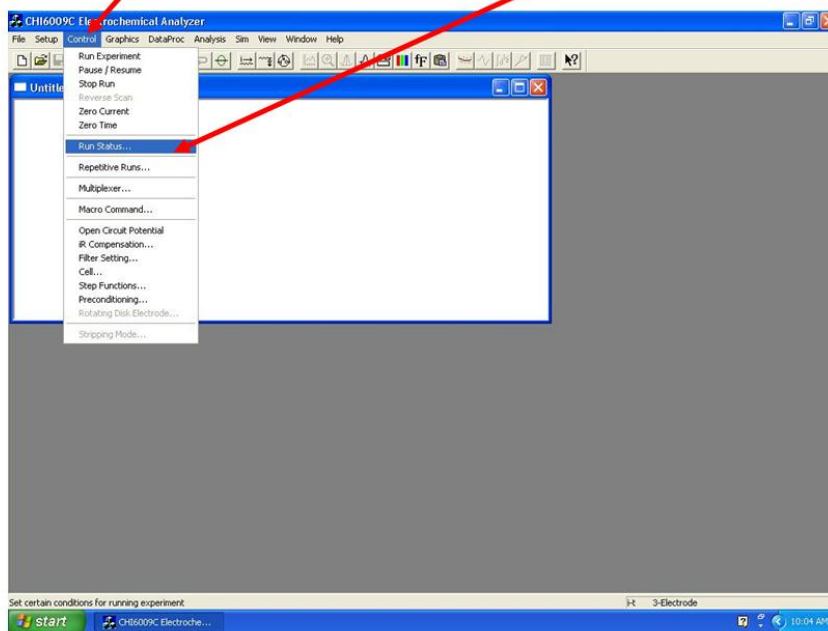
Click this symbol to change the parameter



In figure:

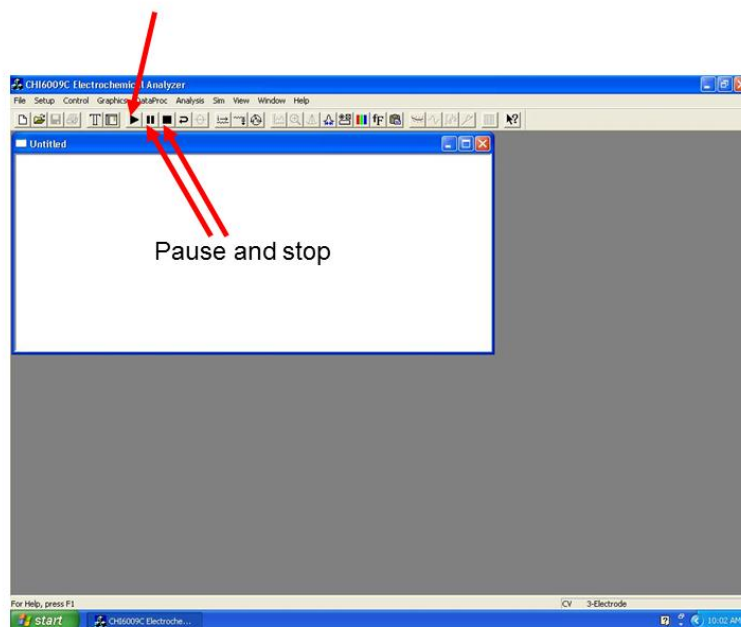
1. Init V is the potential we used. Ag and Au is -0.9 V Ni is -0.95 V
2. Sample interval : use default
3. Run time: usually 3600 sec or more but we use amount of charge to control the reaction time
4. Quiet time: default
5. Scale during run: default
6. Sensitivity: 1×10^{-2}

Click control and then choose Run status

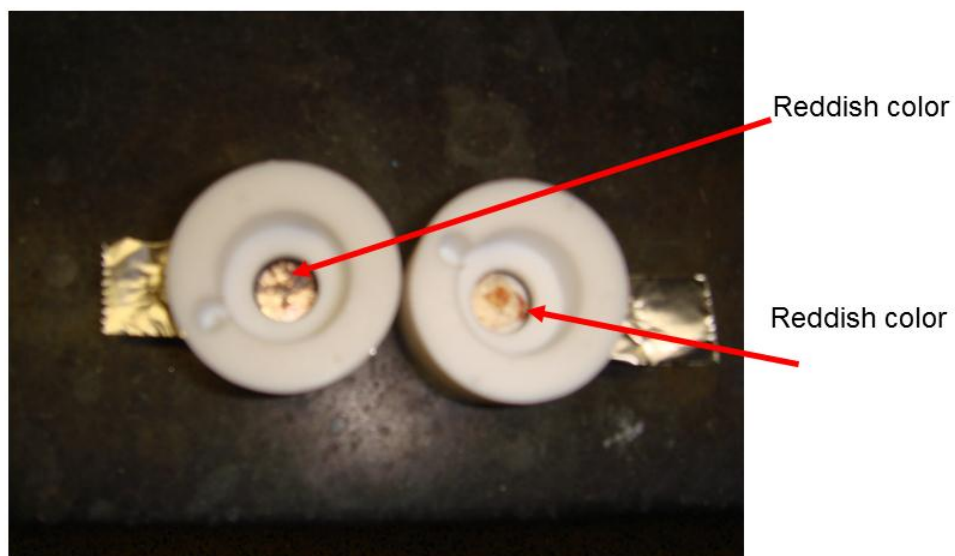


Change the amount of charges here (the unit is Coulumb, C)
Depends on the length you need to change different Coulumb

After setting up all parameters, hit this arrow symbol to run reaction



For our purpose, we need to deposit 1 C silver first
So we choose the parameter $V = -0.9$ V and 1 C and run the program as previous slides show. After 1C silver deposition, the ok sample should show more than half reddish color.
If not, throw it away.



After finishing electrodeposition, wash the electrochemical cell with D.I. water carefully

Deposit Au:

1. Add the Gold electro-plating solution (transparent) (1.5 ml)
2. Put the parameter for desire purpose
Voltage: (-0.90 V)
Charge: (0.13 C) – 80 nm
3. Run the electrochemistry program

After finishing electrodeposition, wash the electrochemical cell with D.I. water carefully

Deposit Ni:

1. Add the nickel electro-plating solution (green) (1.5 ml)
2. Put the parameter for desire purpose
Voltage: (-0.95 V)
Charge: (0.02 C) – 10 nm
3. Run the electrochemistry program

After finishing electrodeposition, wash the electrochemical cell with D.I. water carefully

Deposit Au:

1. Add the Gold electro-plating solution (transparent) (1.5 ml)
2. Put the parameter for desire purpose
Voltage: (-0.90 V)
Charge: (0.13 C) – 80 nm
3. Run the electrochemistry program

After finishing electrodeposition, wash the electrochemical cell with D.I. water carefully

Deposit Ni:

1. Add the nickel electro-plating solution (green) (1.5 ml)
2. Put the parameter for desire purpose
Voltage: (-0.95 V)
Charge: (3 C) – 3 um
3. Run the electrochemistry program

After finishing electrodeposition, wash the electrochemical cell with D.I. water carefully

Deposit Au:

1. Add the Gold electro-plating solution (transparent) (1.5 ml)
2. Put the parameter for desire purpose
Voltage: (-0.90 V)
Charge: (0.18 C) – 130 nm
3. Run the electrochemistry program

After finishing electrodeposition, wash the electrochemical cell with D.I. water carefully

1. Disassemble the electrochemical cell
2. Dry the sample
3. Using nitric acid solution (w/w 50 %), etch out the silver layer.

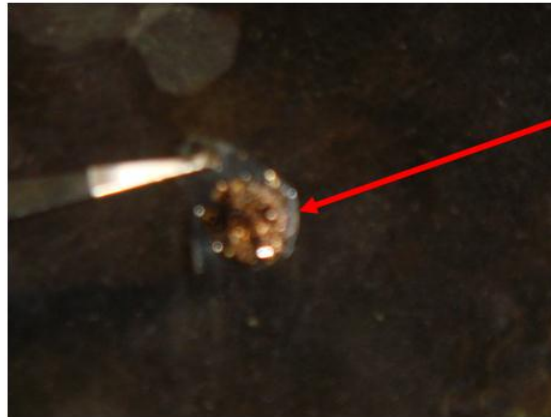


Sample after all steps



etch out the silver layer note the white color becomes transparent

1. Wash sample with DI water to remove acid
 2. Using 6 M NaOH solution, dissolve the AAO template.
- Note that Sonication will help the dissolution of AAO template (1 Hr)



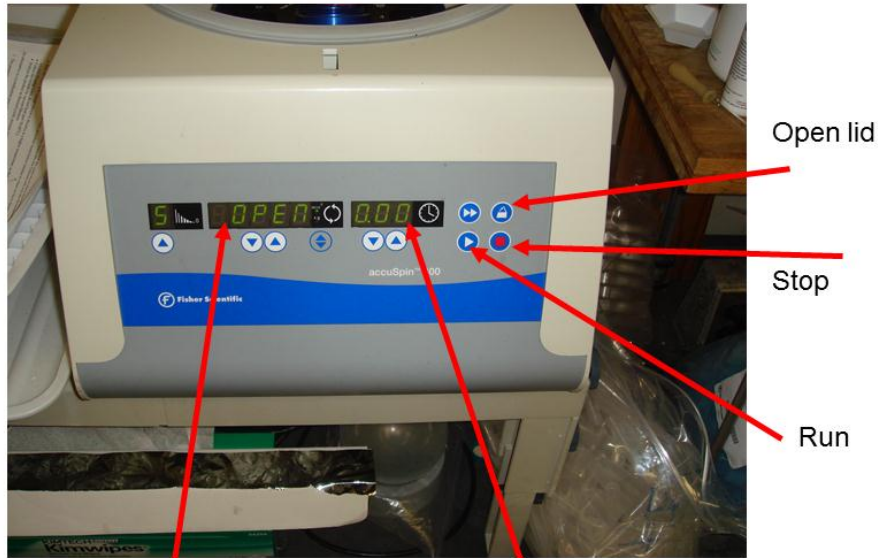
Sample after acid etching

Put sample with sodium hydroxide solution in centrifuge tube
Adding the D.I. water to tube to centrifuge (wash) the sample
After centrifugation for 2hrs, we can get bare nanorod samples.(repeat 2-3 times)



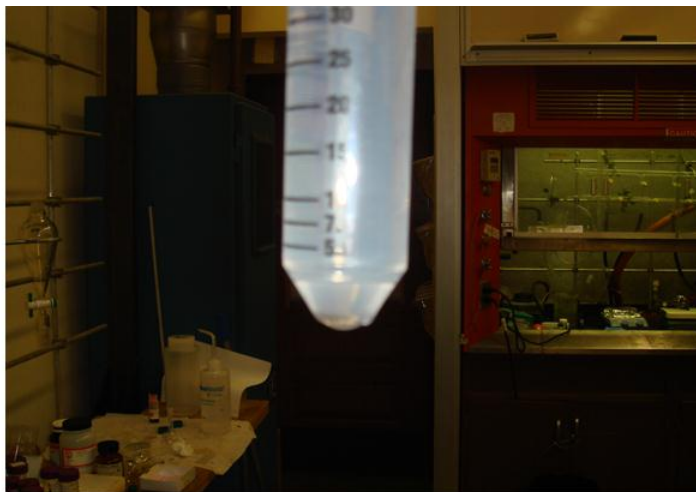
Put equal weight sample
In diagonal direction

Next page shows the
function of
centrifuge machine



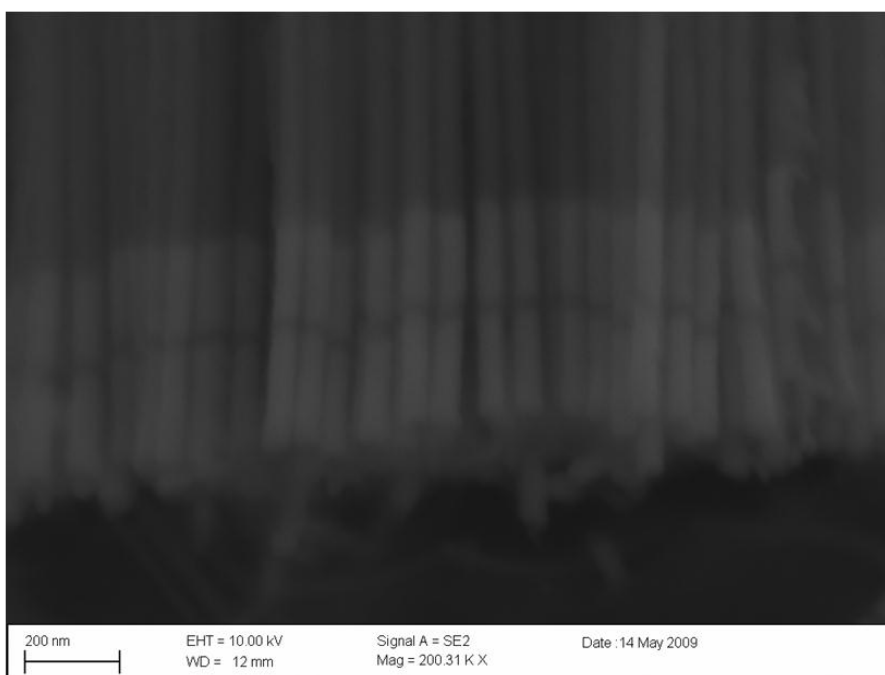
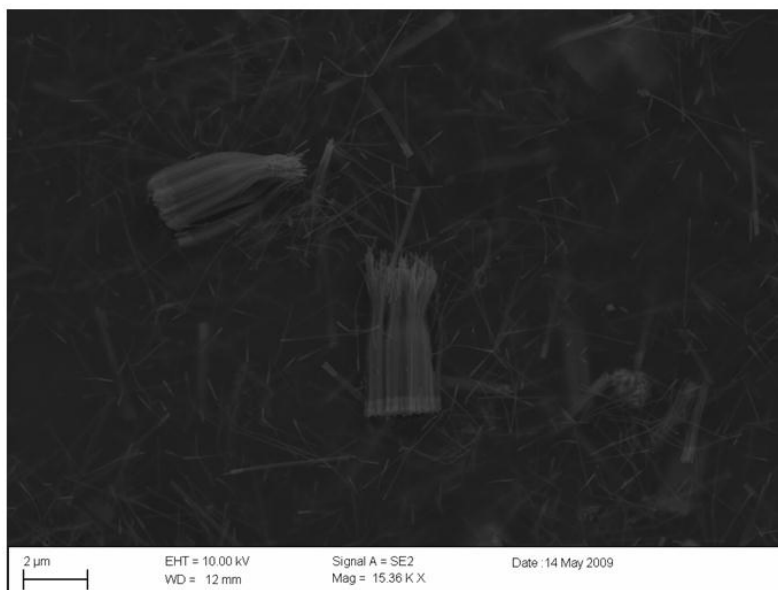
Rotating speed (rpm)
 You can adjust by the arrows button below it
 We always use 4000 rpm

Rotating time (hour : minutes)
 You can adjust by the arrows below it



After centrifuging, you should be able to see some particulate in the bottom of the tube

1. Take out the water solution and only left the particulate
2. Adding 2 ml of i-PrOH to disperse bare nanorods
3. Sonication for 10 mins



References

1. Pawley, J. B., *Handbooks of Biological Confocal Microscopy* 3rd ed.; Springer: 2006.
2. Wayne, R., *Light and Video Microscopy*. 1st ed.; Academic Press: 2009.
3. Lakowicz, J. R., *Principles of Fluorescence Spectroscopy*. 3rd ed.; Springer: 2006.
4. McHale, J. L., *Molecular Spectroscopy*. Prentice Hall, New Jersey: 1999.
5. (a) Ferraro, J. R.; Nakamoto, K.; Brown, C. W., *Introductory Raman Spectroscopy*. 2nd ed.; Academic Press: 2003; (b) Smith, E.; Dent, G., *Modern Raman Spectroscopy*. John Wiley & Sons: 2005.
6. Le Ru, E. C.; Etchegoin, P. G., *Principles of Surface-Enhanced Raman Spectroscopy: and related plasmonic effects*. Elsevier Science: 2008.
7. Huang, Y. S.; Karashima, T.; Yamamoto, M.; Hamaguchi, H., Molecular-level investigation of the structure, transformation, and bioactivity of single living fission yeast cells by time- and space-resolved Raman spectroscopy. *Biochemistry* **2005**, *44* (30), 10009-10019.
8. Eesley, G. L., *Coherent Raman Spectroscopy*. 1st ed.; Pergamon Press: 1981.
9. Aroca, R., *Surface enhanced vibrational spectroscopy*. John Wiley & Sons: 2006.
10. Chen, B.-C.; Lim, S.-H., Optimal laser pulse shaping for interferometric multiplex coherent anti-stokes Raman scattering microscopy. *J. Phys. Chem. B* **2008**, *112* (12), 3653-3661.
11. (a) Langbein, W.; Rocha-Mendoza, I.; Borri, P., Single source coherent anti-Stokes Raman microspectroscopy using spectral focusing. *Applied Physics Letters* **2009**, *95* (8); (b) Langbein, W.; Rocha-Mendoza, I.; Borri, P., Coherent anti-Stokes Raman micro-spectroscopy using spectral focusing: theory and experiment. *Journal of Raman Spectroscopy* **2009**, *40* (7), 800-808; (c) Pegoraro, A. F.; Ridsdale, A.; Moffatt, D. J.; Jia, Y.; Pezacki, J. P.; Stolow, A., Optimally chirped multimodal CARS microscopy based on a single Ti: sapphire oscillator.

- Optics Express* **2009**, *17* (4), 2984-2996; (d) Rocha-Mendoza, I.; Langbein, W.; Borri, P., Coherent anti-Stokes Raman microspectroscopy using spectral focusing with glass dispersion. *Applied Physics Letters* **2008**, *93*, 201103 (e) Hellerer, T.; Enejder, A. M. K.; Zumbusch, A., Spectral focusing: High spectral resolution spectroscopy with broad-bandwidth laser pulses. *Applied Physics Letters* **2004**, *85* (1), 25-27.
12. Maier, S. A., *Plasmonics: fundamentals and applications*. Springer Verlag: 2007.
 13. Boyd, G. T.; Yu, Z. H.; Shen, Y. R., Photoinduced luminescence from the noble metals and its enhancement on roughened surfaces. *Physical Review B* **1986**, *33* (12), 7923-7936.
 14. Muhlschlegel, P.; Eisler, H. J.; Martin, O. J. F.; Hecht, B.; Pohl, D. W., Resonant optical antennas. *Science* **2005**, *308* (5728), 1607-1609.
 15. McCamant, D. W.; Kukura, P.; Yoon, S.; Mathies, R. A., Femtosecond broadband stimulated Raman spectroscopy: Apparatus and methods. *Review of Scientific Instruments* **2004**, *75* (11), 4971-4980.
 16. Boyd, R. W., *Nonlinear Optics*. 3rd ed.; Academic Press: 2008.
 17. (a) Cheng, J. X.; Xie, X. S., Coherent anti-Stokes Raman scattering microscopy: Instrumentation, theory, and applications. *Journal of Physical Chemistry B* **2004**, *108* (3), 827-840; (b) Eric O. Potma; Xie, S., In *Handbook of Biomedical Nonlinear Optical Microscopy*, Masters, B. R.; So, P. T. C., Eds. Oxford University Press: 2008; (c) Evans, C. L.; Xie, X. S., Coherent Anti-Stokes Raman Scattering Microscopy: Chemical Imaging for Biology and Medicine. *Annual Review of Analytical Chemistry* **2008**, *1*, 883-909; (d) Muller, M.; Zumbusch, A., Coherent anti-stokes Raman scattering microscopy. *Chemphyschem* **2007**, *8* (15), 2157-2170.
 18. Zumbusch, A.; Holtom, G. R.; Xie, X. S., Three-dimensional vibrational imaging by coherent anti-Stokes Raman scattering. *Physical Review Letters* **1999**, *82* (20), 4142-4145.

19. (a) Dudovich, N.; Oron, D.; Silberberg, Y., Single-pulse coherently controlled nonlinear Raman spectroscopy and microscopy. *Nature* **2002**, *418* (6897), 512-514; (b) Oron, D.; Dudovich, N.; Yelin, D.; Silberberg, Y., Narrow-band coherent anti-stokes Raman signals from broad-band pulses. *Physical Review Letters* **2002**, *88*, 063004; (c) Dudovich, N.; Oron, D.; Silberberg, Y., Single-pulse coherent anti-Stokes Raman spectroscopy in the fingerprint spectral region. *Journal of Chemical Physics* **2003**, *118* (20), 9208-9215; (d) Oron, D.; Dudovich, N.; Silberberg, Y., Femtosecond phase-and-polarization control for background-free coherent anti-Stokes Raman spectroscopy. *Physical Review Letters* **2003**, *90*, 213902; (e) Silberberg, Y., Quantum Coherent Control for Nonlinear Spectroscopy and Microscopy. *Annual Review of Physical Chemistry*, **2009**; *60*, 277-292.
20. (a) Cheng, J. X.; Volkmer, A.; Book, L. D.; Xie, X. S., An epi-detected coherent anti-stokes raman scattering (E-CARS) microscope with high spectral resolution and high sensitivity. *Journal of Physical Chemistry B* **2001**, *105* (7), 1277-1280; (b) Volkmer, A.; Cheng, J. X.; Xie, X. S., Vibrational imaging with high sensitivity via epidetected coherent anti-Stokes Raman scattering microscopy. *Phys. Rev. Lett.* **2001**, *87* (2), 023901.
21. Cheng, J. X.; Book, L. D.; Xie, X. S., Polarization coherent anti-Stokes Raman scattering microscopy. *Opt. Lett* **2001**, *26* (17), 1341-1343.
22. Volkmer, A.; Book, L. D.; Xie, X. S., Time-resolved coherent anti-Stokes Raman scattering microscopy: Imaging based on Raman free induction decay. *Applied Physics Letters* **2002**, *80* (9), 1505-1507.
23. Wurpel, G. W. H.; Schins, J. M.; Muller, M., Direct measurement of chain order in single phospholipid mono- and bilayers with multiplex CARS. *J. Phys. Chem. B* **2004**, *108* (11), 3400-3403.
24. Powers, P. E., *Fundamentals of Nonlinear Optics*. CRC Press: 2011.
25. (a) Kukura, P.; McCamant, D. W.; Mathies, R. A., Femtosecond stimulated Raman spectroscopy. *Annual Review of Physical Chemistry*, **2007**; *58*, 461-488;

- (b) Min, W.; Freudiger, C. W.; Lu, S.; Xie, X. S., Coherent Nonlinear Optical Imaging: Beyond Fluorescence Microscopy. *Annual Review of Physical Chemistry* **2011**, *62*, 507-530.
26. Shen, Y. R., *The Principles of Nonlinear Optics*. John Wiley & Sons 1984.
27. Nandakumar, P.; Kovalev, A.; Volkmer, A., Vibrational imaging based on stimulated Raman scattering microscopy. *New Journal of Physics* **2009**, *11*, 033026.
28. McCamant, D. W.; Kukura, P.; Mathies, R. A., Femtosecond broadband stimulated Raman: A new approach for high-performance vibrational spectroscopy. *Applied Spectroscopy* **2003**, *57* (11), 1317-1323.
29. (a) Freudiger, C. W.; Min, W.; Saar, B. G.; Lu, S.; Holtom, G. R.; He, C. W.; Tsai, J. C.; Kang, J. X.; Xie, X. S., Label-Free Biomedical Imaging with High Sensitivity by Stimulated Raman Scattering Microscopy. *Science* **2008**, *322* (5909), 1857-1861; (b) Saar, B. G.; Freudiger, C. W.; Reichman, J.; Stanley, C. M.; Holtom, G. R.; Xie, X. S., Video-Rate Molecular Imaging in Vivo with Stimulated Raman Scattering. *Science* **2010**, *330* (6009), 1368-1370; (c) Freudiger, C. W.; Min, W.; Holtom, G. R.; Xu, B. W.; Dantus, M.; Xie, X. S., Highly specific label-free molecular imaging with spectrally tailored excitation-stimulated Raman scattering (STE-SRS) microscopy. *Nature Photonics* **2011**, *5* (2), 103-109.
30. (a) Kukura, P.; Yoon, S.; Mathies, R. A., Femtosecond stimulated Raman spectroscopy. *Analytical Chemistry* **2006**, *78* (17), 5952-5959; (b) Shim, S.; Stuart, C. M.; Mathies, R. A., Resonance Raman cross-sections and vibronic analysis of rhodamine 6G from broadband stimulated Raman spectroscopy. *Chemphyschem* **2008**, *9* (5), 697-699; (c) Frontiera, R. R.; Mathies, R. A., Femtosecond stimulated Raman spectroscopy. *Laser & Photonics Reviews* **2011**, *5* (1), 102-113.

31. Ploetz, E.; Laimgruber, S.; Berner, S.; Zinth, W.; Gilch, P., Femtosecond stimulated Raman microscopy. *Applied Physics B-Lasers and Optics* **2007**, *87* (3), 389-393.
32. Ozeki, Y.; Dake, F.; Kajiyama, S. i.; Fukui, K.; Itoh, K., Analysis and experimental assessment of the sensitivity of stimulated Raman scattering microscopy. *Optics Express* **2009**, *17* (5), 3651-3658.
33. Judson, R. S.; Rabitz, H., Teaching lasers to control molecules. *Physical Review Letters* **1992**, *68* (10), 1500-1503.
34. Meshulach, D.; Silberberg, Y., Coherent quantum control of two-photon transitions by a femtosecond laser pulse. *Nature* **1998**, *396* (6708), 239-242.
35. Tannor, D. J., *Introduction to Quantum mechanics: A Time-Dependent Perspective*. University Science Books: 2007.
36. Oron, D.; Dudovich, N.; Yelin, D.; Silberberg, Y., Quantum control of coherent anti-Stokes Raman processes. *Physical Review A* **2002**, *65* (4), 043408.
37. Chen, B.-C.; Sung, J.; Lim, S.-H., Chemical Imaging with Frequency Modulation Coherent Anti-Stokes Raman Scattering Microscopy at the Vibrational Fingerprint Region. *Journal of Physical Chemistry B* **2010**, *114* (50), 16871-16880.
38. Scofield, J. H., Frequency-domain description of a lock-in amplifier. *American Journal of Physics* **1994**, *62* (2), 129-133.
39. Finsterbusch, K.; Bayer, A.; Zacharias, H., Tunable, narrow-band picosecond radiation in the mid-infrared by difference frequency mixing in GaSe and CdSe. *Applied Physics B-Lasers and Optics* **2004**, *79* (4), 457-462.
40. Min, W.; Lu, S.; Holtom, G. R.; Xie, X. S., Triple-Resonance Coherent Anti-Stokes Raman Scattering Microspectroscopy. *Chemphyschem* **2009**, *10* (2), 344-347.
41. Kasatani, K.; Sato, H., Viscosity-dependent decay dynamics of the S-2 state of cyanine dyes with 3, 5, and 7 methine units by picosecond fluorescence lifetime

- measurements. *Bulletin of the Chemical Society of Japan* **1996**, *69* (12), 3455-3460.
42. Sekiguchi, K.; Yamaguchi, S.; Tahara, T., Formation and dissociation of rhodamine 800 dimers in water: Steady-state and ultrafast spectroscopic study. *Journal of Physical Chemistry A* **2006**, *110* (8), 2601-2606.
43. Lin-Vien, D.; Colthup, N. B.; Fateley, W. G.; Grasselli, J. G., *The Handbook of Infrared and Raman Characteristic Frequencies of Organic Molecules*. Academic Press: 1991.
44. Wang, S. Y.; Hasty, C. E.; Watson, P. A.; Wicksted, J. P.; Stith, R. D.; March, W. F., Analysis of Metabolites in Aqueous-Solutions by Using Laser Raman-Spectroscopy. *Applied Optics* **1993**, *32* (6), 925-929.
45. Ianoul, A.; Coleman, T.; Asher, S. A., UV resonance Raman spectroscopic detection of nitrate and nitrite in wastewater treatment processes. *Analytical Chemistry* **2002**, *74* (6), 1458-1461.
46. Lee, H. I.; Kim, M. S.; Suh, S. W., Raman-Spectroscopy of L-Phenylalanine, L-Tyrosine, and Their Peptides Absorbed on Silver Surface. *Bulletin of the Korean Chemical Society* **1988**, *9* (4), 218-223.
47. Arora, R.; Petrov, G. I.; Liu, J. A.; Yakovlev, V. V., Improving sensitivity in nonlinear Raman microspectroscopy imaging and sensing. *Journal of Biomedical Optics* **2011**, *16* (2), 021114.
48. (a) Fleischm.M; Hendra, P. J.; McQuilla.Aj, Raman-Spectra of pyridine absorbed at a silver electrode. *Chemical Physics Letters* **1974**, *26* (2), 163-166; (b) Jeanmaire, D. L.; Van duyne, R. P., Surface Raman spectroelectrochemistry. 1. heterocyclic, aromatic, and aliphatic-amines absorbed on anodized silver electrode. *Journal of Electroanalytical Chemistry* **1977**, *84* (1), 1-20.
49. (a) Kneipp, K.; Wang, Y.; Kneipp, H.; Perelman, L. T.; Itzkan, I.; Dasari, R.; Feld, M. S., Single molecule detection using surface-enhanced Raman scattering (SERS). *Physical Review Letters* **1997**, *78* (9), 1667-1670; (b) Nie, S. M.; Emery,

- S. R., Probing single molecules and single nanoparticles by surface-enhanced Raman scattering. *Science* **1997**, 275 (5303), 1102-1106.
50. (a) Moskovits, M., Surface-enhanced spectroscopy. *Reviews of Modern Physics* **1985**, 57 (3), 783-826; (b) Campion, A.; Kambhampati, P., Surface-enhanced Raman scattering. *Chemical Society Reviews* **1998**, 27 (4), 241-250; (c) Tian, Z. Q.; Ren, B.; Wu, D. Y., Surface-enhanced Raman scattering: From noble to transition metals and from rough surfaces to ordered nanostructures. *Journal of Physical Chemistry B* **2002**, 106 (37), 9463-9483; (d) Otto, A., The 'chemical' (electronic) contribution to surface-enhanced Raman scattering. *Journal of Raman Spectroscopy* **2005**, 36 (6-7), 497-509; (e) Willets, K. A.; Van Duyne, R. P., Localized surface plasmon resonance spectroscopy and sensing. *Annual Review of Physical Chemistry* **2007**, 58, 267-297; (f) Brus, L., Noble Metal Nanocrystals: Plasmon Electron Transfer Photochemistry and Single-Molecule Raman Spectroscopy. *Accounts of Chemical Research* **2008**, 41 (12), 1742-1749; (g) Etchegoin, P. G.; Le Ru, E. C., A perspective on single molecule SERS: current status and future challenges. *Physical Chemistry Chemical Physics* **2008**, 10 (40), 6079-6089; (h) Camden, J. P.; Dieringer, J. A.; Zhao, J.; Van Duyne, R. P., Controlled Plasmonic Nanostructures for Surface-Enhanced Spectroscopy and Sensing. *Accounts of Chemical Research* **2008**, 41 (12), 1653-1661.
51. (a) Bohren, C. F.; Huffman, D. R., *Absorption and scattering of light by small particles*. John Wiley & Sons, New York: 1983; (b) Kneipp, K.; Moskovits, M.; Kneipp, H., *Surface-enhanced Raman scattering: physics and applications*. Springer Verlag: 2006; Vol. 103; (c) Kreibig, U.; Vollmer, M., *Optical properties of metal clusters*. Springer: 1995; (d) Novotny, L.; Hecht, B., *Principles of nano-optics*. Cambridge University Press: 2006.
52. Griffiths, D. J., *Introduction to electrodynamics*. 3rd ed.; Prentice Hall New Jersey: 1999.

53. Kelly, K. L.; Coronado, E.; Zhao, L. L.; Schatz, G. C., The optical properties of metal nanoparticles: The influence of size, shape, and dielectric environment. *Journal of Physical Chemistry B* **2003**, *107* (3), 668-677.
54. Draine, B. T.; Flatau, P. J. User guide for the discrete dipole approximation code DDSCAT 6.1. <http://arxiv.org/abs/astro-ph/0409262>.
55. Taflove, A.; Hagness, S. C., *Computational Electrodynamics: The Finite-Difference Time-Domain Method*. 3rd ed.; Artech House INC: 2005.
56. (a) Michaels, A. M.; Nirmal, M.; Brus, L. E., Surface enhanced Raman spectroscopy of individual rhodamine 6G molecules on large Ag nanocrystals. *Journal of the American Chemical Society* **1999**, *121* (43), 9932-9939; (b) Michaels, A. M.; Jiang, J.; Brus, L., Ag nanocrystal junctions as the site for surface-enhanced Raman scattering of single Rhodamine 6G molecules. *Journal of Physical Chemistry B* **2000**, *104* (50), 11965-11971.
57. Yang, W. H.; Schatz, G. C.; Vanduyne, R. P., Discrete Dipole Approximation for Calculating Extinction and Raman Intensities for Small Particles with Arbitrary Shapes. *Journal of Chemical Physics* **1995**, *103* (3), 869-875.
58. Liu, T.-Y.; Tsai, K.-T.; Wang, H.-H.; Chen, Y.; Chen, Y.-H.; Chao, Y.-C.; Chang, H.-H.; Lin, C.-H.; Wang, J.-K.; Wang, Y.-L., Functionalized arrays of Raman-enhancing nanoparticles for capture and culture-free analysis of bacteria in human blood. *Nature Communications* **2011**, *2*, 538-545
59. Halas, N. J.; Lal, S.; Chang, W.-S.; Link, S.; Nordlander, P., Plasmons in Strongly Coupled Metallic Nanostructures. *Chemical Reviews* **2011**, *111* (6), 3913-3961.
60. Wustholz, K. L.; Henry, A. I.; McMahon, J. M.; Freeman, R. G.; Valley, N.; Piotti, M. E.; Natan, M. J.; Schatz, G. C.; Van Duyne, R. P., Structure-Activity Relationships in Gold Nanoparticle Dimers and Trimers for Surface-Enhanced Raman Spectroscopy. *Journal of the American Chemical Society* **2010**, *132* (31), 10903-10910.
61. (a) Camden, J. P.; Dieringer, J. A.; Wang, Y. M.; Masiello, D. J.; Marks, L. D.; Schatz, G. C.; Van Duyne, R. P., Probing the structure of single-molecule surface-

- enhanced Raman scattering hot spots. *Journal of the American Chemical Society* **2008**, *130* (38), 12616; (b) Yoon, I.; Kang, T.; Choi, W.; Kim, J.; Yoo, Y.; Joo, S.-W.; Park, Q. H.; Ihee, H.; Kim, B., Single Nanowire on a Film as an Efficient SERS-Active Platform. *Journal of the American Chemical Society* **2009**, *131* (2), 758-762; (c) Hatab, N. A.; Hsueh, C.-H.; Gaddis, A. L.; Retterer, S. T.; Li, J.-H.; Eres, G.; Zhang, Z.; Gu, B., Free-Standing Optical Gold Bowtie Nanoantenna with Variable Gap Size for Enhanced Raman Spectroscopy. *Nano Letters* **2010**, *10* (12), 4952-4955; (d) McMahon, J. M.; Li, S. Z.; Ausman, L. K.; Schatz, G. C., Modeling the Effect of Small Gaps in Surface-Enhanced Raman Spectroscopy. *Journal of Physical Chemistry C* **2012**, *116* (2), 1627-1637.
62. Downes, A.; Salter, D.; Elfick, A., Finite element simulations of tip-enhanced Raman and fluorescence spectroscopy. *Journal of Physical Chemistry B* **2006**, *110* (13), 6692-6698.
63. Lu, Y.; Liu, G. L.; Kim, J.; Mejia, Y. X.; Lee, L. P., Nanophotonic crescent moon structures with sharp edge for ultrasensitive biomolecular detection by local electromagnetic field enhancement effect. *Nano Letters* **2005**, *5* (1), 119-124.
64. Sondergaard, T.; Bozhevolnyi, S. I.; Beermann, J.; Novikov, S. M.; Devaux, E.; Ebbesen, T. W., Resonant Plasmon Nanofocusing by Closed Tapered Gaps. *Nano Letters* **2010**, *10* (1), 291-295.
65. Durr, N. J.; Larson, T.; Smith, D. K.; Korgel, B. A.; Sokolov, K.; Ben-Yakar, A., Two-photon luminescence imaging of cancer cells using molecularly targeted gold nanorods. *Nano Letters* **2007**, *7* (4), 941-945.
66. Kerker, M.; Wang, D. S.; Chew, H., Surface enhanced Raman-scattering (SERS) by molecules absorbed at spherical-particles. *Applied Optics* **1980**, *19* (24), 4159-4174.
67. Stiles, P. L.; Dieringer, J. A.; Shah, N. C.; Van Duyne, R. R., Surface-Enhanced Raman Spectroscopy. *Annual Review of Analytical Chemistry* **2008**, *1*, 601-626.

68. Le Ru, E. C.; Blackie, E.; Meyer, M.; Etchegoin, P. G., Surface enhanced Raman scattering enhancement factors: a comprehensive study. *Journal of Physical Chemistry C* **2007**, *111* (37), 13794-13803.
69. Moskovits, M., Surface selection rules. *Journal of Chemical Physics* **1982**, *77* (9), 4408-4416.
70. (a) Uetsuki, K.; Verma, P.; Yano, T.-a.; Saito, Y.; Ichimura, T.; Kawata, S., Experimental Identification of Chemical Effects in Surface Enhanced Raman Scattering of 4-Aminothiophenol. *Journal of Physical Chemistry C* **2010**, *114* (16), 7515-7520; (b) Osawa, M.; Matsuda, N.; Yoshii, K.; Uchida, I., Charge-Transfer Resonance Raman Process in Surface-Enhanced Raman-Scattering from P-Aminothiophenol Adsorbed on Silver - Herzberg-Teller Contribution. *Journal of Physical Chemistry* **1994**, *98* (48), 12702-12707.
71. Fromm, D. P.; Sundaramurthy, A.; Kinkhabwala, A.; Schuck, P. J.; Kino, G. S.; Moerner, W. E., Exploring the chemical enhancement for surface-enhanced Raman scattering with Au bowtie nanoantennas. *Journal of Chemical Physics* **2006**, *124* (6).
72. McFarland, A. D.; Young, M. A.; Dieringer, J. A.; Van Duyne, R. P., Wavelength-scanned surface-enhanced Raman excitation spectroscopy. *Journal of Physical Chemistry B* **2005**, *109* (22), 11279-11285.
73. (a) Wei, H.; Hao, F.; Huang, Y.; Wang, W.; Nordlander, P.; Xu, H., Polarization dependence of surface-enhanced Raman scattering in gold nanoparticle-nanowire systems. *Nano Letters* **2008**, *8* (8), 2497-2502; (b) Tao, A. R.; Yang, P. D., Polarized surface-enhanced Raman spectroscopy on coupled metallic nanowires. *Journal of Physical Chemistry B* **2005**, *109* (33), 15687-15690; (c) Nagasawa, F.; Takase, M.; Nabika, H.; Murakoshi, K., Polarization characteristics of surface-enhanced Raman scattering from a small number of molecules at the gap of a metal nano-dimer. *Chemical Communications* **2011**, *47* (15), 4514-4516.
74. (a) Fromm, D. P.; Sundaramurthy, A.; Schuck, P. J.; Kino, G.; Moerner, W. E., Gap-dependent optical coupling of single "Bowtie" nanoantennas resonant in the

- visible. *Nano Letters* **2004**, *4* (5), 957-961; (b) Bouhelier, A.; Bachelot, R.; Lerondel, G.; Kostcheev, S.; Royer, P.; Wiederrecht, G. P., Surface plasmon characteristics of tunable photoluminescence in single gold nanorods. *Physical Review Letters* **2005**, *95* (26), 267405; (c) Imura, K.; Nagahara, T.; Okamoto, H., Near-field two-photon-induced photoluminescence from single gold nanorods and imaging of plasmon modes. *Journal of Physical Chemistry B* **2005**, *109* (27), 13214-13220; (d) Beermann, J.; Novikov, S. M.; Sondergaard, T.; Boltasseva, A. E.; Bozhevolnyi, S. I., Two-photon mapping of localized field enhancements in thin nanostrip antennas. *Optics Express* **2008**, *16* (22), 17302-17309; (e) Kim, H. M.; Xiang, C. X.; Guell, A. G.; Penner, R. M.; Potma, E. O., Tunable two-photon excited luminescence in single gold nanowires fabricated by lithographically patterned nanowire electrodeposition. *Journal of Physical Chemistry C* **2008**, *112* (33), 12721-12727.
75. Chen, C. K.; Heinz, T. F.; Ricard, D.; Shen, Y. R., Surface-Enhanced 2nd-Harmonic Generation and Raman-Scattering. *Physical Review B* **1983**, *27* (4), 1965-1979.
76. Bouhelier, A.; Beversluis, M. R.; Novotny, L., Characterization of nanoplasmonic structures by locally excited photoluminescence. *Applied Physics Letters* **2003**, *83* (24), 5041-5043.
77. Schuck, P. J.; Fromm, D. P.; Sundaramurthy, A.; Kino, G. S.; Moerner, W. E., Improving the mismatch between light and nanoscale objects with gold bowtie nanoantennas. *Physical Review Letters* **2005**, *94*, 017402.
78. Sundaramurthy, A.; Schuck, P. J.; Conley, N. R.; Fromm, D. P.; Kino, G. S.; Moerner, W. E., Toward nanometer-scale optical photolithography: Utilizing the near-field of bowtie optical nanoantennas. *Nano Letters* **2006**, *6* (3), 355-360.
79. Ghenuche, P.; Cherukulappurath, S.; Taminiau, T. H.; van Hulst, N. F.; Quidant, R., Spectroscopic mode mapping of resonant plasmon nanoantennas. *Physical Review Letters* **2008**, *101* (11), 116805.

80. Kim, H.; Taggart, D. K.; Xiang, C.; Penner, R. M.; Potma, E. O., Spatial control of coherent anti-stokes emission with height-modulated gold zig-zag nanowires. *Nano Letters* **2008**, *8* (8), 2373-2377.
81. Wang, H. F.; Huff, T. B.; Zweifel, D. A.; He, W.; Low, P. S.; Wei, A.; Cheng, J. X., In vitro and in vivo two-photon luminescence imaging of single gold nanorods. *Proceedings of the National Academy of Sciences of the United States of America* **2005**, *102* (44), 15752-15756.
82. (a) Imura, K.; Okamoto, H.; Hossain, M. K.; Kitajima, M., Visualization of localized intense optical fields in single gold-nanoparticle assemblies and ultrasensitive Raman active sites. *Nano Letters* **2006**, *6* (10), 2173-2176; (b) Imura, K.; Okamoto, H.; Hossain, M. K.; Kitajima, M., Near-field imaging of surface-enhanced Raman active sites in aggregated gold nanoparticles. *Chemistry Letters* **2006**, *35* (1), 78-79.
83. Walter, M. J.; Borys, N. J.; Gaefke, G.; Hoeger, S.; Lupton, J. M., Spatial Anticorrelation between Nonlinear White-Light Generation and Single Molecule Surface-Enhanced Raman Scattering. *Journal of the American Chemical Society* **2008**, *130* (50), 16830.
84. Borys, N. J.; Lupton, J. M., Surface-Enhanced Light Emission from Single Hot Spots in Tollens Reaction Silver Nanoparticle Films: Linear versus Nonlinear Optical Excitation. *Journal of Physical Chemistry C* **2011**, *115* (28), 13645-13659.
85. (a) Martin, C. R., Nanomaterials-a membrane-based synthetic approach. *Science* **1994**, *266* (5193), 1961-1966; (b) Masuda, H.; Fukuda, K., Ordered metal nanohole arrays made by a 2-step replication of honeycomb structures of anodic alumina. *Science* **1995**, *268* (5216), 1466-1468; (c) Martin, C. R., Membrane-based synthesis of nanomaterials. *Chemistry of Materials* **1996**, *8* (8), 1739-1746; (d) Martin, B. R.; Dermody, D. J.; Reiss, B. D.; Fang, M. M.; Lyon, L. A.; Natan, M. J.; Mallouk, T. E., Orthogonal self-assembly on colloidal gold-platinum nanorods. *Advanced Materials* **1999**, *11* (12), 1021-1025; (e) Yu, J. S.; Kim, J. Y.;

- Lee, S.; Mbindyo, J. K. N.; Martin, B. R.; Mallouk, T. E., Template synthesis of polymer-insulated colloidal gold nanowires with reactive ends. *Chemical Communications* **2000**, (24), 2445-2446; (f) Hurst, S. J.; Payne, E. K.; Qin, L. D.; Mirkin, C. A., Multisegmented one-dimensional nanorods prepared by hard-template synthetic methods. *Angewandte Chemie-International Edition* **2006**, *45* (17), 2672-2692.
86. Lu, Y.; Yin, Y. D.; Li, Z. Y.; Xia, Y. N., Synthesis and self-assembly of Au@SiO₂ core-shell colloids. *Nano Letters* **2002**, *2* (7), 785-788.
87. (a) Henzie, J.; Kwak, E. S.; Odom, T. W., Mesoscale metallic pyramids with nanoscale tips. *Nano Letters* **2005**, *5* (7), 1199-1202; (b) Henzie, J.; Shuford, K. L.; Kwak, E. S.; Schatz, G. C.; Odom, T. W., Manipulating the optical properties of pyramidal nanoparticle arrays. *Journal of Physical Chemistry B* **2006**, *110* (29), 14028-14031; (c) Hasan, W.; Lee, J. H.; Henzie, J.; Odom, T. W., Selective functionalization and spectral identification of gold nanopyramids. *Journal of Physical Chemistry C* **2007**, *111* (46), 17176-17179; (d) Lee, J.; Hasan, W.; Stender, C. L.; Odom, T. W., Pyramids: A Platform for Designing Multifunctional Plasmonic Particles. *Accounts of Chemical Research* **2008**, *41* (12), 1762-1771; (e) Shuford, K. L.; Lee, J.; Odom, T. W.; Schatz, G. C., Optical properties of gold pyramidal shells. *Journal of Physical Chemistry C* **2008**, *112* (17), 6662-6666; (f) Lin, J. Y.; Hasan, W.; Yang, J. C.; Odom, T. W., Optical Properties of Nested Pyramidal Nanoshells. *Journal of Physical Chemistry C* **2010**, *114* (16), 7432-7435; (g) Stoerzinger, K. A.; Hasan, W.; Lin, J. Y.; Robles, A.; Odom, T. W., Screening Nanopyramid Assemblies to Optimize Surface Enhanced Raman Scattering. *Journal of Physical Chemistry Letters* **2010**, *1* (7), 1046-1050; (h) Sweeney, C. M.; Stender, C. L.; Nehl, C. L.; Hasan, W.; Shuford, K. L.; Odom, T. W., Optical Properties of Tipless Gold Nanopyramids. *Small* **2011**, *7* (14), 2032-2036.
88. (a) Sun, C. H.; Linn, N. C.; Jiang, P., Templated fabrication of periodic metallic nanopyramid arrays. *Chemistry of Materials* **2007**, *19* (18), 4551-4556; (b) Lin,

- T.-H.; Linn, N. C.; Tarajano, L.; Jiang, B.; Jiang, P., Electrochemical SERS at Periodic Metallic Nanopyramid Arrays. *Journal of Physical Chemistry C* **2009**, *113* (4), 1367-1372; (c) Linn, N. C.; Sun, C.-H.; Arya, A.; Jiang, P.; Jiang, B., Surface-enhanced Raman scattering on periodic metal nanotips with tunable sharpness. *Nanotechnology* **2009**, *20* (22), 225303; (d) Liu, X. F.; Sun, C. H.; Linn, N. C.; Jiang, B.; Jiang, P., Wafer-Scale Surface-Enhanced Raman Scattering Substrates with Highly Reproducible Enhancement. *Journal of Physical Chemistry C* **2009**, *113* (33), 14804-14811; (e) Chung, P.-Y.; Lin, T.-H.; Schultz, G.; Batich, C.; Jiang, P., Nanopyramid surface plasmon resonance sensors. *Applied Physics Letters* **2010**, *96* (26), 261108.
89. (a) Nagpal, P.; Lindquist, N. C.; Oh, S. H.; Norris, D. J., Ultrasoother Patterned Metals for Plasmonics and Metamaterials. *Science* **2009**, *325* (5940), 594-597; (b) Lindquist, N. C.; Nagpal, P.; Lesuffleur, A.; Norris, D. J.; Oh, S. H., Three-Dimensional Plasmonic Nanofocusing. *Nano Letters* **2010**, *10* (4), 1369-1373.
90. (a) Hossain, M. K.; Shimada, T.; Kitajima, M.; Imura, K.; Okamoto, H., Near-field Raman imaging and electromagnetic field confinement in the self-assembled monolayer array of gold nanoparticles. *Langmuir* **2008**, *24* (17), 9241-9244; (b) Farcau, C.; Astilean, S., Mapping the SERS Efficiency and Hot-Spots Localization on Gold Film over Nanospheres Substrates. *Journal of Physical Chemistry C* **2010**, *114* (27), 11717-11722; (c) Fang, Y.; Seong, N.-H.; Dlott, D. D., Measurement of the distribution of site enhancements in surface-enhanced Raman scattering. *Science* **2008**, *321* (5887), 388-392.
91. (a) Beermann, J.; Novikov, S. M.; Sondergaard, T.; Rafaelsen, J.; Pedersen, K.; Bozhevolnyi, S. I., Localized field enhancements in two-dimensional V-groove metal arrays. *Journal of the Optical Society of America B-Optical Physics* **2011**, *28* (3), 372-378; (b) Perney, N. M. B.; Baumberg, J. J.; Zoorob, M. E.; Charlton, M. D. B.; Mahnkopf, S.; Netti, C. M., Tuning localized plasmons in nanostructured substrates for surface-enhanced Raman scattering. *Optics Express* **2006**, *14* (2), 847-857.

92. Lee, S. H.; Bantz, K. C.; Lindquist, N. C.; Oh, S.-H.; Haynes, C. L., Self-Assembled Plasmonic Nanohole Arrays. *Langmuir* **2009**, *25* (23), 13685-13693.
93. Sung, J.; Kosuda, K. M.; Zhao, J.; Elam, J. W.; Spears, K. G.; Van Duyne, R. P., Stability of silver nanoparticles fabricated by nanosphere lithography and atomic layer deposition to femtosecond laser excitation. *Journal of Physical Chemistry C* **2008**, *112* (15), 5707-5714.
94. Beversluis, M. R.; Bouhelier, A.; Novotny, L., Continuum generation from single gold nanostructures through near-field mediated intraband transitions. *Physical Review B* **2003**, *68* (11), 115433.
95. Joo, T. H.; Kim, M. S.; Kim, K., Surface-Enhanced Raman-Scattering of Benzenethiol in Silver Sol. *Journal of Raman Spectroscopy* **1987**, *18* (1), 57-60.

Vita

He-Chun Chou received his BS and MS of chemistry from National Taiwan University in 2001 and 2004 respectively, and he began his PhD work in 2007.

Permanent address (or email): hcchou@utexas.edu

This dissertation was typed by He-Chun Chou